UNIVERSIDADE FEDERAL DO RIO GRANDE DO SUL

CENTRO ESTADUAL DE PESQUISAS EM SENSORIAMENTO REMOTO E METEOROLOGIA

PROGRAMA DE PÓS-GRADUAÇÃO EM SENSORIAMENTO REMOTO

SAVANNAH TÂMARA LEMOS DA COSTA

AVALIAÇÃO DE MÉTODOS *SINGLE CHANNEL* NA ESTIMATIVA DA TEMPERATURA DA SUPERFÍCIE TERRESTRE NO HEMISFÉRIO SUL A PARTIR DE DADOS ORBITAIS NO INFRAVERMELHO TERMAL

PORTO ALEGRE

2022

SAVANNAH TÂMARA LEMOS DA COSTA

AVALIAÇÃO DE MÉTODOS *SINGLE CHANNEL* NA ESTIMATIVA DA TEMPERATURA DA SUPERFÍCIE TERRESTRE NO HEMISFÉRIO SUL A PARTIR DE DADOS ORBITAIS NO INFRAVERMELHO TERMAL

Dissertação de mestrado apresentada ao Programa de Pós-Graduação em Sensoriamento Remoto como requisito parcial para a obtenção do título de mestre em Sensoriamento Remoto e Geoprocessamento.

Orientadora: Profa. Dra. Silvia Beatriz Alves Rolim

PORTO ALEGRE

2022

CIP - Catalogação na Publicação

LEMOS DA COSTA, SAVANNAH TÂMARA
AVALIAÇÃO DE MÉTODOS SINGLE CHANNEL NA ESTIMATIVA DA TEMPERATURA DA SUPERFÍCIE TERRESTRE NO HEMISFÉRIO SUL A PARTIR DE DADOS ORBITAIS NO INFRAVERMELHO TERMAL / SAVANNAH TÂMARA LEMOS DA COSTA. -- 2022.
108 f.
Orientadora: SILVIA BEATRIZ ALVES ROLIM.

Dissertação (Mestrado) -- Universidade Federal do Rio Grande do Sul, Centro Estadual de Pesquisas em Sensoriamento Remoto e Meteorologia, Programa de Pós-Graduação em Sensoriamento Remoto, Porto Alegre, BR-RS, 2022.

1. Temperatura da Superfície Terrestre. 2. Sensoriamento Remoto. 3. Infravermelho termal. 4. Transferência Radiativa. 5. Correção atmosférica. I. ALVES ROLIM, SILVIA BEATRIZ, orient. II. Título.

Elaborada pelo Sistema de Geração Automática de Ficha Catalográfica da UFRGS com os dados fornecidos pelo(a) autor(a).

DISSERTAÇÃO

Submetida como parte dos requisitos
para obtenção do Grau de

MESTRE EM SENSORIAMENTO REMOTO E GEOPROCESSAMENTO

Programa de Pós-Graduação em Sensoriamento Remoto (PPGSR)
Centro Estadual de Pesquisas em Sensoriamento Remoto e Meteorologia (CEPRSM)
Universidade Federal do Rio Grande do Sul (UFRGS)
Porto Alegre, RS, Brasil.

Aprovada em: 03/10/2022.

Homologada em: ____/____/_____.

Pela Banca Examinadora:

Por:

SRolim
Digitally signed by SRolim
DN: cn=SRolim, o=UFRGS, ou,
email=silvia.rolim@ufrgs.br, c=BR
Date: 2022.10.10 09:29:12 -03'00'

Profa. Dra. Silvia Beatriz Alves Rolim
Orientadora

Prof. Dr. Guilherme Garcia de Oliveira
Coordenador do Programa de Pós-Graduação em Sensoriamento Remoto

Dr. Jorge Ricardo Ducati
(PPGSR/UFRGS)

Nájila Rocha

Dra. Nájila Souza da Rocha
(Egressa PPGSR/UFRGS)

Dr. Bijeesh Kozhikkodan Veettil
(Thu Dau Mot University)

Dedico este trabalho à minha avó, Eugênia Fernandes Lemos, pelos seus ensinamentos e valores disseminados.

AGRADECIMENTOS

Aos meus familiares, em especial ao meu pai Sinval e minha mãe Mônica, pelo apoio e por nunca terem medido esforços para me proporcionar um ensino de qualidade.

À minha irmã Pâmela e ao João, pelo apoio e companheirismo.

À minha orientadora professora Dra. Silvia Rolim, pelas contribuições, críticas e sugestões inestimáveis para a construção dessa pesquisa e pelo apoio, confiança e amizade durante esta jornada.

Aos meus colegas de curso, Lucas, Gabriel, Pâmela, Eduardo e Nájila, que participaram, em vários momentos, da construção desse estudo.

As minhas amigas, Ádila, Giovanna e Letícia, pelo apoio.

À Universidade Federal do Rio Grande do Sul, ao Centro Estadual de Pesquisas em Sensoriamento Remoto e Meteorologia e ao Laboratório de Sensoriamento Remoto Geológico por fornecerem estrutura e recursos para o desenvolvimento desta pesquisa.

À Coordenação de Aperfeiçoamento de Pessoal de Nível Superior (CAPES) pela concessão da bolsa de pesquisa.

RESUMO

Diversos métodos tem sido propostos para estimar a Temperatura da Superfície Terrestre (LST) a partir de dados do infravermelho termal obtidos por satélites. Esses esforços são uma tentativa de minimizar os erros impostos na solução não-linear da transferência radiativa no sistema superfície-atmosfera. Além disso, a correção atmosférica em dados termais é um dos fatores fundamentais para obter LST acurada. Os métodos *Single Channel* (SC) permitem derivar a LST a partir da radiância medida em uma banda. Assim, consistem em uma oportunidade para estimar LST de longo prazo com os dados termais da série Landsat, com quase 40 anos de registro. Contudo, a maioria dos SC é desenvolvida e projetada para as condições atmosféricas e de superfície do Hemisfério Norte. Nesse contexto, essa dissertação objetivou avaliar o desempenho dos algoritmos *Generalized Single Channel* (GSC), *Improved Single Channel* (ISC) e *Surface Temperature product* (produto ST) na estimativa da LST em uma região litorânea do Hemisfério Sul. Para tanto, um campo de dunas composto por 99,53% de quartzo foi selecionado e dados do Landsat 8 TIRS foram utilizados. Inicialmente, para fundamentar a avaliação, investigou-se a aplicabilidade de perfis verticais de diferentes resoluções espaciais e horizontais, derivados de produtos de reanálise NCEP, na correção atmosférica, bem como, os impactos gerados na estimativa da LST. Os resultados mostraram que os perfis NCEP CFSv2 de resoluções originais e os perfis NCEP FNL utilizados pela Calculadora de Parâmetros de Correção Atmosférica (ACPC) da NASA foram os mais adequados para a correção atmosférica. Considerando as vantagens da ACPC, ela também foi utilizada para estimar os dados atmosféricos empregados nos algoritmos GSC e ISC na avaliação. O algoritmo ISC (RMSE de 0,69 K) apresentou o melhor desempenho na estimativa da LST, seguido do GSC (RMSE de 2,5 K) e do produto ST (RMSE de 4,24 K). De modo geral, concluiu-se que o ISC se mostrou o mais adequado para calcular a LST, podendo ser aplicado em estudos de balanço de energia, onde um erro de até 2 K é aceitável. Confirmou-se, portanto, a importância da análise dos métodos SC no presente trabalho, justificada pela sua aplicação em dados de radiância de sensores termais com uma banda, principalmente para estudos com séries temporais de LST da série Landsat, além de situações de mau funcionamento de canais espectrais.

Palavras-chave: Transferência radiativa. Correção atmosférica. Single Channel.

ABSTRACT

Several methods have been proposed to estimate the Land Surface Temperature (LST) from thermal infrared data obtained by satellites. These efforts are an attempt to minimize errors imposed in the nonlinear solution of radiative transfer in the surface-atmosphere system. Furthermore, atmospheric correction in thermal data is one of the key factors to obtain accurate LST. Single Channel (SC) methods allow to retrieve the LST from the measured radiance in one band. Thus, they provide an opportunity to estimate long-term LST with the Landsat thermal data series, with almost 40 years of record. However, most SCs are developed and designed for the atmospheric and surface conditions of the Northern Hemisphere. In this context, this dissertation aimed to evaluate the performance of the Generalized Single Channel (GSC), Improved Single Channel (ISC) and Surface Temperature product (ST product) algorithms in estimating LST in a coastal region of the Southern Hemisphere. For that, a dune field composed of 99.53% quartz was selected and Landsat 8 TIRS data were used. Initially, to support the evaluation, the applicability of vertical profiles of different spatial and horizontal resolutions, derived from NCEP reanalysis products, in atmospheric correction, as well as the impacts generated in the LST estimation, was investigated. The results showed that the original resolution NCEP CFSv2 profiles and the NCEP FNL profiles used by NASA's Atmospheric Correction Parameters Calculator (ACPC) were the most suitable for atmospheric correction. Considering the advantages of ACPC, it was also used to estimate the atmospheric data used in the GSC and ISC algorithms in the evaluation. The ISC algorithm (RMSE of 0.69 K) presented the best performance in retrieving the LST, followed by the GSC (RMSE of 2.5 K) and the ST product (RMSE of 4.24 K). In general, it was concluded that the ISC proved to be the most suitable to calculate the LST, and can be applied in energy balance studies, where an error of up to 2 K is acceptable. Therefore, the importance of the analysis of SC methods in the present work was confirmed, justified by their application in radiance data from thermal sensors with one band, mainly for studies with time series of LST from Landsat series, in addition to situations of channel malfunction.

Keywords: Radiative transfer. Atmospheric correction. Single Channel.

LISTA DE ABREVIATURAS E SIGLAS

ACPC	Calculadora de Parâmetros de Correção Atmosférica, do inglês *Atmospheric Correction Parameter Calculation*
ASTER	*Advanced Spaceborne Thermal Emission and Reflection Radiometer*
BOA	Base da Atmosfera, do inglês *Bottom of Atmosphere*
CFSv2	*Climate Forecast System Version 2*
ECMWF	*European Centre for Medium-Range Weather Forecasts*
FNL	*Final Operational Model Global Tropospheric Analyses*
FP-IT	*Forward Processing – Instrument Team*
FTIR	*Fourier-transform Infrared*
GED	*Global Emissivity Dataset*
GEOS	*Goddard Earth Observing System Model*
GEOS-5	*Goddard Earth Observing System Model*, versão 5
GSC	Canal Único Generalizado, do inglês *Generalized Single Channel*
ISC	Canal Único Melhorado, do inglês *Improved Single Channel*
L2SP	*Landsat Level 2 Science Products*
LST	Temperatura da Superfície Terrestre, do inglês *Land Surface Temperature*
LUT	Tabela de Referência, do inglês *Look-Up Table*
MDE	Modelo Digital de Elevação
MERRA-2	*Modern-Era Retrospective Analysis for Research and Applications* versão 2
MODTRAN	*Moderate Resolution Atmospheric Transmission*
MTR	Modelo de Transferência Radiativa
MW	Monocanal, do inglês *Mono Window*
NASA	Administração Nacional da Aeronáutica e Espaço, do inglês *National Aeronautics and Space Administration*
NCEP	*National Centers for Environmental Predictions*
NDVI	Índice de Vegetação por Diferença Normalizada, do inglês *Normalized Difference Vegetation Index*
$NDVI^{THM}$	Limiar do Índice de Vegetação por Diferença Normalizada, do inglês *Normalized Difference Vegetation Index threshold*
NIR	Infravermelho próximo, do inglês *Near InfraRed*

OLI	*Operational Land Imager*
REM	Radiação Eletromagnética
RTE	Equação da Transferência Radiativa, do inglês *Radiative Transfer Equation*
SC	Canal Único, do inglês *Single Channel*
ST	Temperatura da Superfície, do inglês *Surface Temperature*
SW	*Split Window*
TIR	Infravermelho Termal, do inglês *Thermal Infrared*
TIRS	*Thermal Infrared Sensor*
TOA	Topo da Atmosfera, do inglês *Top of Atmosphere*
USGS	Serviço Geológico dos Estados Unidos, do inglês *United States Geological Survey*
WRF	*Weather Research and Forecasting*

SUMÁRIO

APRESENTAÇÃO

Um dos maiores impasses de avaliar informações de sensoriamento remoto orbital é a necessidade de validação das informações a partir de campanhas de campo. Nessa pesquisa, essa tarefa se tornou ainda mais complexa uma vez que foi desenvolvida durante a pandemia do COVID-19. Dessa forma, os resultados dessa dissertação refletem os esforços que foram realizados durante a pandemia pelo grupo de pesquisadores do Laboratório de Sensoriamento Remoto Geológico (LabSRGeo) do Programa de Pós Graduação em Sensoriamento Remoto (PPGSR) da UFRGS e que possibilitaram a conclusão dessa pesquisa com êxito.

As restrições impostas pelo contexto epidemiológico reduziram as campanhas de medidas de variáveis físicas no campo, em parte superadas pela homogeneidade do alvo, um campo de dunas com 99,53% de SiO_2 com propriedades espectrais bem conhecidas. O ineditismo desta pesquisa no sul do Brasil foi fundamental como ponto de partida para avaliar o desempenho dos métodos *single channel* na recuperação de temperatura e emissividade a partir de dados termais mono canais da série de 40 anos (1984 a 2022), do Landsat 5 a 7 e do Landsat 8. Este último, apesar de 2 canais, apresentou problemas de desempenho. Por fim, a importância do presente projeto, se alicerça na necessidade de gerar conhecimento, integrá-lo nas diversas pontas da pesquisa e, em síntese, no aprimoramento do saber científico sobre o balanço de energia no hemisfério sul.

No contexto das mudanças climáticas, a estimativa da Temperatura da Superfície Terrestre (*Land Surface Temperature - LST*) utilizando dados de sensoriamento remoto orbital tem sido um dos tópicos fundamentais. Ela tem dado suporte às pesquisas científicas, principalmente, se tratando do monitoramento histórico do balanço de energia terrestre.

Nessa dissertação de mestrado, métodos de estimativa da LST usando dados do Landsat 8 foram avaliados e, para alcançar esse objetivo, dois artigos foram produzidos. O primeiro artigo foi publicado na revista *Atmosphere* e permitiu descobrir qual a fonte de dados atmosféricos mais adequada para realizar a correção dos efeitos atmosféricos, tarefa inerente à recuperação da LST a partir de dados orbitais no infravermelho termal. O segundo artigo foi submetido na revista *Journal of Applied*

Remote Sensing, consistiu no objetivo principal da pesquisa. Esse artigo respondeu qual o método *Single Channel* possui o melhor desempenho na recuperação da LST.

No Hemisfério Sul, em especial no Brasil, ainda existe um *gap* de informações acerca do erro na LST produzido pelos métodos, bem como, suas aplicações em diferentes sensores orbitais. Portanto, essa pesquisa integrou um dos passos iniciais para conhecer o desempenho desses métodos na estimativa da LST em um campo de dunas no litoral norte do Rio Grande do Sul - Brasil.

1 INTRODUÇÃO

A Temperatura da Superfície Terrestre (*Land Surface Temperature - LST*) é uma variável física definida pela radiância emitida pela superfície da Terra e tem sido um dos parâmetros chave na compreensão espaço-temporal do balanço de energia na interface superfície-atmosfera (DASH *et al.*, 2001; LI *et al.*, 2013b; SEKERTEKIN, 2019; SEKERTEKIN; BONAFONI, 2020; TANG; LI, 2014).

Diante das mudanças no sistema climático evidenciadas no Painel Intergovernamental sobre Mudanças Climáticas (IPCC) (PÖRTNER *et al.*, 2022), a LST tem desempenhado um papel importante na climatologia urbana (KHOSHNOODMOTLAGH *et al.*, 2021), monitoramento de queimadas (GUANGMENG; MEI, 2004; PRASAD; BANDI; PADMAJA, 2013), geologia (LIU *et al.*, 2021) e monitoramento dos recursos ambientais (SHI; SUN; XIAO, 2021; XU *et al.*, 2020). Algumas aplicações envolvem, por exemplo, a utilização da LST, em alguns casos combinada com outros produtos de satélite, como parâmetro de entrada em modelos de estimativa da evapotranspiração (KÄFER *et al.*, 2022; SOBRINO *et al.*, 2021), na detecção de estresse hídrico e de ilhas de calor urbanas (KAISER *et al.*, 2022) e em modelos numéricos de previsão do tempo (ROSAS; HOUBORG; MCCABE, 2017; SOBRINO *et al.*, 2016; YANG *et al.*, 2020).

O monitoramento das variações de LST em escala local, regional e global é possível através do sensoriamento remoto orbital. Os dados do Infravermelho Termal (*Thermal Infrared – TIR),* registrados por sensores de satélites, são amplamente utilizados para estimar a LST (CRISTÓBAL *et al.*, 2018; JIMENEZ-MUNOZ *et al.*, 2014; JIMÉNEZ-MUNOZ; SOBRINO, 2003; LI *et al.*, 2013b; TANG; LI, 2014; TARDY *et al.*, 2016). Nesse contexto, a série Landsat possui 40 anos de registro de dados TIR, em pelo menos uma banda, com resolução espacial de 60 a 120 metros, consistindo, portanto, em uma oportunidade de estudar tendências de LST de longo prazo (1982 – presente) com resolução espacial moderada (KAISER *et al.*, 2022; MALAKAR *et al.*, 2018).

Estimar a LST precisamente a partir de dados TIR é um grande desafio, pois a radiância registrada pelo sensor depende de parâmetros da superfície (temperatura e emissividade) e da correção dos efeitos atmosféricos (DASH *et al.,* 2001; LI *et al.,* 2013b; ROLIM *et al.,* 2016, 2020). A Equação da Transferência Radiativa (*Radiative*

Transfer Equation – RTE) é amplamente utilizada para corrigir os efeitos atmosféricos e, assim, converter a radiância infravermelha registrada pelo sensor em LST. Contudo, ela é indeterminada, sendo o número de variáveis para solucionar (uma temperatura e *n* emissividades) sempre maior que o número de observações disponíveis (*n*). Para solucionar esse problema, suposições e restrições na RTE foram necessárias, dando origem a vários métodos de estimativa da LST (DASH *et al.*, 2001; LI *et al.*, 2013b; MALAKAR *et al.*, 2018; ROLIM *et al.*, 2016).

Existem diversas propostas de classificação dos métodos de estimativa da LST (LI *et al.*, 2013a, 2013b; ROLIM *et al.*, 2016). Uma delas está relacionada ao número de bandas espectrais utilizadas, como a abordagem de canal único (*Single Channel – SC)* ou multicanal. A inversão e solução da RTE, os algoritmos *Generalized Single Channel (GSC)* (JIMENEZ-MUNOZ *et al.*, 2014; JIMÉNEZ-MUNOZ; SOBRINO, 2003; JIMÉNEZ-MUÑOZ; SOBRINO, 2010; SOBRINO; JIMÉNEZ-MUÑOZ; PAOLINI, 2004), *Improved Single Channel (ISC)* (Cristóbal et al. 2009, 2018) e *Mono Window (MW)* (QIN; KARNIELI; BERLINER, 2001) são exemplos de métodos SC. Já o *Split Window (SW)* (BECKER; LI, 2007; MCMILLIN, 1975; SOBRINO *et al.*, 1994) e *Temperature and Emissivity Separation* (LI *et al.*, 2013a; ROLIM *et al.*, 2016) são métodos que utilizam duas bandas ou mais, sendo uma evolução das abordagens de canal único.

A importância de se avaliar métodos SC no presente trabalho se justifica pela sua aplicação em dados de radiância de sensores termais com uma banda, a exemplo de parte da série Landsat, plataformas 4, 5 e 7 (1982 a 2022), além de situações de mau funcionamento de canais espectrais, como o ocorrido no Landsat 8.

Os métodos SC supõem que a emissividade é conhecida previamente. Dentre eles, inverter e solucionar a RTE é a maneira mais confiável para estimar a LST pois não envolve aproximações adicionais (CRISTÓBAL *et al.*, 2018; JIMENEZ-MUNOZ *et al.*, 2014; SEKERTEKIN, 2019; SEKERTEKIN; BONAFONI, 2020; YANG *et al.*, 2020; YU; GUO; WU, 2014). A RTE requer parâmetros de correção atmosférica (transmitância e radiâncias atmosféricas no sentido ascendente e descendente) de alta qualidade. Esses parâmetros são obtidos a partir de perfis verticais de radiossondagens síncronas à passagem do satélite.

Todavia, radiossondagens *in situ* geralmente não estão disponíveis e campanhas de lançamento possuem um alto custo financeiro envolvido. Como alternativa, produtos de perfis atmosféricos provindos de diferentes fontes vêm sendo utilizados, como por exemplo, dados globais de reanálise (DIAZ *et al.*, 2020; ROSAS; HOUBORG; MCCABE, 2017; YANG *et al.*, 2020).

Dados de reanálise proporcionam uma resolução temporal flexível (de 3 ou 6 horas, tipicamente) e consistem em uma alternativa prática às restrições espaciais dos dados de radiossondas (ROSAS; HOUBORG; MCCABE, 2017). A partir dessa abordagem, foi desenvolvida uma Calculadora de Parâmetros de Correção Atmosférica (*Atmospheric Correction Parameter Calculator – ACPC*) que estima, automaticamente, para qualquer data e local, os parâmetros de correção atmosférica usando perfis de reanálise do *National Centers for Environmental Predictions* (NCEP) e o *MODerate resolution atmospheric TRANsmission* (MODTRAN) (BARSI *et al.*, 2005; BARSI; BARKER; SCHOTT, 2003; NASA, 2021).

Além disso, a utilização da RTE combinada com parâmetros atmosféricos derivados de dados de reanálise permitiu a geração de produtos de LST de longo prazo derivados do Landsat 5, 7, 8 e 9, conhecidos como *Surface Temperature product* (produto ST), que faz parte da coleção *Landsat Level 2 Science Product* (L2SP) (COOK *et al.*, 2014; HULLEY; HUGHES; HOOK, 2012; ZANTER, 2018).

Dentre os métodos SC, os algoritmos GSC e ISC foram desenvolvidos para reduzir a dependência de radiossondagens bem como satisfazer as características de vários sensores. O GSC permitiu a correção dos efeitos atmosféricos apenas com o uso do conteúdo de vapor d'água, além do mais, foi projetado para ampla aplicação em diversos sensores (JIMENEZ-MUNOZ *et al.*, 2014; JIMÉNEZ-MUNOZ; SOBRINO, 2003). O ISC, por sua vez, foi elaborado para melhorar o GSC por meio da introdução da temperatura atmosférica média juntamente com o vapor d'água para corrigir os efeitos atmosféricos (CRISTÓBAL *et al.*, 2009, 2018).

As suposições e restrições impostas pelos métodos SC, como reduzir o número de incógnitas na RTE, tratar de condições específicas de superfície ou características particulares de um sensor, são tentativas de minimizar as incertezas na estimativa da LST, porém podem se mostrar adequadas para alguns ambientes e outros não (DASH *et al.*, 2001; LI; JIANG, 2018; LI; BECKER, 1993; MALAKAR *et al.*, 2018). Além disso, as incertezas na estimativa da LST podem resultar de uma correção atmosférica ineficaz.

A maioria dos métodos SC são projetados e validados para o Hemisfério Norte, que apresenta condições atmosféricas e de superfície diferentes do Hemisfério Sul (ANDREWS, 1989; VAN LOON, 1991). Portanto, existe uma necessidade em conhecer o desempenho desses métodos no Hemisfério Sul, em locais como o Brasil devido à sua diversidade climática.

Vários estudos tem mostrado que, para detecção de mudanças climáticas, as incertezas na LST podem variar de 0,3 K a 1 K. Em contrapartida, em estudos de balanço de energia um erro de até 2 K é aceitável (BENMECHETA; ABDELLAOUI; HAMOU, 2014; GUILLEVIC *et al.*, 2018; ROCHA *et al.*, 2020). Dessa forma, nota-se que conhecer a acurácia da LST estimada através dos métodos SC é fundamental, para que possa ser aplicada com confiança na compreensão dos sistemas climáticos. Além do mais, atenção deve ser dada à qualidade dos dados usados na correção dos efeitos atmosféricos, pois podem ser fonte de erros sistemáticos na estimativa da LST.

Com base no exposto, esta pesquisa objetivou avaliar o desempenho dos algoritmos de canal único GSC, ISC e do produto ST na estimativa da LST. Para embasar esta avaliação, primeiramente, a aplicabilidade de perfis verticais derivados de produtos de reanálise como fonte de dados de correção atmosférica foi investigada.

2 OBJETIVO GERAL

O objetivo desta dissertação foi avaliar o desempenho dos algoritmos *Generalized Single Channel, Improved Single Channel,* e o produto ST na estimativa da LST em uma região do Hemisfério Sul.

2.1 Objetivos específicos

- Analisar o impacto de perfis atmosféricos de diferentes resoluções horizontal, vertical e temporal na correção atmosférica e na estimativa da LST. Este objetivo específico se dividiu em duas etapas, sendo elas:
    - I Comparar os parâmetros de correção atmosférica (transmitância, radiância atmosféricas no sentido ascendente e descendente) estimados a partir de perfis verticais com diferentes resoluções horizontal, vertical e temporal, extraídos de dados de reanálise NCEP.

II Verificar o erro na LST estimada a partir da RTE empregando os diferentes perfis verticais como fonte de dados para a correção atmosférica.

- Avaliar o desempenho dos algoritmos GSC e ISC e do produto ST na estimativa da LST, a partir da utilização de perfil de reanálise NCEP, interpolado pela ACPC, como fonte de dados atmosféricos.

3 SENSORIAMENTO REMOTO NO INFRAVERMELHO TERMAL

Toda matéria com temperatura acima do zero absoluto (0 K ou -273°C), tais como a superfície do Sol, corpos d'água, vegetação, rochas e o solo, emite Radiação Eletromagnética (REM) (JENSEN, 2009; KUENZER; DECH, 2013). O Sol, com temperatura aproximada de 6000 K, emite REM desde os raios gama até as ondas de rádio, sendo que sua irradiação máxima ocorre no espectro visível (0,48 µm). Já a Terra, com temperatura média de 300 K, concentra sua emissão na região do infravermelho termal e apresenta pico de máxima emissão no comprimento de onda de 9,67 µm (JENSEN, 2009; LIOU, 2002; OLSEN, 2007; SCHOTT, 2007; TANG; LI, 2014).

O TIR abrange os comprimentos de onda de 3 a 14 µm. Nesse intervalo existem janelas atmosféricas entre 3 a 5 µm e 8 a 14 µm que tornam possível o mapeamento da superfície terrestre (KUENZER; DECH, 2013; SABINS, 1996). São nessas janelas que a atmosfera permite a transmissão de porção da REM infravermelha do terreno para os detectores orbitais (JENSEN, 2009; LIOU, 2002). Por outro lado, há regiões do espectro em que a REM infravermelha é altamente absorvida por gases como o vapor d'água (H_2O), o dióxido de carbono (CO_2) e o ozônio (O_3) (KUZNETSOV *et al.*, 2012; LIOU, 2002; OLSEN, 2007). O intervalo entre 5 a 7 µm, por exemplo, é dominado pela absorção do vapor d'água (região escura na Figura 1), o tornando inútil para o sensoriamento remoto (JENSEN, 2009; OLSEN, 2007).

Figura 1 – Espectro Eletromagnético e as principais janelas atmosféricas.

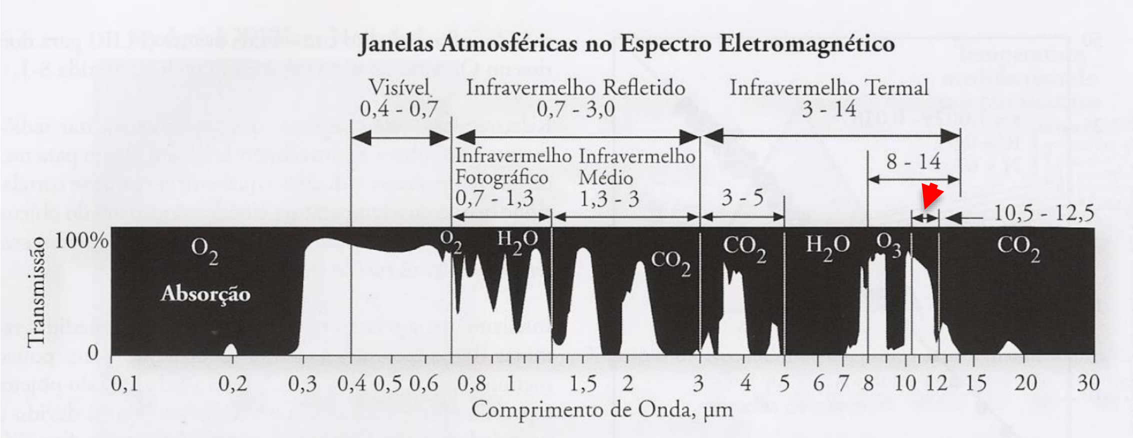

Fonte: Jensen, 2009.

Dentro da faixa de 3–5 μm, a luz solar refletida ainda pode contaminar levemente o sinal térmico (emitido). Dentro da faixa de 8-14 μm existe apenas uma estreita banda de absorção de O_3 (9,2 a 10,2 μm). Portanto, os sensores orbitais são projetados para evitar esta banda de absorção e registrar informações no intervalo entre 10,5-12,5 μm (indicado pela seta vermelha na Figura 1) (JENSEN, 2009; KUENZER; DECH, 2013).

3.1 Leis Físicas

As leis físicas que regem o TIR são fundamentais para compreender como os dados registrados pelos sensores são convertidos em temperatura. O corpo negro é um corpo hipotético que absorve toda a energia incidente e a emite em sua máxima taxa possível por unidade de área em cada comprimento de onda para uma dada temperatura (JENSEN, 2009; KUZNETSOV *et al.*, 2012). A quantidade de REM emitida por um corpo negro em equilíbrio térmico é descrita pela Lei de Planck conforme a Equação 1 (LI *et al.*, 2013b; PLANCK, 1900):

$$B_\lambda(T) = \frac{C_1}{\lambda^5\left(e^{C_2/\lambda T} - 1\right)} \qquad (1)$$

Onde $B_\lambda(T)$ é a radiação espectral (Wm^{-2}μm^{-1}sr^{-1}) do corpo negro a uma temperatura T (K) e a um comprimento de onda λ (μm). C_1 e C_2 são constantes físicas, iguais a 1,191x10^{8} Wμm^{4}m^{-2}sr^{-1} e 14387,7 μmK (KUENZER; DECH, 2013; KUZNETSOV et al., 2012).

O fluxo total de energia emitida por um corpo negro ao longo de todo o espectro eletromagnético é expresso pela lei de Stefan-Boltzmann (JENSEN, 2009; KUZNETSOV *et al.*, 2012; TANG; LI, 2014) e pode ser obtido por:

$$M(T) = \sigma T^4 \tag{2}$$

Em que M é a energia irradiada (Wm^{-2}), σ é a constante de Stefan-Boltzmann ($5{,}6697.10^{-8} Wm^{-2}K^{-4}$) e T é a temperatura (K). Observa-se que a energia total emitida pelo corpo negro é proporcional à quarta potência de sua temperatura. Portanto, à medida que a temperatura aumenta, maior é a quantidade de energia emitida (JENSEN, 2009; TANG; LI, 2014).

Além disso, o aumento da temperatura desloca o pico de máxima emissão do corpo negro para comprimento de onda menores, processo descrito pela lei de deslocamento de Wien (JENSEN, 2009; KUZNETSOV *et al.*, 2012; OLSEN, 2007; TANG; LI, 2014):

$$\lambda_{max} = \frac{A}{T} \tag{3}$$

Onde λ_{max} é o comprimento de onda em que ocorre a máxima emissão, A é a constante de deslocamento de Wien (2897,8 μmK) e T é a temperatura (K).

Teoricamente assume-se que o Sol e a Terra, com suas respectivas temperaturas, são corpos negros (JENSEN, 2009). Contudo, nenhum objeto na natureza é um emissor ideal. Dessa forma, a emissividade (ε), que é definida pela razão entre a radiância de um objeto e a de um corpo negro à mesma temperatura, deve ser considerada (LI *et al.*, 2013b; TANG; LI, 2014). Ela representa a capacidade de um material transformar energia incidente em radiação térmica. A vegetação, o solo, a água e a rocha são corpos que radiam seletivamente e possuem emissividade maior que 0 e menor que 1 (JENSEN, 2009; KUENZER; DECH, 2013). A radiância espectral desses corpos seletivos é dada pela emissividade espectral multiplicada pela equação de Planck mostrada na equação 1 (JENSEN, 2009; KUZNETSOV *et al.*, 2012; TANG; LI, 2014).

3.2 Transferência radiativa no sistema Terra-Atmosfera

Um sensor infravermelho a bordo de um satélite, imageando a superfície, registra a REM emitida pela Terra e pela atmosfera ao longo de sua linha de visada (LI *et al.*, 2013b; TANG; LI, 2014). Com base na aproximação teórica da RTE, e assumindo condições de céu claro sob equilíbrio termodinâmico local, a REM infravermelha

($R_i(\theta,\varphi)$) medida pela banda de um sensor no Topo da Atmosfera (TOA) pode ser escrita como:

$$R_i(\theta,\varphi) = \quad Rg_i(\theta,\varphi)\tau_i(\theta,\varphi) \quad + \quad R_{at_i\uparrow}(\theta,\varphi) \quad + \quad R_{sl_i\uparrow}(\theta,\varphi) \qquad (4)$$

Em que θ e φ são os ângulos de visada zenital e azimutal, respectivamente. i é a banda/canal do sensor. $Rg_i(\theta,\varphi)\tau_i(\theta,\varphi)$ corresponde a radiação emitida pela superfície e atenuada pela atmosfera, $R_{at_i\uparrow}(\theta,\varphi)$ representa a emissão atmosférica e $R_{sl_i\uparrow}(\theta,\varphi)$ é a radiação espalhada pela atmosfera (LI *et al.*, 2013b; TANG; LI, 2014).

Um sensor na Base da Atmosfera (BOA) registra apenas o termo $Rg_i(\theta,\varphi)$ que pode ser descrito por:

$$Rg_i(\theta,\varphi) = \quad \varepsilon_i(\theta,\varphi)B_i(T_s) \quad + \quad [1-\varepsilon_i(\theta,\varphi)]R_{at_i\downarrow} \quad + \quad [1-\varepsilon_i(\theta,\varphi)]R_{sl_i\downarrow}$$
$$+ \rho_{b_i}(\theta,\varphi,\theta_s,\varphi_s)E_i\, cos(\theta_s)\, \tau_i(\theta_s,\varphi_s) \qquad (5)$$

Nesta equação o termo $\varepsilon_i(\theta,\varphi)B_i(T_s)$ representa a emissão da superfície. O termo $[1-\varepsilon_i(\theta,\varphi)]R_{at_i\downarrow}$ refere-se à emissão atmosférica no sentido descendente refletida pela superfície, enquanto que $[1-\varepsilon_i(\theta,\varphi)]R_{sl_i\downarrow}$ corresponde à REM espalhada pela atmosfera no sentido descendente e que também é refletida pela superfície. O termo $\rho_{b_i}(\theta,\varphi,\theta_s,\varphi_s)E_i\, cos(\theta_s)\, \tau_i(\theta_s,\varphi_s)$ refere-se à REM solar incidente refletida pela superfície (LI *et al.*, 2013b; TANG; LI, 2014).

As trajetórias percorridas pela REM até alcançar o sensor orbital, descritas nas Eq. 4 e 5, são representadas na Figura 2.

Figura 2 – Ilustração da aproximação da RTE na região do infravermelho.

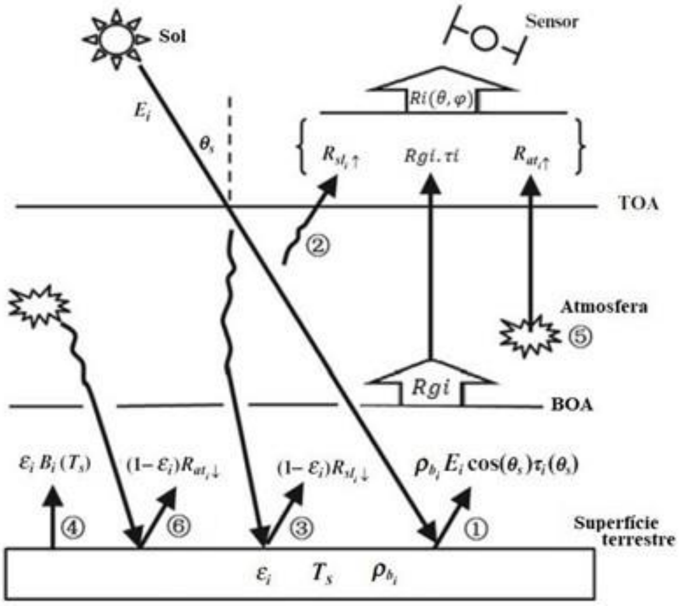

Fonte: Adaptado de Tang e Li (2014).

Como mencionado anteriormente, $R_i(\theta, \varphi)$ é a radiância medida pela banda do sensor no TOA. O caminho ① representa a radiância solar diretamente refletida pela superfície na BOA. Os caminhos ② e ③ são radiâncias espalhadas pela atmosfera no sentido ascendente e descendente, respectivamente. O caminho ④ refere-se à radiância emitida diretamente pela superfície. Os caminhos ⑤ e ⑥ correspondem à radiância emitida pela atmosfera no sentido ascendente e descendente, respectivamente (LI *et al.*, 2013b; TANG; LI, 2014).

No sensoriamento remoto do infravermelho termal, a contribuição solar direta representada pelos caminhos 1, 2 e 3 na Figura 2 pode ser negligenciada sem perda de acurácia (LI *et al.*, 2013b; TANG; LI, 2014). Nesse contexto, a RTE (Equação 4) é matematicamente simplificada e a radiância medida pelo sensor no TOA em um comprimento de onda efetivo é estimada por:

$$L_{\lambda\, sens} = \left[\varepsilon_\lambda B_\lambda(Ts) + (1-\varepsilon_\lambda){L_\lambda}^{\downarrow}\right]\tau_\lambda + {L_\lambda}^{\uparrow} \quad (6)$$

Onde $L_{\lambda\, sens}$ é a REM infravermelha captada pelo sensor ($Wm^{-2}sr^{-1}\mu m^{-1}$), ε_λ é a emissividade espectral (adimensional), ${L_\lambda}^{\downarrow}$ e ${L_\lambda}^{\uparrow}$ correspondem à radiância emitida pela atmosfera, respectivamente, no sentindo descente e ascendente ($Wm^{-2}sr^{-1}\mu m^{-1}$). τ_λ é a transmitância (adimensional), λ é o comprimento de onda, Ts é a temperatura da superfície (K) e $B_\lambda(Ts)$ é a radiância emitida por um corpo negro com temperatura igual à da superfície Ts, isto é, a LST ($Wm^{-2}sr^{-1}\mu m^{-1}$) (DASH *et al.*, 2002; HOOK *et al.*, 1992; LI *et al.*, 2013b; SOBRINO; JIMÉNEZ-MUÑOZ; PAOLINI, 2004; TANG; LI, 2014).

3.3 Série Landsat

A série Landsat permite uma oportunidade de estudar tendências de longo prazo de LST (1982 – presente) com resolução espacial de 60 a 120 metros (Figura 3) (KAISER *et al.*, 2022; MALAKAR *et al.*, 2018).

Figura 3 – Linha do tempo das missões Landsat de registro no TIR.

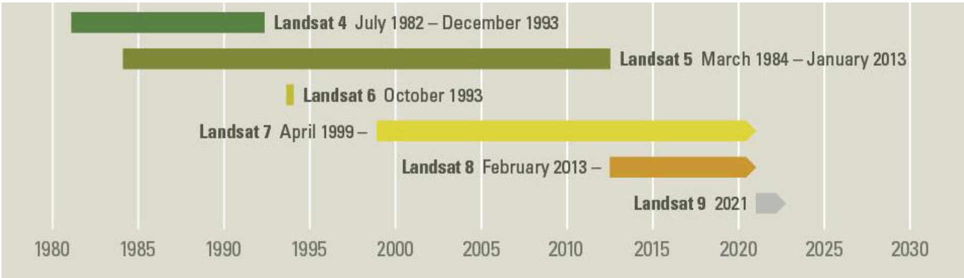

Fonte: USGS, 2022.

O registro de dados de radiância no infravermelho termal iniciou com o Landsat 4 (1982-1993) com uma única banda (10.4-12.5 µm). Em seguida, as plataformas do Landsat 5 (1984-2013) e 7 (1999-6 de abril de 2022) mantiveram uma única banda termal com resolução espectral de 10.4-12.5 µm e resolução espacial de 100 metros (Landsat 5) e 60 metros (Landsat 7) (IHLEN, 2019; LARABY; SCHOTT, 2018; MALAKAR *et al.*, 2018). O Landsat 6 foi lançado em 1993, porém não conseguiu orbitar.

O Landsat 8 foi lançado em 2013 e, até agora, vem mapeando continuamente a superfície da Terra em resolução espacial moderada. Ele carrega dois sensores a bordo, *o Operational Land Imager* (OLI) e o *Thermal Infrared Sensor* (TIRS). O TIRS registra dados em duas bandas: a banda 10 (10.6-11.19 µm) e a banda 11 (11.5-12.51 µm) com resolução espacial de 100 metros reamostrada para 30 metros (IHLEN, 2019; MALAKAR *et al.*, 2018).

O Serviço Geológico dos Estados Unidos (*United States Geological Survey – USGS*) recomendou que a banda 11 não deve ser utilizada devido aos altos erros de calibração produzidos pelo problema de *stray light* (IHLEN, 2019; MALAKAR *et al.*, 2018; MONTANARO *et al.*, 2014). No entanto, é importante mencionar que um algoritmo para o corrigir foi proposto e validado durante 2015-2017 (GERACE; MONTANARO, 2017; GERACE; MONTANARO; ROHRBACH, 2015). Recentemente, em 2021, foi lançado o Landsat 9 levando a bordo o OLI-2 e o TIRS-2 que são versões aprimoradas dos sensores do Landsat 8.

3.4 Estimativa da LST a partir de dados de satélite

A LST refere-se à temperatura radiométrica derivada da radiação emitida pela superfície na região do TIR (DASH *et al.*, 2002; NORMAN; BECKER, 1995; SEKERTEKIN, 2019; TANG; LI, 2014). Do ponto de vista do satélite, o sensor visualiza diferentes materiais de composição e geometria variadas (NORMAN; BECKER, 1995). Nesse sentido, a LST pode ser definida como o conjunto de temperaturas radiométricas desses materiais, contidas em um pixel (DASH *et al.*, 2002; NORMAN; BECKER, 1995; TANG; LI, 2014)

Os dados TIR medidos por sensores orbitais estão diretamente associados à LST através da RTE (Equação 6) (LI *et al.*, 2013b; SOBRINO; JIMÉNEZ-MUÑOZ; PAOLINI, 2004; TANG; LI, 2014). Entretanto, a radiância que alcança o sensor depende dos parâmetros da superfície (temperatura e emissividade) e recebe contribuição dos efeitos de absorção e emissão atmosférica (LI *et al.*, 2013b; SOBRINO; JIMÉNEZ-MUÑOZ; PAOLINI, 2004; TANG; LI, 2014).

O principal problema relacionado à estimativa da LST é que a RTE é matematicamente indeterminada. Um sensor com *n* bandas espectrais possui *n* medidas de radiância e n+1 variáveis. Ainda que realizada uma acurada correção dos efeitos atmosféricos não será possível solucionar a RTE, pois o número de variáveis desconhecidas é maior que o número de equações (DASH *et al.*, 2001; LI *et al.*, 2013b; ROLIM *et al.*, 2016; TANG; LI, 2014)

Nesse contexto, suposições e restrições têm sido realizadas na RTE dando origem a diversos métodos que permitiram a estimativa da LST com dados TIR (DASH *et al.*, 2001; LI *et al.*, 2013b; ROLIM *et al.*, 2016; TANG; LI, 2014). Dentre as suposições impostas pelos métodos, por exemplo, uma ou mais emissividades devem ser conhecidas para poder solucionar a RTE (DASH *et al.*, 2001; GILLESPIE *et al.*, 1998; HOOK *et al.*, 1992; LI *et al.*, 2013b; TANG; LI, 2014).

3.5 Métodos de canal único (*Single Channel – SC*)

De maneira geral, uma das formas de classificar os métodos de estimativa da LST está relacionada ao número de bandas utilizadas. Os métodos de canal único (SC), que incluem a inversão e solução da RTE, algoritmos como o GSC, ISC e MW, permitem estimar a LST utilizando a radiância medida em uma única banda do sensor (BENMECHETA; ABDELLAOUI; HAMOU, 2014; LI *et al.*, 2013b). Já os métodos, como o SW, estimam a LST utilizando duas ou mais bandas. Em ambas classificações, a emissividade deve ser previamente conhecida.

3.5.1 Equação da Transferência Radiativa (RTE)

A maneira mais consolidada para obter uma acurada LST é invertendo e solucionando a RTE, uma vez que não envolve aproximações adicionais (JIMENEZ-MUNOZ *et al.*, 2009; MALAKAR *et al.*, 2018; SEKERTEKIN; BONAFONI, 2020; SOBRINO; JIMÉNEZ-MUÑOZ; PAOLINI, 2004; TARDY *et al.*, 2016). Sob condições de céu claro e equilíbrio termodinâmico, a inversão da RTE (Equação 6), permite estimar a LST conforme a Equação 7:

$$LST = \frac{K_2}{ln\left(\frac{K_1}{\frac{L_{sens} - L^{\uparrow} - \tau(1-\varepsilon)L^{\downarrow}}{\varepsilon\tau}} + 1\right)} \quad (7)$$

onde a LST é estimada em Kelvin, K_1 e K_2 são constantes de conversão térmica da banda do sensor, respectivamente iguais a 774 e 1321 em $Wm^{-2}sr^{-1}\mu m^{-1}$, ε é a emissividade e L_{sens} a radiância medida no sensor. São parâmetros de correção atmosférica, a transmitância (τ), a radiância no sentido descendente ($L_{\lambda}\downarrow$) e a radiância no sentido ascendente ($L_{\lambda}\uparrow$). A Equação 7 foi formulada para a resposta espectral da banda 10 do Landsat 8, portanto, o comprimento de onda foi removido.

Dentre os fatores que afetam a acurácia da LST, está a obtenção de parâmetros de correção atmosférica de alta qualidade, geralmente obtidos a partir de perfis atmosféricos de radiossondagem. Devido à dificuldade em realizá-la em sincronia com a passagem do satélite, estes perfis vêm sendo substituídos por dados de reanálise (DIAZ *et al.*, 2021; LI *et al.*, 2013b; YANG *et al.*, 2020)

Outros métodos baseados na RTE, como os algoritmos GSC e ISC, têm sido desenvolvidos para reduzir a dependência de radiossondagens na correção atmosférica bem como para tratar das características de vários sensores a bordo de diferentes satélites.

3.5.2 Generalized Single Channel (GSC)

O GSC foi desenvolvido para permitir a estimativa da LST a partir qualquer sensor térmico com *Full-Width Half-Maximum* de aproximadamente 1 µm (JIMENEZ-MUNOZ *et al.*, 2014; JIMÉNEZ-MUNOZ; SOBRINO, 2003; JIMÉNEZ-MUÑOZ; SOBRINO, 2010; SOBRINO; JIMÉNEZ-MUÑOZ; PAOLINI, 2004).

O GSC é baseado na relação linear entre radiância e temperatura obtida pela lei de Planck. Sendo assim, a LST é estimada pela Equação 8.

$$T_s = \gamma\left[\frac{1}{\varepsilon}(\psi_1 L_{sens} + \psi_2) + \psi_3\right] + \delta \tag{8}$$

Em que T_s é a LST em Kelvin, ε é a emissividade, L_{sens} é a radiância medida pelo sensor, e ψ_1, ψ_2, ψ_3 são funções atmosféricas. γ e δ são derivadas da equação de Planck, conforme:

$$\gamma = \left\{\frac{C_2 L_{sens}}{(BT_{TOA})^2}\left[\frac{\lambda^4 L_{sens}}{C_1} + \frac{1}{\lambda}\right]\right\}^{-1} \tag{9}$$

$$\delta = -\gamma L_{sens} + BT_{TOA} \tag{10}$$

em que C_1 é igual a 1,191x10^8 Wµm^{4}m^{-2}sr^{-1} e C_2 é igual a 14387,7 µmK, BT_{TOA} é a temperatura de brilho no TOA e λ é o comprimento de onda efetivo.

Nesse método, o vapor d'água é considerado o principal absorvedor na atmosfera (JIMENEZ-MUNOZ *et al.*, 2014). Dessa forma, as funções atmosféricas (ψ_1, ψ_2 e ψ_3) são estimadas pelas equações (11), (12), e (13), baseadas na relação empírica entre vapor d'água (ω) e parâmetros atmosféricos.

$$\psi_1 = 0.04019\omega^2 + 0.02916\omega + 1.01523 \tag{11}$$

$$\psi_2 = -0.38333\omega^2 - 1.50294\omega + 0.20324 \tag{12}$$

$$\psi_3 = 0.00918\omega^2 + 1.36072\omega - 0.27514 \tag{13}$$

Sendo ψ_1 adimensional, ψ_2 e ψ_3 em unidades de radiância (Wm^{-2}µmsr^{-1}).

3.5.3 Improved Single Channel (ISC)

No ISC, a LST é calculada através das Equações 8, 9 e 10, mencionadas anteriormente. Entretanto, as funções atmosféricas são obtidas em função do vapor d'água (ω) e da temperatura atmosférica média (T_a) (CRISTÓBAL *et al.*, 2009, 2018). Assim, as funções atmosféricas são calculadas de acordo com:

$$\psi_1 = -7.2122\omega^2 + 0.00005{T_a}^2 - 2.452321\omega - 0.026275T_a - 0.00005{T_a}^2\omega + 0.02317T_a\omega + 0.04663T_a\omega^2 - 0.00007{T_a}^2\omega^2 + 4.47297 \tag{14}$$

$$\psi_2 = 89.61569\omega^2 - 0.00038{T_a}^2 + 106.55093\omega + 0.21578T_a + 0.00141{T_a}^2\omega - 0.78444T_a\omega - 0.5732T_a\omega^2 + 0.00091{T_a}^2\omega^2 - 30.37028 \tag{15}$$

$$\psi_3 = -14.65955\omega^2 - 0.0001{T_a}^2 - 79.95838\omega + 0.4181T_a - 0.00091{T_a}^2\omega + 0.54535T_a\omega + 0.09114T_a\omega^2 - 0.00014{T_a}^2\omega^2 - 3.76184 \tag{16}$$

3.6 Produto Landsat de Temperatura da Superfície (produto ST)

O produto ST faz parte da coleção de produto científico Landsat nível 2 (L2SP). Nesse produto, a LST é estimada a partir de dados do Landsat 5, 7, 8 e 9 usando a RTE em conjunto com a abordagem de tabela de consulta de temperatura de brilho (*brightness temperature Lookup Table* – LUT) (COOK *et al.*, 2014; HULLEY; HUGHES; HOOK, 2012; ZANTER, 2018).

Pare gerar o produto ST, os parâmetros de correção atmosférica, emissividade e radiância são necessários. Inicialmente, perfis verticais dos produtos de reanálise *Modern-Era Retrospective Analysis for Research and Applications, Version 2* (MERRA-2) com o *Goddard Earth Observing System Model, Version 5* (GEOS-5) *Forward Processing – Instrument Team* (FP-IT) são adquiridos. As informações contidas nos perfis localizados nas grades que sobrepõem e estão em volta da cena Landsat são interpoladas para a data e horário de registro da cena. Um MDE é utilizado para ajustar as camadas dos perfis. Assim, os parâmetros atmosféricos são calculados adequadamente conforme a elevação encontrada em cada pixel. Após isso, os perfis são introduzidos no MODTRAN para que os parâmetros de correção atmosférica sejam estimados e, por fim, interpolados espacialmente para as coordenadas de cada pixel (ANDERSON; SAUER, 2021; COOK et al., 2014; LARABY; SCHOTT, 2018).

A emissividade é extraída do produto *Advanced Spaceborne Thermal Emission and Reflection Radiometer Global Emissivity Dataset* (ASTER GED). Ela é ajustada para a resposta espectral do sensor Landsat com base na abordagem de regressão de banda larga, que usa coeficientes de regressão derivados de emissividades de bibliotecas espectrais (MALAKAR *et al.*, 2018). Uma vez que o produto ASTER GED fornece uma emissividade média no período de 2000-2008, uma correção da emissividade é necessária para áreas em que o tipo de cobertura foi modificado. Nesse caso, uma nova emissividade é estimada com base na relação linear entre o Índice de Vegetação por Diferença Normalizada (NDVI) e emissividade, usando o NDVI calculado com dados do Landsat e ASTER (ANDERSON; SAUER, 2021; HULLEY; HUGHES; HOOK, 2012; MALAKAR *et al.*, 2018).

O último requisito para estimar a LST é a radiância medida pelo sensor. Esta é obtida a partir da banda térmica (banda 10 para o produto ST do Landsat 8) após a calibração radiométrica.

Após a obtenção dos parâmetros atmosféricos, emissividade e radiância no sensor, a radiância emitida pela superfície é calculada através da inversão da RTE, conforme mostra a Equação 17.

$$L_{surf} = \frac{\frac{L_{sens} - L^{\uparrow}}{\tau} - (1-\varepsilon)L^{\downarrow}}{\varepsilon} \tag{17}$$

Em que L_{surf} é a radiância emitida pela superfície e substitui o termo $B_\lambda(Ts)$ na RTE, L_{sens} é a radiância medida pelo sensor. τ, $L^{\uparrow}$ e $L^{\downarrow}$ são os parâmetros de correção atmosférica e ε é a emissividade.

Por fim, a LUT de temperatura de brilho é simplesmente “invertida” por interpolação e a LST é calculada, dada a radiância emitida pela superfície estimada pela Equação 17. A LUT consiste em uma tabela de valores de radiâncias *versus* temperaturas. Para construí-la, a equação de Planck é usada para calcular as radiâncias esperadas para a resposta espectral do sensor em uma faixa de temperaturas com intervalos de 0,01 K (ANDERSON; SAUER, 2021; MALAKAR *et al.*, 2018).

Além do produto de LST, bandas adicionais contendo os parâmetros atmosféricos, emissividade e radiância no sensor são fornecidas. Ademais, uma banda de qualidade do produto também é produzida. Ela contém os erros LST, em Kelvin, produzidos por incertezas na estimativa da emissividade, correção atmosférica, instrumento, bem como, presença de nuvens na cena (ANDERSON; SAUER, 2021).

3.7 Correção atmosférica no TIR

Corrigir os efeitos da atmosfera é um passo essencial para a correta utilização dos dados TIR, já que o sinal que deixa um alvo na superfície é tanto atenuado como realçado pela atmosfera. Na estimativa da LST através da RTE, a correção dos efeitos de absorção e emissão da atmosfera são feitos por meio dos parâmetros atmosféricos que são a transmitância e radiâncias ascendente e descendente. Nos algoritmos GSC e ISC, a correção é realizada empregando o vapor d'água e/ou temperatura atmosférica média.

Os perfis verticais são uma fonte confiável para estimar esses dados atmosféricos pois providenciam o real estado da atmosfera com informações de temperatura (K), pressão (hPa), altura geopotencial (m) e umidade relativa (%) (BERK *et al.*, 1998; CRISTÓBAL *et al.*, 2018; DUAN *et al.*, 2018; JIMENEZ-MUNOZ *et al.*, 2014; YANG *et al.*, 2020; YU; GUO; WU, 2014).

A maneira mais acurada para obter perfis verticais atmosféricos é através de radiossondagens. As radiossondas são balões meteorológicos que podem medir parâmetros físicos atmosféricos, como perfis de temperatura, pressão e umidade do ar (RAHIMZADEGAN; MOBASHERI, 2011; HASSANLI; RAHIMZADEGAN, 2019). Um perfil de radiossonda pode caracterizar situações atmosféricas em latitudes e longitudes com alta precisão (YANG *et al.*, 2020). Contudo, o lançamento dessas radiossondas é uma tarefa difícil pois depende de campanha de campo, gasto de recursos e deve ser realizado simultaneamente com a passagem do satélite. Alternativamente, perfis atmosféricos de dados de reanálise podem substituir os perfis de radiossondagem (DIAZ *et al.*, 2020, 2021; DUAN *et al.*, 2018; MENG; CHENG, 2018; TARDY *et al.*, 2016; YANG *et al.*, 2020).

Os dados de reanálise são matrizes de escala global de variáveis meteorológicas de superfície e de distintas camadas da atmosfera. A temperatura do ar e do ponto de orvalho, dados radiação solar, velocidade do vento, precipitação são alguns exemplos de variáveis. Essas informações são assimiladas por modelos numéricos a partir de dados observacionais históricos de um longo período de tempo, provenientes de observações climáticas de boias, radiossondagens, aeronaves, navios, satélites, previsões meteorológicas e estações terrestres (DEE *et al.*, 2011; ECMWF, 2020; LARABY, 2017; MENG; CHENG, 2018; YANG *et al.*, 2020). Existem diversos produtos de dados reanálises disponíveis que fornecem diferentes variáveis e possuem diferentes coberturas terrestres e resoluções horizontal, vertical e temporal.

O NCEP/NCAR (National Center for Atmospheric Research's) Reanalysis 1 (R1) (KALNAY *et al.*, 1996) e NCEP/DOE (United States Department of Energy) Reanalysis 2 (R2) (KANAMITSU *et al.*, 2002), NCEP Final Operational Model Global Tropospheric Analyses (NCEP/FNL) (NCEP *et al.*, 2000), NCEP Global Forecast 26 System (GFS) (NCEP *et al.*, 2007), NCEP Climate Forecast System Reanalysis (NCEP/CFSR) (SAHA *et al.*, 2010) e Climate Forecast System Version 2 (NCEP/CFSv2) (SAHA *et al.*, 2014), European Centre for Medium-Range Weather Forecasts (ECMWF) ReAnalysis (ERA-Interim) (DEE *et al.*, 2011) e ERA5 (HERSBACH *et al.*, 2020), Modern Era Retrospective-Analysis for Research and Applications (MERRA) (RIENECKER *et al.*, 2011), e Japanese Reanalysis (JRA) (KOBAYASHI *et al.*, 2015) são exemplos de produtos de dados de reanálise.

Os perfis dos produtos de reanálise NCEP/FNL, utilizados pela ACPC, possuem 26 níveis de pressão atmosférica, são produzidos pelo *Global Data Assimilation System* a cada 6 horas em uma resolução horizontal de 1,0° x 1,0° (BARSI; BARKER; SCHOTT, 2003; SAHA *et al.*, 2014; YANG *et al.*, 2020). Os perfis derivados do NCEP/CFSv2 são mais modernos (2011-presente) e refinados, possuem resolução vertical de 37 níveis, horizontal de 0,5º x 0,5º e temporal de 6 horas.

Os dados de reanálise do MERRA-2, fornecidos pela NASA, são gerados usando o *Goddard Earth Observing System Model, Version 5 (GEOS-5)* combinado com o *Atmospheric Data Assimiliation System*. Os perfis atmosféricos possuem 42 níveis de pressão e são produzidos de 3-3 horas em grades com resolução horizontal de 0.625° x 0.5° (ANDERSON; SAUER, 2021; YANG *et al.*, 2020). Os produtos NCEP e MERRA-2 têm sido utilizados como fonte de dados na correção atmosférica com resultados satisfatórios na estimativa da LST (DIAZ *et al.*, 2021; MENG; CHENG, 2018; YANG *et al.*, 2020).

Os perfis verticais extraídos de produtos de reanálise possuem diferentes resoluções vertical, horizontal e temporal. Vários estudos tem comparado diferentes perfis para estimar os parâmetros de correção atmosférica e verificar o efeito dos mesmos no cálculo da LST (MENG; CHENG, 2018; ROSAS; HOUBORG; MCCABE, 2017; YANG *et al.*, 2020). Esses perfis podem ter suas resoluções horizontal e vertical aumentadas utilizando modelos numéricos como o *Weather Research and Forecasting* (WRF). A utilização de perfis de alta resolução na estimativa de parâmetros de correção atmosférica objetivando a estimativa da LST ainda é incipiente.

Nesse contexto, o WRF é um modelo de simulação atmosférica de mesoescala de última geração, sendo, atualmente, o mais utilizado no mundo. Ele oferece uma variedade de recursos para uma ampla gama de aplicações na previsão/simulação de sistemas terrestres como hidrologia, poluição atmosférica, furacões, energia solar e eólica, incêndios florestais, simulações climáticas e meteorologia urbana (POWERS *et al.*, 2017; SKAMAROCK *et al.*, 2021).

No WRF, o processo para realizar as simulações atmosféricas se divide em três etapas: a primeira, destina-se a configurar os domínios do modelo, isto é, inserir os dados de entrada e preparar as condições iniciais e de contorno; já a segunda consiste na execução do modelo numérico propriamente dito; e a terceira etapa é a de pós-processamento e visualização dos dados (POWERS *et al.*, 2017; SKAMAROCK *et al.*, 2021).

É na primeira etapa em que as informações geográficas, como topografia e uso do solo, são extraídas. Além disso, é nesta etapa que os dados atmosféricos, necessários para definir as condições iniciais no modelo (por exemplo, os dados de (re)análise de um modelo global), são incorporados, reformatados e interpolados para os domínios configurados pelo usuário (POWERS *et al.*, 2017; SKAMAROCK *et al.*, 2021).

3.7.1 Parâmetros Atmosféricos

Os parâmetros de correção atmosférica são amplamente estimados através de um Modelo de Transferência Radiativa (MTR) como o MODTRAN, desenvolvido pelo *U.S. Air Force Research Laboratory* em parceria com a *Spectral Sciences Incorporation*. Esse modelo é capaz de simular a propagação da REM entre 0,2 e 100 µm considerando a absorção, emissão, espalhamento e reflexão molecular na atmosfera (BERK *et al.*, 1998; DIAZ *et al.*, 2021; LARABY, 2017).

Para estimar os valores de transmitância, radiâncias ascendente e descendente (τ_λ,$L_\lambda{}^{\uparrow}$, $L_\lambda{}^{\downarrow}$), o MODTRAN requer como *input* inicial um perfil atmosférico com dados de temperatura do ar, umidade relativa e níveis de pressão cobrindo da superfície até o sensor (0-100 Km). Entretanto, estas informações são fornecidas até, aproximadamente, 30 Km por perfis de reanálise ou de radiossondagem. Assim, esses perfis são complementados (30 a 100 Km) com dados de atmosfera padrão disponibilizados pelo modelo. Além disso, os três parâmetros produzidos devem ser integrados para a resposta espectral da banda utilizada na estimativa da LST (BARSI; BARKER; SCHOTT, 2003; LARABY, 2017; MALAKAR *et al.*, 2018; TARDY *et al.*, 2016).

A Calculadora de Parâmetros de Correção Atmosférica (*Atmospheric Correction Parameter Calculator - ACPC*) criada por Barsi et al. (2005) e Barsi; Barker; Schott (2003) produz automaticamente os parâmetros de correção atmosférica para qualquer local e horário. A ACPC utiliza perfis de reanálise NCEP/FNL, em conjunto com MODTRAN, para calcular os valores de τ_λ,$L_\lambda{}^{\uparrow}$, $L_\lambda{}^{\downarrow}$ com resposta espectral para os satélites Landsat 5, 7 e 8 (banda 10). Esta ferramenta é de fundamental importância já que permite estimar os parâmetros no momento da passagem do satélite.

3.7.2 Estimando o vapor d'água e a temperatura atmosférica média

O vapor d'água (ω) e a temperatura atmosférica média (T_a), nos algoritmos GSC e ISC, são alternativas ao uso dos parâmetros atmosféricos para estimar a LST. Para calcular ω e T_a não é necessário o uso de um MTR. De acordo Leckner (1978), o cálculo do vapor d'água pode ser realizado conhecendo-se a umidade relativa e a temperatura próxima à superfície (Equação 18), dados que são obtidos a partir de um perfil atmosférico.

$$\omega = \frac{0.493\varphi_r P_S}{T_o} \qquad (18)$$

Onde ω é o vapor d'água em g.cm^{-2}, φ_r é a umidade relativa e T_o é a temperatura (K), ambos extraídos da primeira camada do perfil atmosférico. P_S é a pressão parcial dada por:

$$P_S = exp\left(26.23 - \frac{5416}{T_o}\right) \qquad (19)$$

QIN, KARNIELI e BERLINER (2001) encontraram funções lineares entre a temperatura atmosférica média (T_a) e a temperatura próxima à superfície (T_o) fornecida por perfis verticais de atmosfera padrão do MODTRAN (*Mid-latitude winter* e *summer*). De acordo com os autores, T_a pode ser estimada para o verão (Eq. 20) e para o inverno (Eq. 21), em condições de céu claro, conforme as formulações:

$$T_a = 16.011 + 0.9262T_o \tag{20}$$

$$T_a = 19.2704 + 0.91118T_o \tag{21}$$

3.8 Estimativa da emissividade para utilização no cálculo da LST

3.8.1 Emissividade obtida com espectroradiômetro

A emissividade de um alvo pode ser medida com alta acurácia utilizando um espectroradiômetro como o *Fourier-transform Infrared* (μFTIR; 102F model). Esse instrumento registra a radiância em um intervalo de 2 a 16 μm com resolução espectral de 4.8 ou 16 cm-1, a emissividade espectral pode ser calculada conforme a equação (D&P INSTRUMENTS, 2006):

$$\varepsilon_\lambda = \frac{L_\lambda - L_\lambda^{\downarrow}}{B_\lambda(Ts) - L_\lambda^{\downarrow}} \tag{22}$$

Em que L_λ é a radiância do alvo, $L_\lambda^{\downarrow}$ é a radiância atmosférica descendente medida com uma placa de ouro de emissividade igual a 0,04 e $B_\lambda(Ts)$ é a radiância derivada da equação de Planck.

3.8.2 Estimando a emissividade com base no NDVI

A emissividade é um dos fatores determinísticos na acurácia da LST, diversos métodos tem sido desenvolvidos para estimá-la a partir de dados de satélite. Todavia, esta tarefa torna-se difícil em alvos heterogêneos, como exemplo as áreas urbanas, devido às diferentes coberturas do solo com emissividades específicas que podem estar contidas em um único pixel (LI *et al.*, 2013b; SOBRINO *et al.*, 2008a; TANG; LI, 2014). Dentre os métodos de estimativa de emissividade a partir de dados de satélite, os baseados no Índice de Vegetação por Diferença Normalizada (*Normalized Difference Vegetation Index – NDVI*) tem se mostrado os mais apropriados para aplicação na LST (DUAN *et al.*, 2020; KAFER *et al.*, 2019; MALAKAR *et al.*, 2018; SEKERTEKIN; BONAFONI, 2020; SOBRINO *et al.*, 2008b; WAN; ZHU; DING, 2021; ZHOU *et al.*, 2011).

O método de limiar do NDVI (*Normalized Difference Vegetation Index threshold - NDVI^{THM}*) considera a relação estatística (alta correlação) entre a emissividade e o NDVI, índice que pode ser facilmente calculado utilizando as bandas do vermelho (*red*) e infravermelho próximo (*Near Infrared - NIR*), conforme Equação 23:

$$NDVI = \frac{\rho_{NIR} - \rho_{red}}{\rho_{NIR} + \rho_{red}} \quad (23)$$

onde ρ_{NIR} é a reflectância da banda do infravermelho próximo e ρ_{red} é a reflectância da banda vermelha.

A partir do NDVI é possivel calcular a porção de área vegetada (P_V) de acordo com a Equação 24:

$$P_V = \left(\frac{NDVI - NDVI_{min}}{NDVI_{max} - NDVI_{min}}\right)^2 \quad (24)$$

Onde *NDVI* é o valor do índice calculado para o pixel, $NDVI_{min}$ = 0,2 e $NDVI_{max}$ = 0,5 em um contexto global (SOBRINO *et al.*, 2008b; SOBRINO; JIMÉNEZ-MUÑOZ; PAOLINI, 2004).

A estimativa da emissividade através do método *NDVI^{THM}* é dada, portanto, através dos três seguintes casos (SEKERTEKIN; BONAFONI, 2020; SOBRINO *et al.*, 2008b; VAN DE GRIEND; OWE, 2007):

Se $NDVI < NDVI_{min}$, o pixel é considerado solo exposto e a emissividade pode ser calculada pela Equação 25, utilizando a reflectância da banda vermelha (ρ_{red}).

$$\varepsilon = 0.979 - 0.035\rho_{red} \quad (25)$$

Se $NDVI > NDVI_{max}$, o pixel é inteiramente vegetado e assume a emissividade da vegetação ($\varepsilon = 0.99$).

Se $NDVI_{min} \leq NDVI \leq NDVI_{max}$, trata-se de um pixel misturado (contem solo e vegetação). Nesse caso, a emissividade do pixel é determinada pela Equação 26, utilizando a porção de área vegetada obtida com a Equação 24.

$$\varepsilon = 0.004P_V + 0.986 \quad (26)$$

A garantia do bom desempenho do método *NDVI*^{THM} depende de algumas suposições, são elas: 1) A superfície é composta apenas por vegetação e solo; 2) a emissividade do solo exposto pode ser linearmente representada pela reflectância extraída da banda vermelha e; 3) a emissividade varia linearmente em relação a porção de vegetação no pixel (LI *et al.*, 2013a; SOBRINO; RAISSOUNI, 2010; VAN DE GRIEND; OWE, 2007). Dentre as vantagens desse método estão a fácil aplicação, o que permitiu seu uso em vários sensores, e a não necessidade de correção atmosférica para cálculo do NDVI (LI *et al.*, 2013b; SOBRINO; RAISSOUNI, 2010).

4 ÁREA DE ESTUDO

Para esse estudo, duas áreas no estado do Rio Grande do Sul (RS), Brasil, foram selecionadas: o Aeroporto Internacional de Porto Alegre (SBPA) e o campo de dunas de Cidreira localizado no litoral norte entre os municípios de Cidreira e Tramandaí.

O SBPA possui uma estação em que radiossondas são lançadas duas vezes ao dia (00:00 e 12:00 UTC) gerando perfis verticais com informações de temperatura do ar, pressão e umidade relativa em 99 níveis verticais. Essa característica tornou esse local ideal para avaliar os perfis atmosféricos extraídos de dados de reanálise, bem como, refinados por modelo atmosféricos.

Figura 4 – Localização da estação de radiossondagem SBPA do Aeroporto Internacional de Porto Alegre.

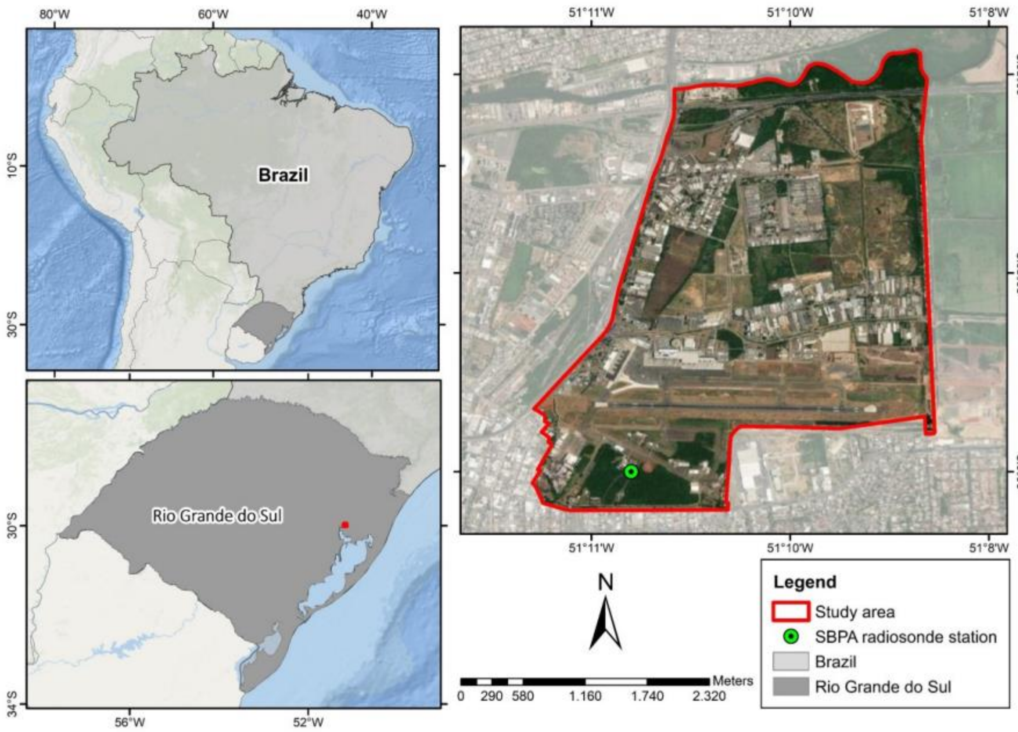

A área selecionada abrange os limites oficiais do bairro Anchieta, com área de cerca de 9,2 km^2 (Figura 4). Segundo a classificação climática de Köppen, o clima local é subtropical úmido com verões quentes (Cfa) (KÖPPEN, 1918), com temperatura média anual do ar de 19,6º C, umidade relativa média anual de 76,1% e precipitação média anual de 1397 mm.

A segunda área consiste em um campo de dunas transgressivas de Cidreira, conforme mostra a Figura 5. É considerado um sítio experimental com aproximadamente 30 km^2 de areias finas (tamanhos entre 125-250 µm) compostas por 99,53% de quartzo (SiO_2) e 0,47% de minerais pesados (KAFER *et al.*, 2019; PITTIGLIANI; ROLIM, 2017). Por ser um alvo pseudo-invariante com emissividade conhecida, este ambiente é adequado para avaliar métodos de estimativa da LST.

Figura 5 – Campo de dunas de Cidreira localizada no litoral norte do Rio Grande do Sul.

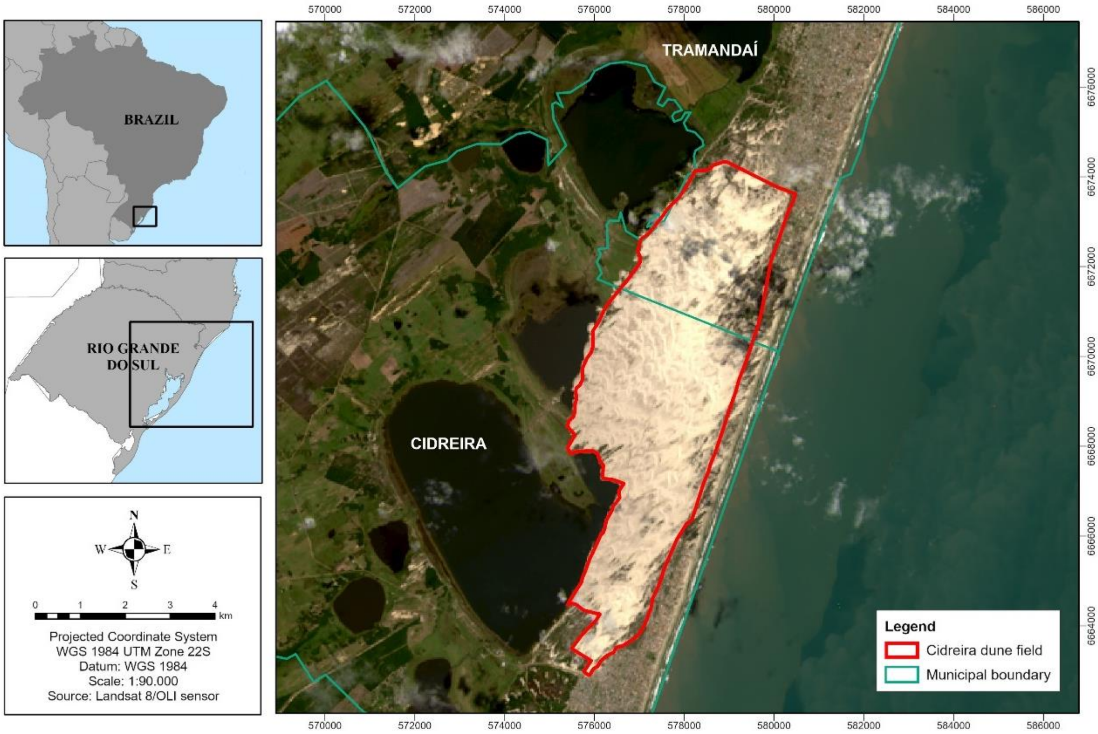

A região das dunas de Cidreira está localizada na Zona Subtropical Sul e é influenciada por fatores dinâmicos como as massas marítimas e fatores estáticos como o relevo (PAZ, 2015). Segundo Köppen (1918), o clima é temperado e úmido com chuvas bem distribuídas ao longo do ano, não caracterizando uma estação seca definida.

5 MÉTODOS

Nessa pesquisa, dois artigos científicos foram desenvolvidos para alcançar os objetivos.

O primeiro artigo avaliou diferentes perfis verticais, extraídos de dados de reanálise NCEP, na correção atmosférica e estimativa da LST. Nesse estudo, a LST foi calculada através da RTE e os parâmetros de correção atmosférica foram estimados a partir de: (i) perfil vertical extraído diretamente do produto de reanálise NCEP CFSv2; (ii) perfil vertical do NCEP CFSv2 com resolução horizontal refinada para 12 Km através do modelo WRF; (iii) perfil vertical do NCEP CFSv2 com resolução horizontal refinada para 3 Km; (iv) calculadora de correção atmosférica ACPC que utiliza perfil de reanálise NCEP FNL. Os perfis i, ii e iii foram introduzidos no

MODTRAN para estimar os três parâmetros de correção atmosférica. As principais etapas são mostradas na Figura 6.

Para avaliar os diferentes perfis como fonte de dados atmosféricos, parâmetros de correção atmosférica e LST calculados a partir das informações fornecidas pelos perfis das radiossondagens do SBPA foram utilizados como valores de referência.

Figura 6 – Utilização de diferentes perfis atmosféricos para obtenção dos parâmetros de correção atmosférica e da LST.

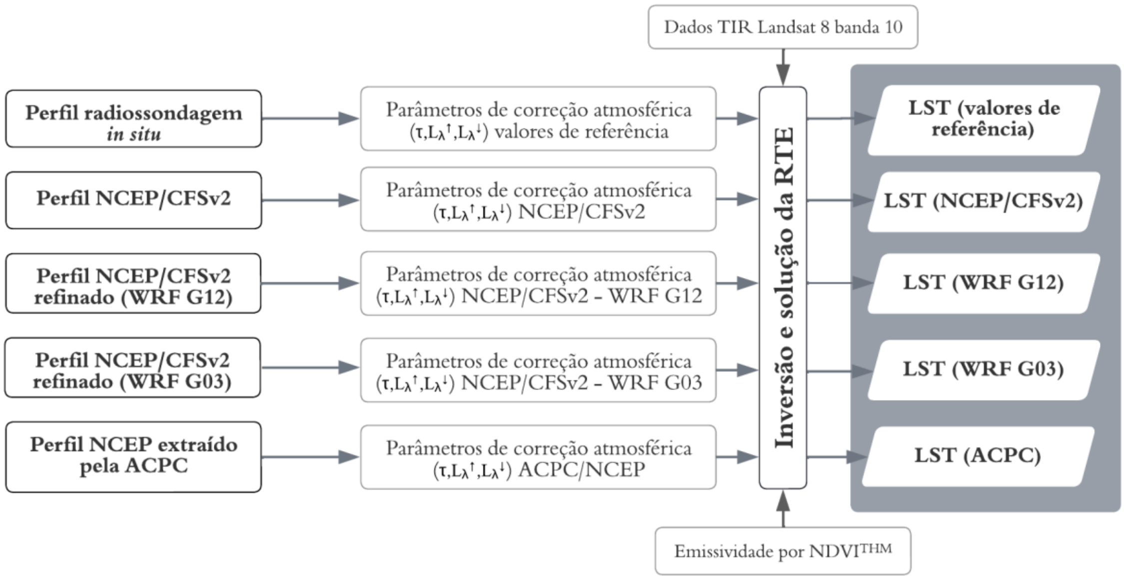

Esse primeiro artigo teve o intuito de embasar a avaliação dos métodos de estimativa da LST, realizada no segundo artigo, no sentido de conhecer qual o perfil vertical de dados de reanálise NCEP é o mais adequado para a correção atmosférica no infravermelho termal. Destaca-se que os perfis de reanálise NCEP CFSv2 de resolução original precisaram ser baixados e também refinados através do WRF. Em seguida, necessitaram ser convertidos e processados no MODTRAN para, então, integrar e estimar os parâmetros de correção atmosférica. Partindo de um ponto de vista prático, a calculadora ACPC da NASA, em relação aos procedimentos realizados com os perfis NCEP CFSv2, apresenta algumas vantagens, pois, além de ser uma ferramenta online de livre acesso, automaticamente extrai os perfis NCEP FNL, os processa no MODTRAN, e estima os três parâmetros de correção atmosférica para uma data, local e horário específico e reposta espectral da plataforma Landsat selecionada.

O segundo artigo objetivou avaliar o desempenho dos algoritmos GSC, ISC e o produto Landsat 8 de Temperatura da Superfície (produto ST) na estimativa da LST sobre o campo de dunas de Cidreira. Para tanto, as LSTs estimadas pelos algoritmos e pelo produto foram comparadas com a LST obtida pela inversão da RTE. Essa equação foi solucionada empregando dados de campo confiáveis obtidos em sincronia com a passagem do satélite. Sendo assim, os parâmetros de correção atmosférica foram calculados a partir das informações fornecidas pelo perfil de radiossondagem e a emissividade estimada com espectroradiômetro em campo. Visando as vantagens oferecidas pela ACPC, os dados atmosféricos aplicados no GSC e ISC foram estimados a partir das informações interpoladas pela ferramenta. As etapas para estimativa da LST, bem como os dados de entrada utilizados em cada um dos métodos são mostradas na Figura 7.

Figura 7 – Etapas para validação dos métodos GSC, ISC e produto ST.

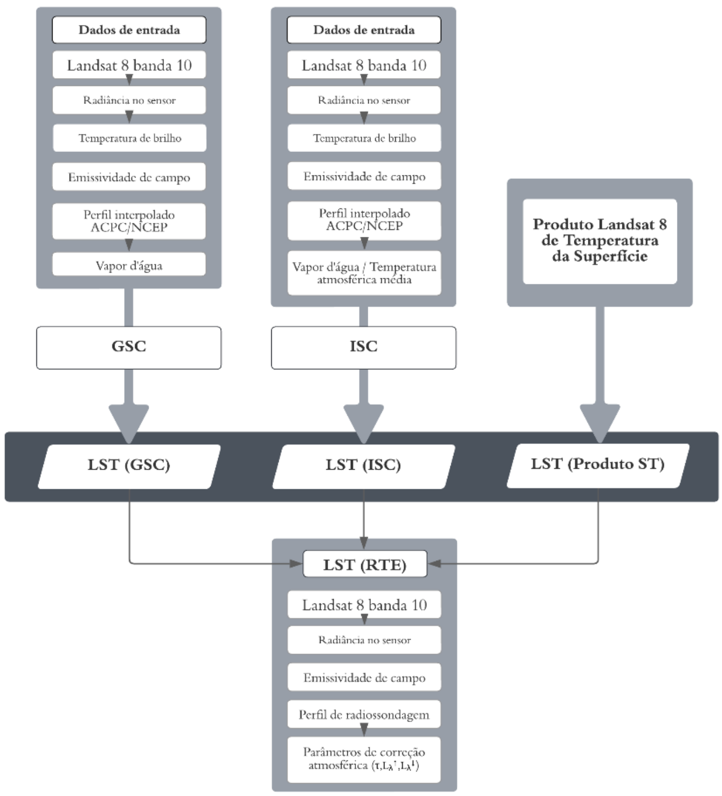

As estimativas realizadas nesta pesquisa foram implementadas através de linguagem Python. Os métodos utilizados são apresentados detalhadamente em cada um dos artigos.

6 RESULTADOS E DISCUSSÕES

6.1 ARTIGO 01: Land Surface Temperature Retrieval Using High-Resolution Vertical Profiles Simulated by WRF Model.

O artigo intitulado “*Land Surface Temperature Retrieval Using High-Resolution Vertical Profiles Simulated by WRF Model*” foi publicado na revista *Atmosphere*. Este trabalho foi importante para conhecer, dentre os perfis derivados de dados de reanálise NCEP, qual o mais adequado para ser aplicado na correção atmosférica e posterior estimativa da LST. Os resultados obtidos nesse artigo foram importantes para dar seguimento à avaliação dos algoritmos GSC, ISC e produto ST, abordada no segundo artigo, pois possibilitou determinar qual a fonte de dados atmosféricos ideal para ser utilizada nos algoritmos de canal único.

atmosphere

Article

Land Surface Temperature Retrieval Using High-Resolution Vertical Profiles Simulated by WRF Model †

Lucas Ribeiro Diaz [1,2,*], Daniel Caetano Santos [3], Pâmela Suélen Käfer [1], Nájila Souza da Rocha [1], Savannah Tâmara Lemos da Costa [1], Eduardo Andre Kaiser [1] and Silvia Beatriz Alves Rolim [1]

1 State Research Center for Remote Sensing and Meteorology (CEPSRM), Universidade Federal do Rio Grande do Sul (UFRGS), Av. Bento Gonçalves 9500, Porto Alegre 91501-970, RS, Brazil; pamelaskafer@gmail.com (P.S.K.); najila.rocha@ufrgs.br (N.S.d.R.); savannah.lemos@ufrgs.br (S.T.L.d.C.); kaiser-eduardo@hotmail.com (E.A.K.); silvia.rolim@ufrgs.br (S.B.A.R.)
2 Faculty of Science, Vrije Universiteit Amsterdam, de Boelelaan 1085, 1081 HV Amsterdam, The Netherlands
3 Center for Natural and Exact Sciences, Department of Physics, Universidade Federal de Santa Maria (UFSM), Av. Roraima, Santa Maria 97105-900, RS, Brazil; danielcae@gmail.com
* Correspondence: l.ribeiro.diaz@vu.nl

† This paper is an expanded version of the work presented at the 4th International Electronic Conference on Atmospheric Sciences: Diaz, L.R.; Santos, D.C.; Käfer, P.S.; Rocha, N.S.d.; Costa, S.T.L.d.; Kaiser, E.A.; Rolim, S.B.A. Atmospheric Correction of Thermal Infrared Landsat Images Using High-Resolution Vertical Profiles Simulated by WRF Model. *Environ. Sci. Proc.* **2021**, *8*, 27. https://doi.org/10.3390/ecas2021-10351.

Abstract: This work gives a first insight into the potential of the Weather Research and Forecasting (WRF) model to provide high-resolution vertical profiles for land surface temperature (LST) retrieval from thermal infrared (TIR) remote sensing. WRF numerical simulations were conducted to downscale NCEP Climate Forecast System Version 2 (CFSv2) reanalysis profiles, using two nested grids with horizontal resolutions of 12 km (G12) and 3 km (G03). We investigated the utility of these profiles for the atmospheric correction of TIR data and LST estimation, using the moderate resolution atmospheric transmission (MODTRAN) model and the Landsat 8 TIRS10 band. The accuracy evaluation was performed using 27 clear-sky cases over a radiosonde station in Southern Brazil. We included in the comparative analysis NASA's Atmospheric Correction Parameter Calculator (ACPC) web-tool and profiles obtained directly from the NCEP CFSv2 reanalysis. The atmospheric parameters from ACPC, followed by those from CFSv2, were in better agreement with parameters calculated using in situ radiosondes. When applied into the radiative transfer equation (RTE) to retrieve LST, the best results (RMSE) were, in descending order: CFSv2 (0.55 K), ACPC (0.56 K), WRF G12 (0.79 K), and WRF G03 (0.82 K). Our findings suggest that there is no special need to increase the horizontal resolution of reanalysis profiles aiming at RTE-based LST retrieval. However, the WRF results were still satisfactory and promising, encouraging further assessments. We endorse the use of the well-known ACPC and recommend the NCEP CFSv2 profiles for TIR atmospheric correction and LST single-channel retrieval.

Keywords: thermal infrared (TIR); atmospheric correction; reanalysis; Landsat; radiative transfer equation (RTE); NCEP CFSv2; numerical weather prediction (NWP)

Citation: Diaz, L.R.; Santos, D.C.; Käfer, P.S.; Rocha N.S.d.; Costa S.T.L.d.; Kaiser, E.A.; Rolim, S.B.A. Land Surface Temperature Retrieval Using High-Resolution Vertical Profiles Simulated by WRF Model. *Atmosphere* **2021**, *12*, 1436. https://doi.org/10.3390/atmos12111436

Academic Editor: Anthony R. Lupo

Received: 2 October 2021
Accepted: 27 October 2021
Published: 30 October 2021

1. Introduction

Land surface temperature (LST) is one of the essential climate variables (ECVs) of the Global Climate Observing System (GCOS) [1,2]. It is closely connected to Earth–atmosphere interactions, playing a pivotal role in surface energy and water balances at both local and global scales [3–5]. Therefore, LST is a key parameter in a wide range of environmental applications [6]: urban heat island studies [7]; numerical weather prediction [8]; agricultural, forests and drought monitoring [9–11]; monitoring of geothermal activity and natural hazards [12,13]; evapotranspiration estimation [14,15];

fire detection [16,17]; water resource management [18,19]. It is worth mentioning that the LST should not be confused with the near-surface air temperature (typically measured by meteorological/in situ stations); the LST refers to the so-called “skin temperature” [10].

Thermal infrared (TIR) remote sensing is a one-off way of obtaining the LST at regional and global scales [20–22]. However, the spectral radiance measured by the TIR sensors on board satellites is influenced not only by the surface parameters (emissivity and temperature) but also by the composition and structure of the atmosphere (mainly water vapor) [23,24]. Thus, these atmospheric effects must be removed for the appropriate use of TIR remote sensing data in temperature research applications [4,25,26]. The atmospheric correction (AC) is, in general terms, the conversion of top-of-the-atmosphere (TOA) to ground-level measurements. Neglecting the AC leads to systematic errors in the LST estimation for any atmosphere [24,27].

One of the widely applied methodologies for AC and LST retrieval is the physics-based radiative transfer equation (RTE) method [28]. It involves a simple inversion of the RTE for a particular channel and can provide theoretically accurate LST retrieval [23]. The RTE approach requires vertical atmospheric profiles (air temperature, water vapor, and pressure). This information is introduced into a radiative transfer model (RTM) to calculate the three atmospheric parameters necessary for AC: atmospheric transmittance, upwelling atmospheric radiance, and downwelling atmospheric radiance [24,29]. In situ radiosonde profiles launched simultaneously with the satellite overpass are ideal for AC [30,31]. Nevertheless, this kind of profile is unavailable under most realistic conditions [20,32,33], as local radiosonde launching has a significant financial cost [23,24]. Radiosonde stations with atmospheric-profile databases are launched daily around the globe (e.g., in airports). However, these data may be either non-synchronous or too far away from the scene footprint [4,34]. Hence, local radiosondes are mainly suitable for particular local studies and validation at specific sites [21,35].

Therefore, atmospheric profile products from different sources have been used as surrogate radiosondes in TIR atmospheric correction, resulting in LSTs with acceptable accuracy [4,26,36–39]. Satellite-derived profiles overcome the spatial limitations of local radiosondes. These are available at the satellite pixel scale, providing data over a large spatial extent. Although they have a high spatial resolution, the satellite-derived profiles can be compromised by low temporal coverage (only at the satellite overpassing time) [21,40]. Thus, the results may not be favorable when the sensor of interest is not (or not concurrent with) the one from which the profiles are derived [26,32]. Overcoming this temporal limitation, profiles from global reanalysis data provide a flexible temporal resolution (typically 3 and 6 hourly) and are a practical alternative to the radiosonde’s spatial constraint [21]. Reanalysis datasets are global gridded extended homogeneous time series, with no spatial or temporal gaps [41].

Barsi et al. (2005, 2003) [27,29] proposed an atmospheric web-based correction tool (Atmospheric Correction Parameter Calculator—ACPC) for Landsat 5, 7, and 8 thermal bands. It uses reanalysis profiles from the National Centers for Environmental Prediction (NCEP) and the code of the moderate resolution atmospheric transmission (MODTRAN) model [42] to directly provide the three atmospheric parameters for AC. Additionally, researchers have evaluated and compared the efficacy of different reanalysis and satellite-based profile products for AC/LST retrieval. NCEP reanalyses (Reanalysis 1 [43] and FNL [44]) and a moderate resolution radiometer (MODIS) atmospheric profiles product (MOD07) [45] were analyzed for different sites in Spain [24,33,46] and in China [47], for TIR sensors such as Landsat, ASTER, and HJ-1B IRS. Coll et al. (2012) [32], in Spain, added the satellite-based profiles from Atmospheric Infrared Sounder (AIRS) [48] to the comparison. Rosas et al. (2017) [21] also included the European Centre for Medium-Range Weather Forecast’s (ECMWF) ERA-Interim reanalysis product [49] along with previous profiles for Landsat 8 LST estimates in Saudi Arabia. More recently, assessments with a greater number of different profile products were carried out. Meng and Cheng (2018) [20] evaluated reanalysis products from Modern-Era Retrospective Analysis for Research and Applications (MERRA) [50] 1 and 2, ERA-Interim, NCEP FNL and NCEP Reanalysis 2 [51], and Japanese Reanalysis (JRA-55) [52]. Their validation included profiles distributed around the globe and 32 Landsat 8 band 10 images over China. Yang et al. (2020) [40] assessed seven profile sources (AIRS, MOD07, ERA-Interim, MERRA 2, and NCEP's FNL, Reanalysis 2, and GFS) using 17 radiosonde stations over Europe and in situ LST measurements in China. Overall, the accuracies of AC parameters and retrieved LST data using satellite-derived profiles were lower than those using reanalysis methods [32,33,40,46,47].

However, reanalysis profiles also have their disadvantages. The spatial resolution of several degrees (varying for each product) can be considered low. The accuracy is usually poorer for regions with less coverage of permanent observatories, such as the oceans and many Southern Hemisphere zones [41,53,54]. Since the data are spaced at grid points with time intervals commonly of 6 h, the description of meteorological phenomena on a sub-grid or variable time scale may be affected [55]. On the other hand, modern numerical weather models benefit from computing performance and physical processes parameterization in downscaling the reanalysis data. Mesoscale atmospheric models use global (re)analysis models as initial and boundary conditions for local applications [56,57]. Lee et al., (2020) [58] employed high-resolution (1.5 and 12 km) Numerical Weather Prediction (NWP) models distributed by the Korea Meteorological Administration (KMA) as input atmospheric data for AC and sea surface temperature estimation with visible infrared imaging radiometer suite (VIIRS) bands. Their KMA NWP dataset is restricted to eastern Asia, but the approach of using high-resolution NWP models combined with RTM provides an interesting background for studies of TIR remote sensing atmospheric correction.

The Weather Research and Forecasting (WRF) model [59] is an atmospheric modeling system designed for both research and NWP. It is a state-of-the-art mesoscale model and the world's most widely used model for these purposes. Non-hydrostatic, open-source, free, community-based, and with a wide range of parameterization options, the WRF model provides a spectrum of capabilities for a variety of applications in atmospheric science and weather prediction [60]. Hence, the WRF model has been extensively employed for estimating high-resolution meteorological data [61–66].

It is imperative to assess whether the use of the WRF model to generate high-resolution atmospheric vertical profiles, in conjunction with an RTM, results in a higher AC/LST retrieval accuracy. Moreover, almost all studies that evaluated different profile sources for LST retrieval were performed over Asia and Europe. To the best of our knowledge, no study has carried out such an assessment in South America. There is also a lack of studies using newer and better reanalysis profiles (e.g., ERA5 [67] and NCEP Climate Forecast System Version 2 (CFSv2) [68]) for AC and LST estimation [38,69].

This study conducted simulations with the WRF model using NCEP CFSv2 reanalysis data as initial and boundary conditions. Its objective was to generate high-resolution vertical profiles, improving the spatial, temporal, and vertical resolutions of the global reanalysis. The intention was to investigate the utility of these profiles in TIR atmospheric correction and LST retrieval, in relation to the ACPC web-tool and profiles extracted directly from the NCEP CFSv2 reanalysis. We used Landsat 8 TIRS band 10 as an example to retrieve LST values through an RTE inversion-based algorithm in conjunction with the MODTRAN radiative transfer model. The accuracy assessment was performed using local radiosonde observations in Southern Brazil.

2. Materials and Methods

2.1. Study Area and in Situ Radiosonde Data

The Porto Alegre International Airport (SBPA), Rio Grande do Sul State, Brazil was selected as the study area. The airport includes a radiosonde station, which made this site a useful environment for studies that aimed to evaluate atmospheric profiles. The selected area covers the official limits of the Anchieta district [70], with an area of around 9.2 km^2

(Figure 1). According to Köppen's climate classification, the local climate is subtropical humid with hot summers (Cfa) [71], with a mean annual air temperature of 19.6 °C, mean annual relative humidity of 76.1%, and mean annual precipitation of 1397 mm [72].

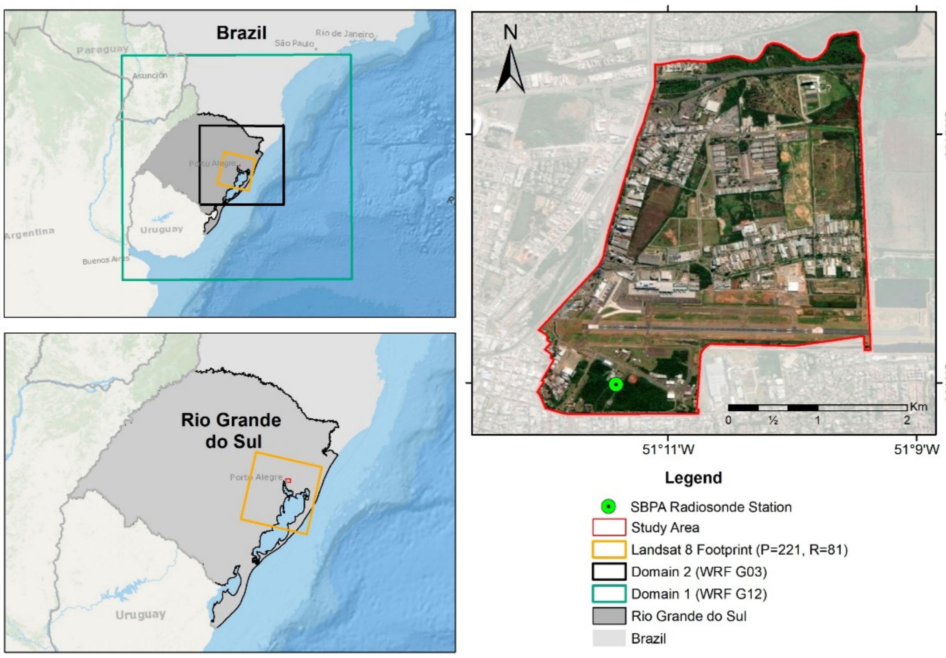

Figure 1. Map of the study area showing the Porto Alegre Airport (SBPA) radiosonde station, Southern Brazil, and the WRF nested grids.

The SBPA station is located at 30.00° S and 51.18° W, 3.0 m above mean sea level, and its identifier number is 83971. In this station, radiosondes are launched twice a day, at 00:00 and 12:00 UTC. In this study, we used the 12:00 UTC radiosonde profiles, as this is the closest time to the Landsat 8 crossing time over the study site (~13 UTC). Data were obtained from the University of Wyoming website (http://weather.uwyo.edu/upperair/sounding.html, accessed on 28 October 2021). This dataset allows the vertical structure of the atmosphere to be characterized, with profiles of air temperature, pressure, and humidity with up to 99 vertical levels. The radiosonde observations, as well as the parameters calculated from them, are considered as ground truth for the assessments in this study.

2.2. Landsat 8 Satellite Data and Case Days

The Landsat mission has been providing moderate-resolution space-based surface observations for almost 50 years. Landsat 8 is the most recent operational satellite of the series and was launched in February 2013. It carries a two-sensor payload: the Operational Land Imager (OLI), which has nine reflective (visible, near-infrared, and short-wave infrared) bands with a 30 m spatial resolution and the Thermal Infrared Sensor (TIRS) with two bands in the TIR region. The TIRS bands have a 100 m spatial resolution but it is resampled and provided at 30 m by the United States Geological Survey (USGS), to be consistent with the OLI bands [73,74].

In this study, we acquired all Landsat 8 images (Collection 1) available under daily clear-sky conditions over the study area from 2013 to 2019. This resulted in a total of 27 scenes at Path-Row 221-81 (Figure 1), with an acquisition scene center time around 13:20 UTC. The full-swath Landsat data were reduced to a subset for a 10,184-pixel region covering the study area of Figure 1. Table 1 presents the specifications of the Landsat 8 data utilized in the study, as well as the case days that henceforward will be used to refer to each dataset. Seeking to illustrate the meteorological conditions near the acquisition time, we also include in Table 1 the air temperature and the water vapor content in the atmosphere, using the precipitable water vapor (PWV) data for the entire radiosonde column measured by the SBPA station. TIRS band 10 (10.60–11.19 µm) was used for RTE-based LST retrieval (Section 2.6.2) and OLI bands 4—red (0.64–0.67 µm) and 5—near-infrared (0.85–0.88 µm) for land surface emissivity estimation (Section 2.5).

Table 1. Information about Landsat 8 data used in the paper (27 images from 2013 to 2019, Path-Row 221-81). The last columns present meteorological conditions measured by the SBPA station.

Scene ID	Acquisition Date	Case Day	Season	Air T [°C]	PWV [g/cm²]
LC82210812013322LGN01	18 November 2013	1	spring	23	1.57
LC82210812013338LGN01	4 December 2013	2	spring	21	2.43
LC82210812014037LGN01	6 February 2014	3	summer	31	4.10
LC82210812014293LGN01	20 October 2014	4	spring	19.8	1.18
LC82210812014341LGN01	7 December 2014	5	spring	26.6	1.99
LC82210812015024LGN01	24 January 2015	6	summer	24.4	2.66
LC82210812015056LGN01	25 February 2015	7	summer	24.6	3.26
LC82210812015312LGN01	8 November 2015	8	spring	24.4	2.79
LC82210812016075LGN01	15 March 2016	9	summer	22.8	2.23
LC82210812016235LGN02	22 August 2016	10	winter	9.4	0.91
LC82210812016347LGN01	12 December 2016	11	summer	23.4	3.27
LC82210812017093LGN01	3 April 2017	12	autumn	22	3.31
LC82210812017173LGN00	22 June 2017	13	winter	10.6	1.85
LC82210812017205LGN00	24 July 2017	14	winter	13.4	1.93
LC82210812017237LGN00	25 August 2017	15	winter	22.2	2.82
LC82210812017317LGN00	13 November 2017	16	spring	20	1.83
LC82210812017349LGN00	15 December 2017	17	spring	25.2	3.17
LC82210812018048LGN00	17 February 2018	18	summer	23.4	2.36
LC82210812018112LGN00	22 April 2018	19	autumn	19	3.26
LC82210812018160LGN00	9 June 2018	20	autumn	6.6	0.84
LC82210812018240LGN00	28 August 2018	21	winter	9.4	0.60
LC82210812018272LGN00	29 September 2018	22	spring	23	3.60
LC82210812018320LGN00	16 November 2018	23	spring	23.6	1.74
LC82210812019083LGN00	24 March 2019	24	autumn	25.8	2.53
LC82210812019099LGN00	9 April 2019	25	autumn	19.6	1.72
LC82210812019227LGN00	15 August 2019	26	winter	10.8	1.08
LC82210812019323LGN00	19 November 2019	27	spring	24.8	2.33

2.3. Reanalysis Data

The NCEP Climate Forecast System version 2 (CFSv2) [68] reanalysis data are produced using the NCEP Global Forecasting System (GFS) atmospheric model and the Gridpoint Statistical Interpolation (GSI) analysis system with three-dimensional variational data assimilation (3D-Var). This is arranged in grids with a horizontal resolution of 0.5° × 0.5° and in 37 vertical (pressure) levels (1000—1 mbar), with 0.205° for surface parameters. We used CFSv2 reanalysis data from the 6-hourly product as initial and boundary conditions for the WRF simulations. In addition, profiles retrieved directly from NCEP CFSv2 were included in the analysis, to assess the WRF model downscaling performance. These profiles were extracted from the grid point closest to the SBPA station.

2.4. WRF Model Configuration

The WRF model version 4.1.2 with the advanced research WRF (ARW) dynamical solver [59,75] was used to perform high-resolution numerical simulations. We configured the WRF domains with two nested grids, in one-way mode, centered at the SBPA station, with horizontal resolutions of 12 km (G12) and 3 km (G03) (4:1 parent grid ratio) (see Figure 1) and 33 sigma vertical levels with 50 hPa as the top pressure value. The time step used for the outermost domain was 72 s with a 4:1 parent ratio. Geographical static data such as land use, topography, albedo, and reflectance, were inserted into the modeling process using the land use categories of USGS.

Some atmospheric physical processes cannot be directly resolved by the numerical model and so need to be parameterized. Parameterization schemes represent the contribution of unresolved but important phenomena in terms of variables resolved at the model discrete grid [76–78]. The WRF model has a vast range of parameterization scheme options. The physics parameterization chosen for our simulations included: Purdue Lin microphysics parameterization [79]; the Yonsei University (YSU) Planetary Boundary Layer (PBL) scheme [80]; the Betts–Miller–Janjic (BMJ) cumulus scheme [81]; Dudhia shortwave radiation [82]; the Rapid Radiative Transfer Model (RRTM) longwave radiation option [83]; the Unified NOAH Land-Surface Model (LSM) [84]; the revised MM5 surface-layer scheme [85]. In Diaz et al. (2021) [86], some parametrization options were tested for the same SBPA area, and the set used here is based on these results and those of Santos and Nascimento (2016) [87]. The WRF configurations are summarized in Table 2 [88].

Table 2. Overview of WRF model setting.

WRF Model Configuration	
Version	4.1.2
Dynamical solver	ARW
Boundary conditions	NCEP CFSv2
Map projection	Lambert
Grid size	Domain 1: (119 × 116) × 33 Domain 2: (169 × 165) × 33
Horizontal resolution	Domain 1: 12 km Domain 2: 3 km
Nesting	One-way
Time step	72 s
Static geographical data	USGS
Cloud Microphysics	Purdue Lin
Planetary Boundary Layer (PBL)	Yonsei University (YSU)
Cumulus	Betts–Miller–Janjic (BMJ) [1]
Shortwave Radiation	Dudhia
Longwave Radiation	Rapid Radiative Transfer Model (RRTM)
Land Surface Model (LSM)	Unified NOAH
Surface-layer	Revised MM5

[1] Domain 1 only.

The WRF model was run using the above configurations for each of the case days in Table 1. We conducted simulations of 24 h duration starting at 00:00 UTC and the resulting profiles were extracted at 12:00 UTC for the grid point closest to the SBPA station, to match with the local radiosonde observations. Hence, the first 12 h of the simulation was considered to be spin-up time. The model output for each domain was stored every 30 min.

2.5. Land Surface Emissivity Estimation

Land surface emissivity (LSE) is one of the key parameters for retrieving LST from remote sensing data. It is a measure of the surface's intrinsic ability to convert heat energy into radiant energy. LSE is a function of the composition, roughness, and moisture of the surface and the observation conditions [74,89,90]. Among the methods for LSE retrieval from space, those based on the normalized difference vegetation index (NDVI) are operational and are the most frequently applied, with satisfactory results [89,91–96]. Sekertekin and Bonafoni (2020a, 2020b) [74,97] examined the influence of six NDVI-based LSE models on the performance of LST retrieval. Based on their results, we opted to use the NDVI threshold method ($NDVI^{THM}$) of Sobrino et al. (2008) [91]. The LSE estimation from satellites inevitably has errors and NDVI-based methods also have their limitations, especially in urban environments [98]. However, a recent study [99] reported that the use of LSE data estimated by different methods resulted in no significant variations in the LST accuracy. Nevertheless, assessing the LSE estimation is beyond the scope of this paper.

To calculate the NDVI from Landsat 8 data, the first step is to convert the digital number (DN) values of bands 4 (red) and 5 (near-infrared—NIR) to reflectances using Equation (1) [97,100]:

$$\rho_\lambda = \frac{M_p \cdot Q_{CAL} + A_p}{\sin \theta_{SE}} \tag{1}$$

where ρ_λ is the reflectance of the corresponding band, M_p is the multiplicative rescaling factor of the corresponding band, Q_{CAL} is the calibrated and quantized standard product of pixel values (DNs), A_p is the additive rescaling factor of the corresponding band, and θ_{SE} is the local sun elevation angle.

Then, the NDVI is obtained from Equation (2):

$$NDVI = \frac{\rho_{NIR} - \rho_R}{\rho_{NIR} + \rho_R} \tag{2}$$

where ρ_{NIR} is the reflectance of the NIR band and ρ_R is the reflectance of the red band. It is not necessary to correct the atmospheric effects in the red and NIR bands to estimate LSE [101].

From the NDVI, it is possible to calculate the fractional vegetation cover (P_V) from Equation (3) [102]:

$$P_V = \left[\frac{NDVI - NDVI_{min}}{NDVI_{max} - NDVI_{min}}\right]^2 \tag{3}$$

where $NDVI_{min}$ = 0.2 and $NDVI_{max}$ = 0.5 in a global context [30,91,103]. The P_V is an important factor in the LSE estimation.

The $NDVI^{THM}$ proposed by (Sobrino et al., 2008) [91] estimates the LSE considering three different cases as presented in Equation (4), for Landsat 8 [74]:

$$\varepsilon = \begin{cases} 0.979 - 0.035\rho_R & NDVI < 0.2 \\ 0.004P_V + 0.986 & 0.2 \le NDVI \le 0.5 \\ 0.99 & NDVI > 0.5 \end{cases} \tag{4}$$

where ε is the land surface emissivity (LSE). For NDVI < 0.2, the pixel is considered to be bare soil, and the emissivity is calculated using the reflectance of the red band. In the second case (0.2 ≤ NDVI ≤ 0.5), the pixel is considered to be composed of a mixture of bare soil and vegetation and the LSE depends on the P_V value. The pixels with NDVI values higher than 0.5 are considered to be fully vegetated areas and the emissivity is assumed to be 0.99.

2.6. Atmospheric Correction and LST Retrieval

2.6.1. Atmospheric Parameters Calculation with MODTRAN and ACPC

MODTRAN (moderate resolution atmospheric transmission) is a commercial and widely employed atmospheric RTM developed by the U.S. Air Force and Spectral Sciences Inc. [42]. The present study used the MODTRAN4 v3r1 [104] to estimate the three atmospheric correction parameters (i.e., atmospheric transmittance, upwelling atmospheric radiance, and downwelling atmospheric radiance) in the Landsat TIR spectrum. We introduced into the MODTRAN as input, vertical profiles of pressure, air temperature, and relative humidity from: (i) SBPA radiosonde; (ii) NCEP CFSv2 reanalysis; (iii) WRF G12; (iv) WRF G03. The atmospheric parameters calculated from SBPA profiles were treated as ground truth data.

The methodology of Barsi et al. (2003) [29] was adopted to fulfill the profiles. To predict space-reaching atmospheric parameters, MODTRAN requires atmospheric profiles reaching "space", or 100 km above sea level. Since the radiosondes and NCEP CFSv2 stretch from the surface to about 30 and 50 km, respectively, the upper atmosphere layers (to 100 km) were extracted from the MODTRAN standard atmospheres and pasted into our site-specific profiles. We used the standard mid-latitude summer profile [105] for case days in hot seasons (spring and summer) and the mid-latitude winter profile [106] for those in cold seasons (autumn and winter). The WRF-simulated profiles refined the NCEP CFSv2 profiles by increasing the number of levels in the portion of the atmosphere closest to the surface. The model was set up with the top pressure level at 50 hPa (~18 km). Thus, these profiles were completed first with the remaining levels from the reanalysis and then, starting at 50 km, with MODTRAN standard atmospheres.

This approach results in surface-to-space vertical profiles of air temperature, pressure, and water vapor. The profiles constructed for MODTRAN from the NCEP CFSv2 reanalysis count 40 (43) vertical levels in the warm (cold) seasons. Using WRF, the number of vertical levels in the filled profiles increases to 45 (48). The radiosondes describe the atmospheric profile in more detail, but the number of vertical levels varies, averaging 88 and reaching 109 in our final profiles. These completed profiles were inserted into a MODTRAN input file and then processed [27,29].

MODTRAN outputs are provided in the model's spectral resolution, so an integration must be performed between the bounds defined by the spectral response curve of the sensor band (Equation (5)) [4]:

$$\mathrm{var}\,(\lambda_i) = \frac{\int_{\lambda_{i,min}}^{\lambda_{i,max}} \mathrm{var}\,(\lambda) R_s(\lambda) d\lambda}{\int_{\lambda_{i,min}}^{\lambda_{i,max}} R_s(\lambda) d\lambda} \tag{5}$$

where R_s is the spectral response of the sensor at the center wavelength λ_i of a band with a spectral window of $\lambda_{i,min}$–$\lambda_{i,max}$ and var alternatively denotes the atmospheric parameter (transmittance, upwelling, or downwelling radiance) value extracted from the MODTRAN output file, between the wavelengths $\lambda_{i,min}$ and $\lambda_{i,max}$. In this case, the spectral response curve is from the Landsat 8 TIRS band 10 (TIRS10).

Additionally, we included in the comparative analysis the atmospheric parameters estimated by NASA's well-established Atmospheric Correction Parameter Calculator (ACPC) web-tool [27,29]. As mentioned above, the ACPC uses NCEP reanalysis profiles (with 1° × 1° horizontal resolution and 28 vertical levels), MODTRAN code, and a suite of integration algorithms to provide the AC parameters for the particular date, time, and location inputted. The reanalysis profiles used by ACPC are to about 30 km, so they are fulfilled using MODTRAN standard atmospheres. Completed ACPC profiles have 33 vertical levels. The mid-latitude standard upper profiles varied according to the season of each case day. The option of using the atmospheric profile from the closest integer coordinate to the inputted location (SBPA station) was set.

2.6.2. Radiative Transfer Equation (RTE)-Based LST Retrieval Method

The inverse solution of the RTE [28] is a direct and a priori the most appropriate procedure for LST retrieval using a single TIR band [101]. The RTE applied to a particular TIR band/wavelength (λ) can be simplified and given by:

$$L_\lambda^{sen} = \left[\varepsilon_\lambda B_\lambda(T_s) + (1-\varepsilon_\lambda)L_\lambda^{\downarrow}\right]\tau_\lambda + L_\lambda^{\uparrow} \quad (6)$$

where L_λ^{sen} ($W{\cdot}m^{-2}{\cdot}sr^{-1}{\cdot}\mu m^{-1}$) is the at-sensor (TOA) spectral radiance of the corresponding TIR band (in this paper, TIRS10), ε_λ refers to the LSE (dimensionless), B_λ ($W{\cdot}m^{-2}{\cdot}sr^{-1}{\cdot}\mu m^{-1}$) is the black body radiance, T_s (Kelvin) represents the LST, $L_\lambda^{\downarrow}$ and $L_\lambda^{\uparrow}$ ($W{\cdot}m^{-2}{\cdot}sr^{-1}{\cdot}\mu m^{-1}$) refer to the downwelling and upwelling radiances, respectively, and τ_λ is the atmospheric transmittance (dimensionless). Hence, the emitted radiance for a black body at a temperature T_s is given by the inversion of Equation (6):

$$B_\lambda(T_s) = \frac{L_\lambda^{sen} - L_\lambda^{\uparrow} - \tau(1-\varepsilon_\lambda)L_\lambda^{\downarrow}}{\tau_\lambda\varepsilon_\lambda} \quad (7)$$

where the L_λ^{sen} of Landsat 8 TIRS10 is obtained by converting the DN values (Q_{CAL}) applying Equation (8) [100]:

$$L_\lambda^{sen} = M_L \cdot Q_{CAL} + A_L \quad (8)$$

where M_L and A_L are the multiplicative and additive rescaling factors of the corresponding band (TIRS10). In addition, B_λ comes from Planck's law:

$$B_\lambda(T) = \frac{C_1}{\lambda^5\left(e^{C_2/\lambda T} - 1\right)} \quad (9)$$

where C_1 = 1.19104 × 10^8 $W{\cdot}\mu m^4{\cdot}m^{-2}{\cdot}sr^{-1}$ and C_2 = 14,387.7 μm·K are Planck's radiation constants. Thus, T_s is calculated by inverting Planck's law in Equation (7):

$$T_s = \frac{C_2}{\lambda}\left[\ln\left(\frac{C_1}{\lambda^5\left[\frac{L_\lambda^{sen} - L_\lambda^{\uparrow}}{\varepsilon_\lambda\tau_\lambda} - \left(\frac{1-\varepsilon_\lambda}{\varepsilon_\lambda}\right)L_\lambda^{\downarrow}\right]} + 1\right)\right]^{-1} \quad (10)$$

Finally, Equation (10) can be simplified and the LST (T_s) from Landsat 8 TIRS10 is estimated as:

$$LST = \frac{K_2}{\ln\left(\frac{K_1}{\frac{L_\lambda^{sen} - L_\lambda^{\uparrow} - \tau_\lambda(1-\varepsilon_\lambda)L_\lambda^{\downarrow}}{\tau_\lambda\varepsilon_\lambda}} + 1\right)} \quad (11)$$

where K_1 and K_2 refer to calibration constants, whose values for Landsat 8 TIRS10 are 774.89 $W{\cdot}m^{-2}{\cdot}sr^{-1}{\cdot}\mu m^{-1}$ and 1321.08 K, respectively [100]. Henceforth, the spectral notation (λ) will be omitted, since here only a single TIR band is used.

The aforementioned procedure was applied with τ, $L^{\uparrow}$, and $L^{\downarrow}$ calculated using profiles from:

1. SBPA local radiosonde;
2. NCEP CFSv2 reanalysis;
3. WRF G12;
4. WRF G03;
5. ACPC.

The LST images retrieved using the atmospheric parameters from SBPA radiosondes are considered as "ground truth", and LST retrievals considering the other cases were compared to this, as detailed in the next section.

2.7. Metrics for Performance Evaluation

To evaluate the performance of the WRF model and other profiles we take into account the atmospheric parameters (τ, $L^{\uparrow}$, and $L^{\downarrow}$) and LST images. The SBPA radiosondes are the available in situ observations. Hence, the AC parameters and LSTs calculated using SBPA profiles are considered our references. To perform the comparative assessment, the Pearson's correlation coefficient (R), bias (mean error), mean absolute error (MAE), and root mean square error (RMSE) were used as statistical criteria. These metrics are widely employed to evaluate and compare models [31,107,108]. The metrics' equations are given as follows:

$$\mathrm{R} = \frac{\sum_{i=1}^{n}(p_i - \bar{p})(o_i - \bar{o})}{\sqrt{\sum_{i=1}^{n}(p_i - \bar{p})^2}\sqrt{\sum_{i=1}^{n}(o_i - \bar{o})^2}} \tag{12}$$

$$\mathrm{bias} = \frac{1}{n}\sum_{i=1}^{n}(p_i - o_i) \tag{13}$$

$$\mathrm{MAE} = \frac{1}{n}\sum_{i=1}^{n}|p_i - o_i| \tag{14}$$

$$\mathrm{RMSE} = \sqrt{\frac{1}{n}\sum_{i=1}^{n}(p_i - o_i)^2} \tag{15}$$

where p_i and o_i are pairwise predicted and observed values, respectively, n is the number of pairs, and terms with overbars are respective mean values.

R scores range from −1 to 1, and values approaching 1 indicate stronger correlations. Bias is useful in determining if the model is underestimating (bias < 0) or overestimating (bias > 0) the observed values. MAE is the average of the absolute difference between the predictions and the observations, despite model overestimation or underestimation. It is a negatively oriented index (values closer to zero are better). RMSE is also negatively oriented. It indicates the deviation between modeled and observed values and is more sensitive to outliers as the errors are squared before summing.

3. Results and Discussion

3.1. Evaluation of Atmospheric Parameters

3.1.1. Overall Results

The AC parameters (τ, $L^{\uparrow}$, and $L^{\downarrow}$) calculated with different sources of estimated vertical profiles (CFSv2, WRF G12, WRF G03, and ACPC) were compared against those using observational SBPA radiosondes (Figure 2). In Table 3, the accuracies of atmospheric parameter estimations are presented. All the profile sources provide AC parameters with high correlation coefficients, all greater than 0.9 in relation to the reference (SBPA). The R values of ACPC are slightly better, followed by those of CFSv2. There is a general but small tendency to overestimate the transmittance values. On the other hand, the atmospheric radiances tend to be underestimated, except for ACPC downwelling. The smallest biases were from the WRF for all three parameters. The largest were from CFSv2. With respect to MAE and RMSE, the best results were from ACPC followed by CFSv2. The largest RMSE value found was 0.43 $W{\cdot}m^{-2}{\cdot}sr^{-1}{\cdot}\mu m^{-1}$ for the downwelling calculated with WRF G03 profiles.

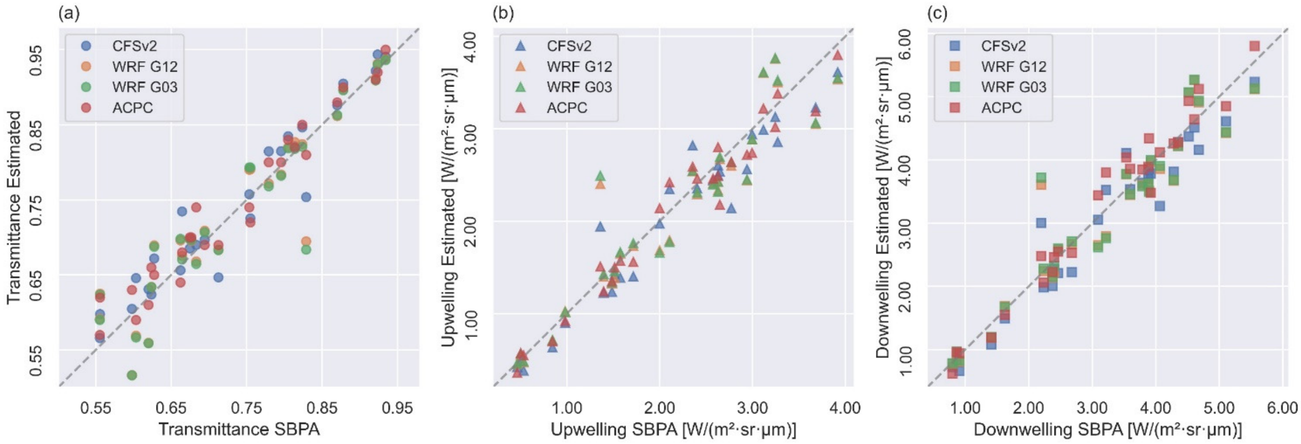

Figure 2. Comparison of (**a**) atmospheric transmittance, (**b**) upwelling radiance, and (**c**) downwelling radiance calculated with SBPA in situ radiosondes and estimated profile sources. The dashed line represents the "1:1 line".

Table 3. Statistical metrics of atmospheric parameters estimated from different atmospheric profiles. Bias, MAE, and RMSE are in the units of the parameter of interest, i.e., $W \cdot m^{-2} \cdot sr^{-1} \cdot \mu m^{-1}$ for atmospheric radiances and the transmittance is dimensionless.

		CFSv2	WRF G12	WRF G03	ACPC
Transmittance	R	0.96	0.93	0.93	0.97
	bias	0.01	0.00	0.00	0.01
	MAE	0.02	0.03	0.03	0.02
	RMSE	0.03	0.04	0.04	0.03
Upwelling	R	0.97	0.94	0.94	0.98
	bias	−0.12	−0.04	−0.02	−0.06
	MAE	0.21	0.24	0.24	0.16
	RMSE	0.27	0.33	0.34	0.20
Downwelling	R	0.97	0.95	0.95	0.98
	bias	−0.15	−0.05	−0.03	0.08
	MAE	0.28	0.30	0.30	0.21
	RMSE	0.35	0.42	0.43	0.27

The higher negative bias of the atmospheric radiances with NCEP CFSv2 in our findings may be due to the fact that these reanalysis profiles have the lowest level at 1000 hPa, which corresponds to around 60–250 m for the SBPA station in our case days. Therefore, the lowest layer of the atmosphere (which typically presents the largest water vapor content and warmest temperature) is neglected in these profiles. This fact was indicated by Coll et al. (2012) [32] and Meng and Cheng (2018) [20]. We tried to reduce this limitation by downscaling the CFSv2 reanalysis profiles with the WRF model. The WRF profiles bring the first level to around 1 m above the surface.

Figure 3 illustrates the performance of the AC parameters from the different profile sources via Taylor diagrams [109]. These quantify the agreement of the modeled profiles with the observational profiles in terms of graphical representations of the three statistics combined: standard deviation, root mean squared deviation (RMSD, the same as RMSE), and correlation coefficient. Figure 3 corroborates the results shown in Table 3. It indicates that ACPC obtained better results than the other profiles for all three atmospheric parameters. Next was the CFSv2 reanalysis profiles. The diagrams clearly point out that the profiles from WRF G12 and G03 had very similar accuracies. In fact, no significant statistical differences were found between the parameters from the WRF grids G12 and G03. This suggests that computation costs can be saved by using profiles from a WRF domain with coarse horizontal resolution. Despite other aims, scholars have already reported this kind of result with WRF model grids [57,110–112].

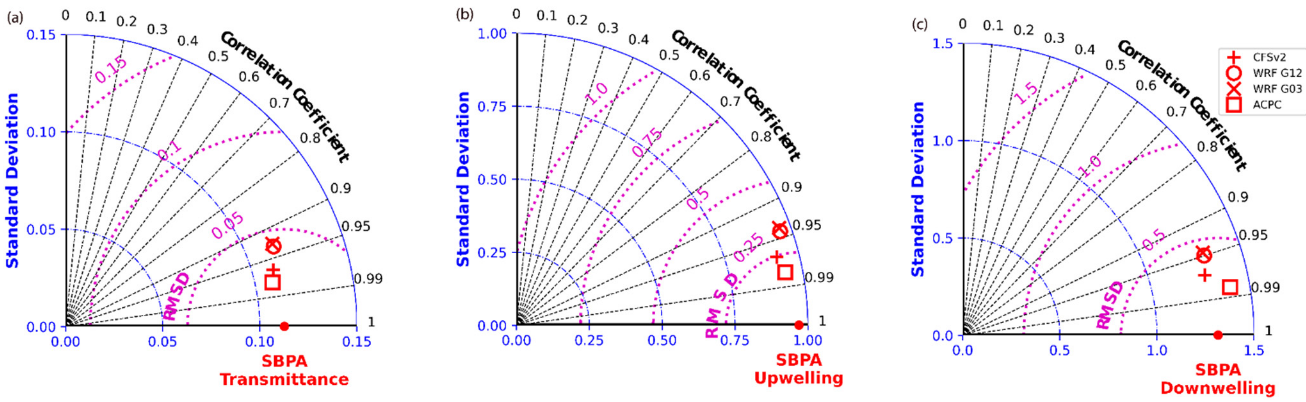

Figure 3. Taylor diagrams of (**a**) atmospheric transmittance, (**b**) upwelling radiance, and (**c**) downwelling radiance. The parameters calculated with SBPA radiosondes are the references. The black dashed lines represent the correlation coefficient (R), blue dash-dot lines represent the standard deviation, and the magenta dotted lines represent the root mean squared deviation (RMSD = RMSE).

Our RMSE range is in agreement with the findings for reanalysis profiles in Meng and Cheng (2018) [20] for the three parameters. The authors analyzed 30,715 atmospheric profiles in 163 stations around the globe. The RMSE values of Yang et al., (2020) [40] were overall slightly lower than ours. However, their assessment only includes profiles from Europe. In Diaz et al. (2021) [85], the vertical distributions of air temperature and water vapor for the SBPA radiosondes, CFSv2 reanalysis, and WRF (G12 and G03) profiles were compared. The evaluation of the profiles themselves showed that both CFSv2 and WRF models skillfully represent the vertical profiles of temperature and water vapor. Nevertheless, the statistical metrics indicated that increasing the horizontal resolution did not significantly improve the quality of the simulated atmospheric profile. This is in line with the above results for the atmospheric parameters comparison.

3.1.2. Analysis by Meteorological Conditions

The errors in the estimation of atmospheric parameters for each case day are shown in Figure 4. This shows that, despite the fact that ACPC presented the best overall metrics, none of the profile sources performed best in all cases. For instance, in eight of the case days, one of the WRF profiles had the best results in calculating the downwelling radiance. For case day 23, the WRF model plainly produced the largest errors, whereas for case days such as day 26, the model successfully reduced the largest error in the driving reanalysis data. Therefore, it is pertinent to assess the dependence of the performances of different profile sources on the meteorological conditions.

Figure 4. Errors in the estimation of (**a**) atmospheric transmittance, (**b**) upwelling radiance, and (**c**) downwelling radiance from the different profiles for each case day.

Figure 5 shows the RMSE values of the AC parameters calculated taking into account specific ranges of precipitable water vapor (PWV) for the entire atmospheric column (measured by SBPA radiosondes) and air temperature observed at the SBPA station (Table 1). The WRF model performs better under dry and cold conditions. It outperforms the other profile sources in the range of 2–3 g/cm² PWV. Under almost all moisture and temperature conditions, the ACPC profiles presented better results than the NCEP CFSv2 profiles. All the different profiles presented minor errors in situations of the lowest water vapor and air temperature. However, it is important to mention that the number of case days under these conditions was less than for the other ranges. This is consistent with the research of Meng and Cheng (2018) [20], where it was noted that the best global RMSEs were for profiles with a water vapor content lower than 1 g/cm². Furthermore, they indicated that the largest RMSEs occurred when the water vapor was between 3 and 4 g/cm². With respect to the air temperature, our results suggest that errors in estimating the atmospheric parameters are higher on warmer days.

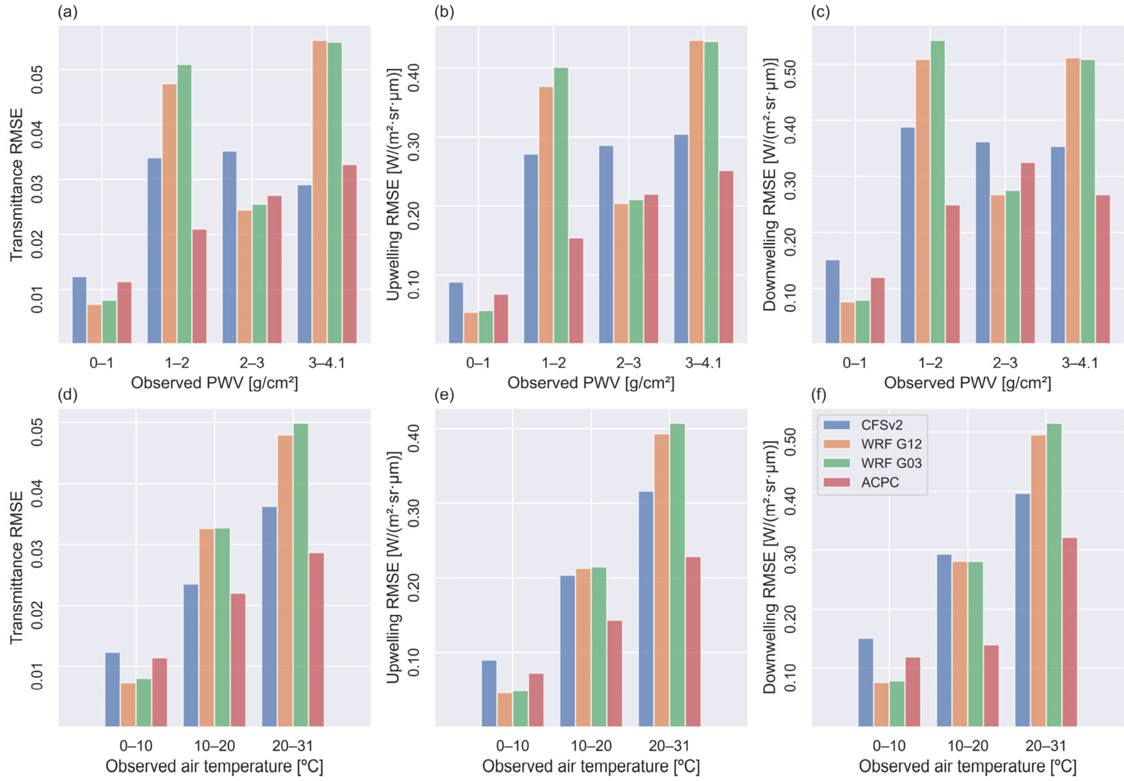

Figure 5. Atmospheric parameters' RMSE values calculated for specific ranges of observed precipitable water vapor (PWV) (**a**–**c**) and air temperature (**d**–**f**).

3.2. Application to RTE-Based LST Retrieval

To further assess the different atmospheric profiles, the LSTs retrieved by RTE inversion with atmospheric parameters, Landsat 8 TIRS10 radiance, and NDVI^{THM} emissivity were compared with each other. Once more, the LST images that used SBPA profiles were assumed as reference data. Except for the atmospheric parameters calculated from the different profile sources, the other variables in Equation (11) were the same for each pixel of the scenes. Therefore, the differences between LST values that were retrieved with SBPA profiles and those from other sources were due to the discrepancies among the profiles [40]. Figure 6 illustrates an example (case day 25) of the LST spatial distribution in the study area. Note that the hottest pixels are over the airstrip and adjacent buildings of the airport.

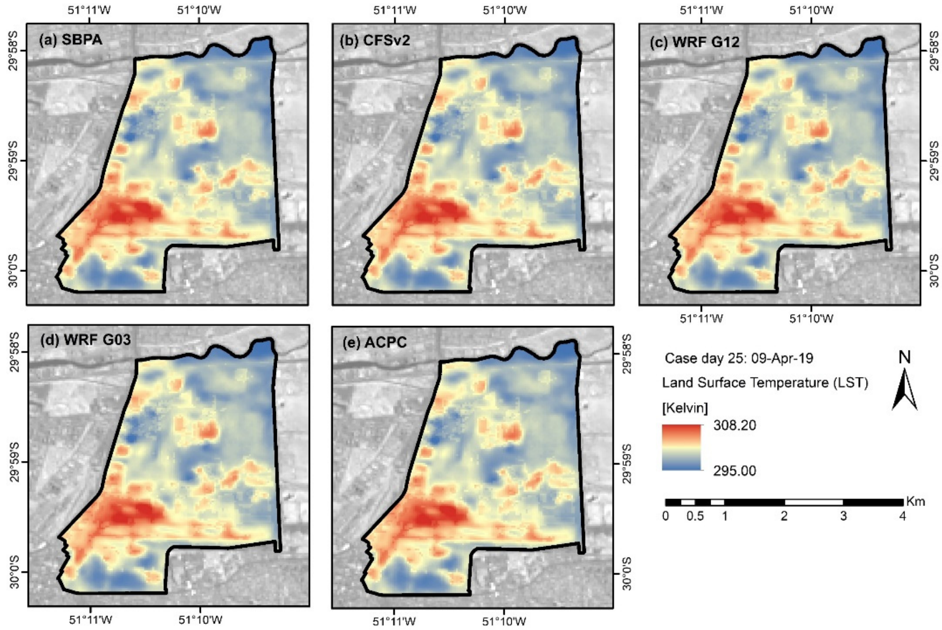

Figure 6. LST images retrieved with atmospheric parameters from (**a**) SBPA, (**b**) CFSv2, (**c**) WRF G12, (**d**) WRF G03, and (**e**) ACPC, for case day 25 (9 April 2019).

Histograms of LST errors for all the 10,184 pixels in the study area of the 27 case days are shown in Figure 7. These represent the frequency distribution of the errors in the retrieval of LST using the different atmospheric profile sources. For all profiles, more than 50% of the errors are in the range of ±1 K. Yang et al. (2020) [40] also found the most LST differences in this range, using different reanalysis and satellite-derived profiles. The histograms in Figure 7b,c indicate that WRF profiles tend to overestimate the LST, whereas ACPC tends to underestimate it (Figure 7d). Using WRF profiles, LST errors can reach to more than 4 K, although only in a very small number of cases. For ACPC and both WRF grids, the error range that occurs most often is between 0 and −1 K. The distribution of CFSv2 LST errors is more symmetrical than in the other profiles.

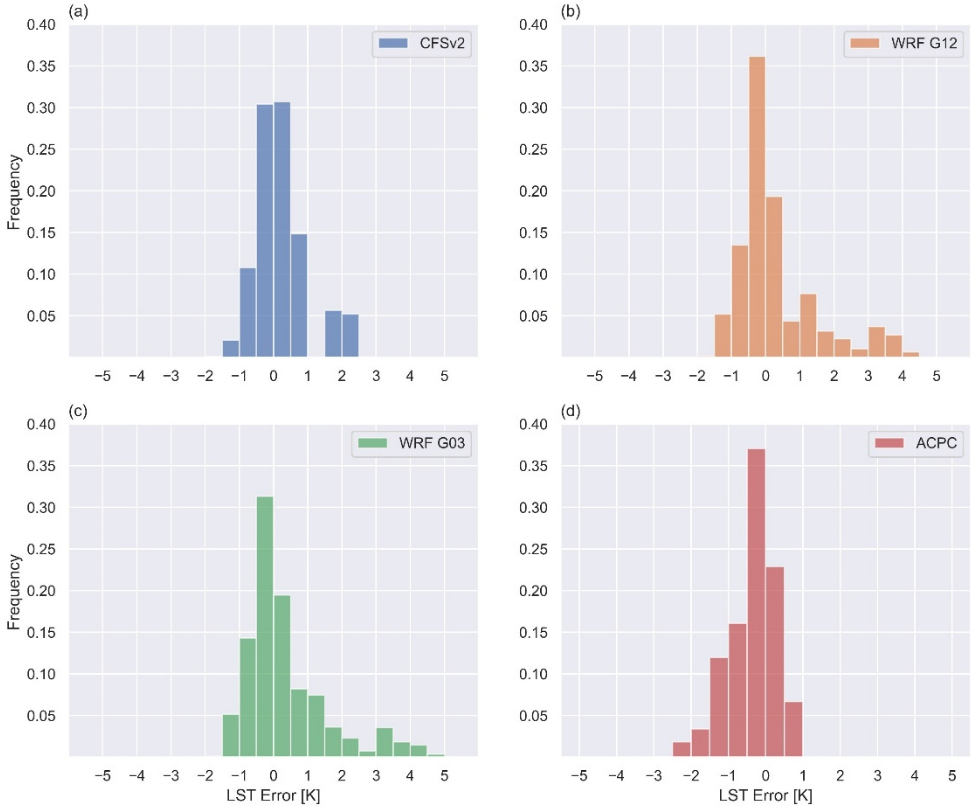

Figure 7. Normalized histograms of the LST errors using profiles from (**a**) CFSv2, (**b**) WRF G12, (**c**) WRF G03, and (**d**) ACPC.

Table 4 summarizes the metrics of the LST retrieval comparative analysis. Overall, the LST values of the four profile sources analyzed in this study were found to be in good agreement with the reference. All of them showed a very strong correlation and relatively low bias, MAE, and RMSE values. CFSv2, WRF G12, and WRF G03 presented an average positive bias and ACPC a negative bias. This corresponds with the histogram analysis in Figure 7. The mean error criteria (MAE and RMSE) indicate that the profiles with the best performance in the AC- and RTE-based LST retrieval are, in descending order: CFSv2, ACPC, WRF G12, and WRF G03. The differences between CFSv2 and ACPC overall MAE and RMSE values were very small, and similarly for WRF G12 and G03.

Table 4. Statistical metrics of land surface temperatures (LST) retrieved using atmospheric parameters from different profile sources. The LST values calculated with SBPA parameters were considered as reference values.

		CFSv2	WRF G12	WRF G03	ACPC
LST [K]	R	0.99	0.99	0.99	0.99
	bias	0.23	0.32	0.36	−0.38
	MAE	0.54	0.79	0.81	0.56
	RMSE	0.55	0.79	0.82	0.56

Comparing these results with previous studies that evaluated the application of different atmospheric profiles for LST retrieval, Meng and Cheng (2018) [20] reported overall LST RMSE values higher than ours for eight different reanalysis profile sources analyzed around the globe. All their eight average RMSEs were larger than 1 K. The authors mention that ERA-Interim and MERRA (6 h product) showed the lowest RMSEs, at 1.09 K and 1.07 K respectively. They also indicated an average tendency to overestimate the LST, except for JRA-55. In Yang et al. (2020) [39], RMSEs were smaller than 0.6 K using profiles from ERA-Interim, MERRA2, NCEP GFS, and NCEP FNL, over Europe. Their worst accuracy (RMSE of 1 K) was obtained using MOD07 satellite-based profiles. Retrieving LST from three MODIS thermal bands, Pérez-Planells et al. (2015) [33] showed RMSEs between 0.6 and 0.9 K using ACPC/NCEP and between 1.3 and 3 K for MOD07 profiles, depending on the band and the altitude of the study sites in Spain.

Figure 8 displays the distribution of LST bias and RMSE among the case days. Figure 8a evidences the ACPC and WRF settings' average tendency to under and overestimate the LST, respectively. We found better RMSE values using CFSv2 in 11 of the 27 case days, and in 8 using ACPC. However, the metrics of mean errors are greater for WRF profiles, as in 11 case days the model improves the results of the reanalysis. Furthermore, the finer grid (G03) succeeded in downscaling the G12 11 times. In fact, the largest errors were achieved when using the WRF model (e.g., for case days 23, 19, and 17), contributing to the higher overall RMSE values. In general, the days with larger errors in atmospheric parameters (Figure 4) were the days with larger LST RMSEs, as in case day 23. Conversely, for case day 22, the errors in atmospheric parameters using ACPC were less than those using WRF profiles, but the highest LST RMSE on this day was with ACPC. Jiménez-Muñoz et al. (2010) [24] suggest that cases like this may be explained by compensation among the AC parameter errors, for instance, a significant positive difference in transmittance and significant but negative differences in the atmospheric radiances. Figure 9 shows how errors in the atmospheric parameters propagate to the retrieved LST. The sensitivity analysis of Sekertekin and Bonafoni (2020a) [74] reported that an uncertainty of ±0.01 in atmospheric transmittance had an impact of ±0.97 K on RTE-based LST retrieval. For upwelling and downwelling, uncertainties of ±10% led to ±1.82 K and ±0.07 K errors in LST, respectively. Rosas et al. (2017) [21] mentioned that an introduced uncertainty of 20% in the relative humidity profile could result in LST errors as large as 1.5 K in arid environments.

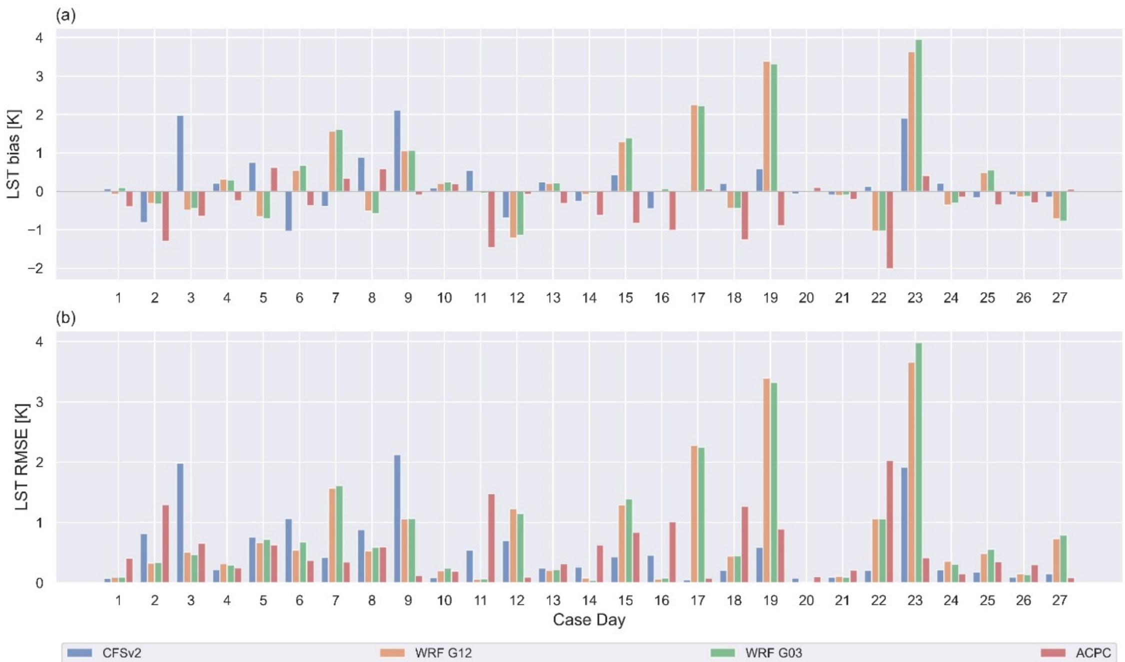

Figure 8. LST (**a**) bias and (**b**) RMSE for each case day.

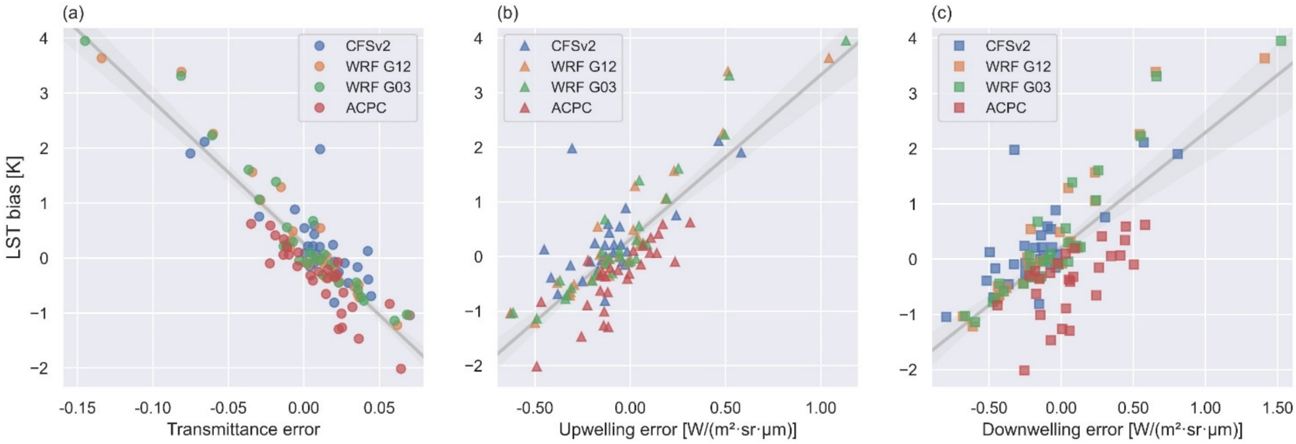

Figure 9. Relation of daily LST bias with errors in (**a**) transmittance, (**b**) upwelling, and (**c**) downwelling radiances for each case day. The gray line represents the linear regression for all data.

In summary, the attempt at downscaling the horizontal resolution of reanalysis data from 0.5° (~56 km) to 12 km and so to 3 km, aiming to reduce errors in the calculation of atmospheric parameters and hence in LST retrieval, did not perform as theoretically expected. Using WRF simulations, we improved the vertical resolution in the lowest atmospheric levels. However, no significant improvement was found in the AC using the WRF profiles. In some cases, using a finer grid resolution profile resulted in even greater differences in atmospheric parameters and LST estimation. Rosas et al. (2017) [21] reported that the higher vertical resolution of NCEP and ECMWF profiles in their study did not seem to play a significant role in the atmospheric correction. Even if data with higher resolution naturally tend to represent the atmospheric parameters better, it is not a strictly direct relationship [20,40]. Furthermore, the ACPC, which uses profiles with 1° × 1° (~111 km) horizontal resolution, showed good results. Although these profiles have a coarser horizontal resolution, previous studies have found satisfactory results using the ACPC, even surpassing other methods [24,31,46,93,113–117]. It is important to note that in this study the WRF profiles were extracted at 12 UTC to match the available radiosonde data. Nevertheless, the extraction could be set for the exact time of the satellite overpass. In the ACPC, and in general for reanalysis profiles, this time synchronization is achieved through linear interpolation, which may not be the most appropriate strategy for sampling weather fronts and diurnal heating cycles [20,27,29].

4. Conclusions

Vertical atmospheric profiles are key inputs in the atmospheric correction for estimating LST using the RTE inversion single-channel approach. This study evaluated the use of the WRF numerical model to simulate high-resolution profiles, improving horizontal, temporal, and vertical resolutions of NCEP CFSv2 reanalysis data. The profiles were incorporated into the MODTRAN RTM to compute the atmospheric correction parameters, which were then applied in the RTE to retrieve LST values from Landsat 8 TIRS10 data. We included in the comparison analysis the widely applied ACPC web-tool. The assessment took into account 27 clear-sky Landsat 8 scenes over a radiosonde station in Southern Brazil.

The obtained results showed that for the three atmospheric parameters (atmospheric transmittance, upwelling radiance, and downwelling radiance) the ACPC provided parameters in better agreement with those calculated using the radiosondes. The second-lowest uncertainties occurred when using CFSv2 profiles. No significant statistical differences were found between the parameters from the two WRF grids. None of the profile sources outperformed the others in all case days analyzed. The overall metrics of the WRF profiles were influenced by some cases with large errors. In general, the assessed profile sources better represented the atmosphere in dry and cold conditions. With respect to the retrieved LST values, using those calculated with the SBPA profile as reference, CFSv2 had the best results. With an RMSE of 0.55 K, it was slightly more accurate than ACPC (RMSE of 0.56 K). WRF G12 and G03 showed RMSE values of 0.79 and 0.82 K, respectively. Both WRF grids and CFSv2 generated a positive LST bias, while ACPC generated a negative bias. On balance, all the profile sources presented relatively good results in estimating the LST.

From the above findings, we conclude the following.

- Our main conclusion is that there is no special need to increase the horizontal resolution of reanalysis profiles aiming at general RTE-based LST retrieval. We recommend the use of NCEP CFSv2 profiles for these applications.
- The results reinforce the validity and feasibility of ACPC, which is free of charge.
- Even though the overall statistical metrics for WRF profiles were inferior, their results were satisfactory for the estimation of both atmospheric parameters and LST values.

Despite the fact that some studies used the WRF model to simulate the skin temperature [118,119], to the best of our knowledge, this paper is the first attempt to apply the WRF model to aid the atmospheric correction of thermal remote sensing data. Its use showed potential, and our findings encourage further validations. Our study adds to the background of studies combing TIR satellite images and high-resolution NWP models.

Finally, in spite of the discoveries in this study, some limitations to be considered in future work are worth mentioning. There were no in situ LST data available to perform validation of the retrieved LST. The uncertainties in the SBPA radiosonde profiles were not analyzed; they were directly assumed as reference data. The study results refer to one area only, and therefore additional research is currently ongoing to extrapolate the conclusions to other environments.

Author Contributions: Conceptualization, L.R.D., D.C.S. and S.B.A.R.; methodology, L.R.D., D.C.S., P.S.K. and S.B.A.R.; software, L.R.D., D.C.S., P.S.K. and S.T.L.d.C.; validation, L.R.D. and D.C.S.; investigation, L.R.D., D.C.S., P.S.K., N.S.d.R., S.T.L.d.C. and E.A.K.; resources, S.B.A.R.; data curation, L.R.D., D.C.S. and E.A.K.; writing—original draft preparation, L.R.D.; writing—review and editing, L.R.D., D.C.S., P.S.K., N.S.d.R. and S.B.A.R.; supervision, S.B.A.R.; project administration, S.B.A.R.; funding acquisition, S.B.A.R. All authors have read and agreed to the published version of the manuscript.

Funding: This study was financed in part by the Coordenação de Aperfeiçoamento de Pessoal de Nível Superior—Brazil (CAPES), finance code 001, grant number 88882.438973/2019-01.

Data Availability Statement: The Landsat 8 data are courtesy of the US Geological Survey Earth Resources Observation and Science Center. The CFSv2 reanalysis data are provided by the National Centers for Environmental Prediction (NCEP), available at the Research Data Archive (RDA)—National Center for Atmospheric Research (NCAR). The radiosonde observations were obtained from the University of Wyoming website.

Acknowledgments: The anonymous reviewers are thanked for their valuable contributions. We are also grateful to Luis Morales-Salinas (University of Chile) and Dražen Skokovic (University of Valencia) for their support regarding the MODTRAN model.

Conflicts of Interest: The authors declare no conflict of interest. The funders had no role in the design of the study, in the collection, analyses, or interpretation of data, in the writing of the manuscript, or in the decision to publish the results.

References

1. Cao, B.; Liu, Q.; Du, Y.; Roujean, J.L.; Gastellu-Etchegorry, J.P.; Trigo, I.F.; Zhan, W.; Yu, Y.; Cheng, J.; Jacob, F.; et al. A Review of Earth Surface Thermal Radiation Directionality Observing and Modeling: Historical Development, Current Status and Perspectives. *Remote Sens. Environ.* **2019**, *232*, 111304, https://doi.org/10.1016/j.rse.2019.111304.
2. WMO. *The Global Observing System for Climate: Implementation Needs*; World Meteorological Organization (WMO): Geneva, Switzerland, 2016; Volume 200.

3. Anderson, M.C.; Norman, J.M.; Kustas, W.P.; Houborg, R.; Starks, P.J.; Agam, N. A Thermal-Based Remote Sensing Technique for Routine Mapping of Land-Surface Carbon, Water and Energy Fluxes from Field to Regional Scales. *Remote Sens. Environ.* **2008**, *112*, 4227–4241, https://doi.org/10.1016/j.rse.2008.07.009.
4. Tardy, B.; Rivalland, V.; Huc, M.; Hagolle, O.; Marcq, S.; Boulet, G. A Software Tool for Atmospheric Correction and Surface Temperature Estimation of Landsat Infrared Thermal Data. *Remote Sens.* **2016**, *8*, 696, https://doi.org/10.3390/rs8090696.
5. Wu, P.; Yin, Z.; Zeng, C.; Duan, S.-B.; Gottsche, F.-M.; Li, X.; Ma, X.; Yang, H.; Shen, H. Spatially Continuous and High-Resolution Land Surface Temperature Product Generation: A Review of Reconstruction and Spatiotemporal Fusion Techniques. *IEEE Geosci. Remote Sens. Mag.* **2021**, *9*, 112–137, https://doi.org/10.1109/MGRS.2021.3050782.
6. Sobrino, J.A.; Del Frate, F.; Drusch, M.; Jiménez-Muñoz, J.C.; Manunta, P.; Regan, A. Review of Thermal Infrared Applications and Requirements for Future High-Resolution Sensors. *IEEE Trans. Geosci. Remote Sens.* **2016**, *54*, 2963–2972, https://doi.org/10.1109/TGRS.2015.2509179.
7. Montaner-Fernández, D.; Morales-Salinas, L.; Rodriguez, J.S.; Cárdenas-Jirón, L.; Huete, A.; Fuentes-Jaque, G.; Pérez-Martínez, W.; Cabezas, J. Spatio-Temporal Variation of the Urban Heat Island in Santiago, Chile during Summers 2005–2017. *Remote Sens.* **2020**, *12*, 3345, https://doi.org/10.3390/rs12203345.
8. Candy, B.; Saunders, R.W.; Ghent, D.; Bulgin, C.E. The Impact of Satellite-Derived Land Surface Temperatures on Numerical Weather Prediction Analyses and Forecasts. *J. Geophys. Res. Atmos.* **2017**, *122*, 9783–9802, https://doi.org/10.1002/2016JD026417.
9. Hu, X.; Ren, H.; Tansey, K.; Zheng, Y.; Ghent, D.; Liu, X.; Yan, L. Agricultural Drought Monitoring Using European Space Agency Sentinel 3A Land Surface Temperature and Normalized Difference Vegetation Index Imageries. *Agric. For. Meteorol.* **2019**, *279*, 107707, https://doi.org/10.1016/j.agrformet.2019.107707.
10. Jiménez-Muñoz, J.C.; Mattar, C.; Sobrino, J.A.; Malhi, Y. Digital Thermal Monitoring of the Amazon Forest: An Intercomparison of Satellite and Reanalysis Products. *Int. J. Digit. Earth* **2016**, *9*, 477–498, https://doi.org/10.1080/17538947.2015.1056559.
11. Magarreiro, C.; Gouveia, C.; Barroso, C.; Trigo, I. Modelling of Wine Production Using Land Surface Temperature and FAPAR—The Case of the Douro Wine Region. *Remote Sens.* **2019**, *11*, 604, https://doi.org/10.3390/rs11060604.
12. Pavlidou, E.; van der Meijde, M.; van der Werff, H.; Hecker, C. Time Series Analysis of Land Surface Temperatures in 20 Earthquake Casesworldwide. *Remote Sens.* **2019**, *11*, 61, https://doi.org/10.3390/rs11010061.
13. Gemitzi, A.; Dalampakis, P.; Falalakis, G. International Journal of Applied Earth Observations and Geoinformation Detecting Geothermal Anomalies Using Landsat 8 Thermal Infrared Remotely Sensed Data. *Int. J. Appl. Earth Obs. Geoinf.* **2021**, *96*, 102283, https://doi.org/10.1016/j.jag.2020.102283.
14. da Rocha, N.S.; Käfer, P.S.; Skokovic, D.; Veeck, G.; Diaz, L.R.; Kaiser, E.A.; Carvalho, C.M.; Cruz, R.C.; Sobrino, J.A.; Roberti, D.R.; et al. The Influence of Land Surface Temperature in Evapotranspiration Estimated by the S-SEBI Model. *Atmosphere* **2020**, *11*, 1059, https://doi.org/10.3390/atmos11101059.
15. Anderson, M.C.; Yang, Y.; Xue, J.; Knipper, K.R.; Yang, Y.; Gao, F.; Hain, C.R.; Kustas, W.P.; Cawse-Nicholson, K.; Hulley, G.; et al. Interoperability of ECOSTRESS and Landsat for Mapping Evapotranspiration Time Series at Sub-Field Scales. *Remote Sens. Environ.* **2021**, *252*, 112189, https://doi.org/10.1016/j.rse.2020.112189.
16. Maffei, C.; Alfieri, S.M.; Menenti, M. Relating Spatiotemporal Patterns of Forest Fires Burned Area and Duration to Diurnal Land Surface Temperature Anomalies. *Remote Sens.* **2018**, *10*, 1777, https://doi.org/10.3390/rs10111777.
17. Singh, N.; Chatterjee, R.S.; Kumar, D.; Panigrahi, D.C.; Mujawdiya, R. Retrieval of Precise Land Surface Temperature from ASTER Night-Time Thermal Infrared Data by Split Window Algorithm for Improved Coal Fire Detection in Jharia Coalfield, India. *Geocarto Int.* **2020**, 1–18, https://doi.org/10.1080/10106049.2020.1753820.
18. Anderson, M.C.; Allen, R.G.; Morse, A.; Kustas, W.P. Use of Landsat Thermal Imagery in Monitoring Evapotranspiration and Managing Water Resources. *Remote Sens. Environ.* **2012**, *122*, 50–65, https://doi.org/10.1016/j.rse.2011.08.025.
19. Tavares, M.H.; Cunha, A.H.F.; Motta-Marques, D.; Ruhoff, A.L.; Fragoso, C.R.; Munar, A.M.; Bonnet, M.P. Derivation of Consistent, Continuous Daily River Temperature Data Series by Combining Remote Sensing and Water Temperature Models. *Remote Sens. Environ.* **2020**, *241*, 111721, https://doi.org/10.1016/j.rse.2020.111721.
20. Meng, X.; Cheng, J. Evaluating Eight Global Reanalysis Products for Atmospheric Correction of Thermal Infrared Sensor—Application to Landsat 8 TIRS10 Data. *Remote Sens.* **2018**, *10*, 474, https://doi.org/10.3390/rs10030474.
21. Rosas, J.; Houborg, R.; McCabe, M.F. Sensitivity of Landsat 8 Surface Temperature Estimates to Atmospheric Profile Data: A Study Using MODTRAN in Dryland Irrigated Systems. *Remote Sens.* **2017**, *9*, 988, https://doi.org/10.3390/rs9100988.
22. Cristóbal, J.; Jiménez-Muñoz, J.; Prakash, A.; Mattar, C.; Skoković, D.; Sobrino, J. An Improved Single-Channel Method to Retrieve Land Surface Temperature from the Landsat-8 Thermal Band. *Remote Sens.* **2018**, *10*, 431, https://doi.org/10.3390/rs10030431.
23. Li, Z.-L.; Tang, B.-H.; Wu, H.; Ren, H.; Yan, G.; Wan, Z.; Trigo, I.F.; Sobrino, J.A. Satellite-Derived Land Surface Temperature: Current Status and Perspectives. *Remote Sens. Environ.* **2013**, *131*, 14–37, https://doi.org/10.1016/j.rse.2012.12.008.
24. Jiménez-Muñoz, J.C.; Sobrino, J.A.; Mattar, C.; Franch, B. Atmospheric Correction of Optical Imagery from MODIS and Reanalysis Atmospheric Products. *Remote Sens. Environ.* **2010**, *114*, 2195–2210, https://doi.org/10.1016/j.rse.2010.04.022.
25. Tang, H.; Li, Z.-L. *Quantitative Remote Sensing in Thermal Infrared*; Springer Remote Sensing/Photogrammetry; Springer Berlin Heidelberg: Berlin, Heidelberg, 2014; ISBN 978-3-642-42026-9.
26. Galve, J.M.; Sánchez, J.M.; Coll, C.; Villodre, J. A New Single-Band Pixel-by-Pixel Atmospheric Correction Method to Improve the Accuracy in Remote Sensing Estimates of LST. Application to Landsat 7-ETM+. *Remote Sens.* **2018**, *10*, 826, https://doi.org/10.3390/rs10060826.

27. Barsi, J.A.; Schott, J.R.; Palluconi, F.D.; Hook, S.J. Validation of a Web-Based Atmospheric Correction Tool for Single Thermal Band Instruments. In Proceedings of the Earth Observing Systems X.; Butler, J.J., Ed.; 18 August 2005; Volume 5882, p. 58820E.
28. Price, J.C. Estimating Surface Temperatures from Satellite Thermal Infrared Data—A Simple Formulation for the Atmospheric Effect. *Remote Sens. Environ.* **1983**, *13*, 353–361, https://doi.org/10.1016/0034-4257(83)90036-6.
29. Barsi, J.A.; Barker, J.L.; Schott, J.R. An Atmospheric Correction Parameter Calculator for a Single Thermal Band Earth-Sensing Instrument. In Proceedings of the IGARSS 2003, 2003 IEEE International Geoscience and Remote Sensing Symposium, Proceedings (IEEE Cat. No.03CH37477), IEEE, Toulouse, France, 21–25 July 2003; Volume 5, pp. 3014–3016.
30. Sobrino, J.A.; Jiménez-Muñoz, J.C.; Paolini, L. Land Surface Temperature Retrieval from LANDSAT TM 5. *Remote Sens. Environ.* **2004**, *90*, 434–440, https://doi.org/10.1016/j.rse.2004.02.003.
31. Sekertekin, A. Validation of Physical Radiative Transfer Equation-Based Land Surface Temperature Using Landsat 8 Satellite Imagery and SURFRAD in-Situ Measurements. *J. Atmos. Sol.-Terr. Phys.* **2019**, *196*, 105161, https://doi.org/10.1016/j.jastp.2019.105161.
32. Coll, C.; Caselles, V.; Valor, E.; Niclòs, R. Comparison between Different Sources of Atmospheric Profiles for Land Surface Temperature Retrieval from Single Channel Thermal Infrared Data. *Remote Sens. Environ.* **2012**, *117*, 199–210, https://doi.org/10.1016/j.rse.2011.09.018.
33. Pérez-Planells, L.; García-Santos, V.; Caselles, V. Comparing Different Profiles to Characterize the Atmosphere for Three MODIS TIR Bands. *Atmos. Res.* **2015**, *161–162*, 108–115, https://doi.org/10.1016/j.atmosres.2015.04.001.
34. Mira, M.; Olioso, A.; Rivalland, V.; Courault, D.; Marloie, O.; Guillevic, P. Quantifying Uncertainties in Land Surface Temperature Due to Atmospheric Correction: Application to Landsat-7 Data over a Mediterranean Agricultural Region. In Proceedings of the 2014 IEEE Geoscience and Remote Sensing Symposium, IEEE, Quebec City, QC, Canada, 13–18 July 2014; pp. 2375–2378.
35. Coll, C.; Caselles, V.; Galve, J.M.; Valor, E.; Niclòs, R.; Sánchez, J.M.; Rivas, R. Ground Measurements for the Validation of Land Surface Temperatures Derived from AATSR and MODIS Data. *Remote Sens. Environ.* **2005**, *97*, 288–300, https://doi.org/10.1016/j.rse.2005.05.007.
36. Mattar, C.; Durán-Alarcón, C.; Jiménez-Muñoz, J.C.; Santamaría-Artigas, A.; Olivera-Guerra, L.; Sobrino, J.A. Global Atmospheric Profiles from Reanalysis Information (GAPRI): A New Database for Earth Surface Temperature Retrieval. *Int. J. Remote Sens.* **2015**, *36*, 5045–5060, https://doi.org/10.1080/01431161.2015.1054965.
37. Duan, S.-B.; Li, Z.-L.; Wang, C.; Zhang, S.; Tang, B.-H.; Leng, P.; Gao, M.-F. Land-Surface Temperature Retrieval from Landsat 8 Single-Channel Thermal Infrared Data in Combination with NCEP Reanalysis Data and ASTER GED Product. *Int. J. Remote Sens.* **2018**, *40*, 1763–1778, https://doi.org/10.1080/01431161.2018.1460513.
38. Vanhellemont, Q. Automated Water Surface Temperature Retrieval from Landsat 8/TIRS. *Remote Sens. Environ.* **2020**, *237*, 111518, https://doi.org/10.1016/j.rse.2019.111518.
39. Malakar, N.K.; Hulley, G.C.; Hook, S.J.; Laraby, K.; Cook, M.; Schott, J.R. An Operational Land Surface Temperature Product for Landsat Thermal Data: Methodology and Validation. *IEEE Trans. Geosci. Remote Sens.* **2018**, *56*, 5717–5735, https://doi.org/10.1109/TGRS.2018.2824828.
40. Yang, J.; Duan, S.B.; Zhang, X.; Wu, P.; Huang, C.; Leng, P.; Gao, M. Evaluation of Seven Atmospheric Profiles from Reanalysis and Satellite-Derived Products: Implication for Single-Channel Land Surface Temperature Retrieval. *Remote Sens.* **2020**, *12*, 791, https://doi.org/10.3390/rs12050791.
41. Alghamdi, A.S. Evaluation of Four Reanalysis Datasets against Radiosonde over Southwest Asia. *Atmosphere* **2020**, *11*, 402, https://doi.org/10.3390/ATMOS11040402.
42. Berk, A.; Conforti, P.; Kennett, R.; Perkins, T.; Hawes, F.; van den Bosch, J. MODTRAN6: A Major Upgrade of the MODTRAN Radiative Transfer Code. In Proceedings of the Workshop on Hyperspectral Image and Signal Processing, Evolution in Remote Sensing; Velez-Reyes, M., Kruse, F.A., Eds.; 13 June 2014; Volume 2014, p. 90880H.
43. Kalnay, E.; Kanamitsu, M.; Kistler, R.; Collins, W.; Deaven, D.; Gandin, L.; Iredell, M.; Saha, S.; White, G.; Woollen, J.; et al. The NCEP/NCAR 40-Year Reanalysis Project. *Bull. Am. Meteorol. Soc.* **1996**, *77*, 437–471, https://doi.org/10.1175/1520-0477(1996)077<0437:TNYRP>2.0.CO;2.
44. National Centers for Environmental Prediction National Weather Service NOAA U.S. Department of Commerce NCEP FNL Operational Model Global Tropospheric Analyses, Continuing from July 1999 2000. https://doi.org/10.5065/D6M043C6.
45. Borbas, E.; Menzel, P. *MODIS Atmosphere L2 Atmosphere Profile Product*; NASA MODIS Adaptive Processing System, Goddard Space Flight Center: Greenbelt, MD, USA, 2017. http://dx.doi.org/10.5067/MODIS/MOD07_L2.006.
46. Skokovic, D.; Sobrino, J.A.; Jimenez-Munoz, J.C. Vicarious Calibration of the Landsat 7 Thermal Infrared Band and LST Algorithm Validation of the ETM+ Instrument Using Three Global Atmospheric Profiles. *IEEE Trans. Geosci. Remote Sens.* **2017**, *55*, 1804–1811, https://doi.org/10.1109/TGRS.2016.2633810.
47. Li, H.; Liu, Q.; Du, Y.; Jiang, J.; Wang, H. Evaluation of the NCEP and MODIS Atmospheric Products for Single Channel Land Surface Temperature Retrieval with Ground Measurements: A Case Study of HJ-1B IRS Data. *IEEE J. Sel. Top. Appl. Earth Obs. Remote Sens.* **2013**, *6*, 1399–1408, https://doi.org/10.1109/JSTARS.2013.2255118.
48. Aumann, H.H.; Chahine, M.T.; Gautier, C.; Goldberg, M.D.; Kalnay, E.; McMillin, L.M.; Revercomb, H.; Rosenkranz, P.W.; Smith, W.L.; Staelin, D.H.; et al. AIRS/AMSU/HSB on the Aqua Mission: Design, Science Objectives, Data Products, and Processing Systems. *IEEE Trans. Geosci. Remote Sens.* **2003**, *41*, 253–264, https://doi.org/10.1109/TGRS.2002.808356.

49. Dee, D.P.; Uppala, S.M.; Simmons, A.J.; Berrisford, P.; Poli, P.; Kobayashi, S.; Andrae, U.; Balmaseda, M.A.; Balsamo, G.; Bauer, P.; et al. The ERA-Interim Reanalysis: Configuration and Performance of the Data Assimilation System. *Q. J. R. Meteorol. Soc.* **2011**, *137*, 553–597, https://doi.org/10.1002/qj.828.
50. Rienecker, M.M.; Suarez, M.J.; Gelaro, R.; Todling, R.; Bacmeister, J.; Liu, E.; Bosilovich, M.G.; Schubert, S.D.; Takacs, L.; Kim, G.K.; et al. MERRA: NASA's Modern-Era Retrospective Analysis for Research and Applications. *J. Clim.* **2011**, *24*, 3624–3648, https://doi.org/10.1175/JCLI-D-11-00015.1.
51. Kanamitsu, M.; Ebisuzaki, W.; Woollen, J.; Yang, S.K.; Hnilo, J.J.; Fiorino, M.; Potter, G.L. NCEP-DOE AMIP-II Reanalysis (R-2). *Bull. Am. Meteorol. Soc.* **2002**, *83*, 1631–1644, https://doi.org/10.1175/BAMS-83-11-1631(2002)083<1631:NAR>2.3.CO;2.
52. Kobayashi, S.; Ota, Y.; Harada, Y.; Ebita, A.; Moriya, M.; Onoda, H.; Onogi, K.; Kamahori, H.; Kobayashi, C.; Endo, H.; et al. The JRA-55 Reanalysis: General Specifications and Basic Characteristics. *J. Meteorol. Soc. Japan. Ser. II* **2015**, *93*, 5–48, https://doi.org/10.2151/jmsj.2015-001.
53. Chen, B.; Liu, Z. Global Water Vapor Variability and Trend from the Latest 36 Year (1979 to 2014) Data of ECMWF and NCEP Reanalyses, Radiosonde, GPS, and Microwave Satellite. *J. Geophys. Res. Atmos.* **2016**, *121*, 11442–11462, https://doi.org/10.1002/2016JD024917.
54. Chen, G.; Iwasaki, T.; Qin, H.; Sha, W. Evaluation of the Warm-Season Diurnal Variability over East Asia in Recent Reanalyses JRA-55, ERA-Interim, NCEP CFSR, and NASA MERRA. *J. Clim.* **2014**, *27*, 5517–5537, https://doi.org/10.1175/JCLI-D-14-00005.1.
55. Tonooka, H. An Atmospheric Correction Algorithm for Thermal Infrared Multispectral Data over Land-a Water-Vapor Scaling Method. *IEEE Trans. Geosci. Remote Sens.* **2001**, *39*, 682–692, https://doi.org/10.1109/36.911125.
56. Wee, T.K.; Kuo, Y.H.; Lee, D. kyou; Liu, Z.; Wang, W.; Chen, S.Y. Two Overlooked Biases of the Advanced Research Wrf (Arw) Model in Geopotential Height and Temperature. *Mon. Weather Rev.* **2012**, *140*, 3907–3918, https://doi.org/10.1175/MWR-D-12-00045.1.
57. Hassanli, H.; Rahimzadegan, M. Investigating Extracted Total Precipitable Water Vapor from Weather Research and Forecasting (WRF) Model and MODIS Measurements. *J. Atmos. Sol. -Terr. Phys.* **2019**, *193*, 105060, https://doi.org/10.1016/j.jastp.2019.105060.
58. Lee, H.; Won, J.S.; Park, W. An Atmospheric Correction Using High Resolution Numericalweather Prediction Models for Satellite-Borne Single-Channel Mid-Wavelength and Thermal Infrared Imaging Sensors. *Remote Sens.* **2020**, *12*, 853, https://doi.org/10.3390/rs12050853.
59. Skamarock, W.C.; Klemp, J.B.; Dudhia, J.; Gill, D.O.; Zhiquan, L.; Berner, J.; Wang, W.; Powers, J.G.; Duda, M.G.; Barker, D.M.; et al. *A Description of the Advanced Research WRF Model Version 4*; National Center for Atmospheric Research: Boulder, CO, USA, 2019.
60. Powers, J.G.; Klemp, J.B.; Skamarock, W.C.; Davis, C.A.; Dudhia, J.; Gill, D.O.; Coen, J.L.; Gochis, D.J.; Ahmadov, R.; Peckham, S.E.; et al. The Weather Research and Forecasting Model: Overview, System Efforts, and Future Directions. *Bull. Am. Meteorol. Soc.* **2017**, *98*, 1717–1737, https://doi.org/10.1175/BAMS-D-15-00308.1.
61. Onwukwe, C.; Jackson, P.L. Meteorological Downscaling with Wrf Model, Version 4.0, and Comparative Evaluation of Planetary Boundary Layer Schemes over a Complex Coastal Airshed. *J. Appl. Meteorol. Climatol.* **2020**, *59*, 1295–1319, https://doi.org/10.1175/JAMC-D-19-0212.1.
62. Kioutsioukis, I.; de Meij, A.; Jakobs, H.; Katragkou, E.; Vinuesa, J.; Kazantzidis, A. High Resolution WRF Ensemble Forecasting for Irrigation: Multi-Variable Evaluation. *Atmos. Res.* **2016**, *167*, 156–174, https://doi.org/10.1016/j.atmosres.2015.07.015.
63. Moya-Álvarez, A.S.; Estevan, R.; Kumar, S.; Flores Rojas, J.L.; Ticse, J.J.; Martínez-Castro, D.; Silva, Y. Influence of PBL Parameterization Schemes in WRF_ARW Model on Short-Range Precipitation's Forecasts in the Complex Orography of Peruvian Central Andes. *Atmos. Res.* **2020**, *233*, 104708, https://doi.org/10.1016/j.atmosres.2019.104708.
64. Fekih, A.; Mohamed, A. Evaluation of the WRF Model on Simulating the Vertical Structure and Diurnal Cycle of the Atmospheric Boundary Layer over Bordj Badji Mokhtar (Southwestern Algeria). *J. King Saud Univ.-Sci.* **2019**, *31*, 602–611, https://doi.org/10.1016/j.jksus.2017.12.004.
65. Mylonas, M.P.; Douvis, K.C.; Polychroni, I.D.; Politi, N.; Nastos, P.T. Analysis of a Mediterranean Tropical-Like Cyclone. Sensitivity to WRF Parameterizations and Horizontal Resolution. *Atmosphere* **2019**, *10*, 425, https://doi.org/10.3390/atmos10080425.
66. Tyagi, B.; Magliulo, V.; Finardi, S.; Gasbarra, D.; Carlucci, P.; Toscano, P.; Zaldei, A.; Riccio, A.; Calori, G.; D'Allura, A.; et al. Performance Analysis of Planetary Boundary Layer Parameterization Schemes in WRF Modeling Set up over Southern Italy. *Atmosphere* **2018**, *9*, 272, https://doi.org/10.3390/atmos9070272.
67. Hersbach, H.; Bell, B.; Berrisford, P.; Hirahara, S.; Horányi, A.; Muñoz-Sabater, J.; Nicolas, J.; Peubey, C.; Radu, R.; Schepers, D.; et al. The ERA5 Global Reanalysis. *Q. J. R. Meteorol. Soc.* **2020**, *146*, 1999–2046, https://doi.org/10.1002/qj.3803.
68. Saha, S.; Moorthi, S.; Wu, X.; Wang, J.; Nadiga, S.; Tripp, P.; Behringer, D.; Hou, Y.-T.; Chuang, H.; Iredell, M.; et al. The NCEP Climate Forecast System Version 2. *J. Clim.* **2014**, *27*, 2185–2208, https://doi.org/10.1175/JCLI-D-12-00823.1.
69. Vanhellemont, Q. Combined Land Surface Emissivity and Temperature Estimation from Landsat 8 OLI and TIRS. *ISPRS J. Photogramm. Remote Sens.* **2020**, *166*, 390–402, https://doi.org/10.1016/j.isprsjprs.2020.06.007.
70. Porto Alegre City Hall. *Neighborhood Law No. 12.112/16*; Porto Alegre Official Gazette: Porto Alegre, Brazil, 2016; p. 37.
71. Alvares, C.A.; Stape, J.L.; Sentelhas, P.C.; De Moraes Gonçalves, J.L.; Sparovek, G. Köppen's Climate Classification Map for Brazil. *Meteorol. Z.* **2013**, *22*, 711–728, https://doi.org/10.1127/0941-2948/2013/0507.
72. Matzenauer, R.; Radin, B.; Almeida, I.R. de *Atlas Climático Do Rio Grande Do Sul*; CemetRS: Porto Alegre, Brazil, 2011.

73. Roy, D.P.; Wulder, M.A.; Loveland, T.R.; C.E., W.; Allen, R.G.; Anderson, M.C.; Helder, D.; Irons, J.R.; Johnson, D.M.; Kennedy, R.; et al. Landsat-8: Science and Product Vision for Terrestrial Global Change Research. *Remote Sens. Environ.* **2014**, *145*, 154–172, https://doi.org/10.1016/j.rse.2014.02.001.
74. Sekertekin, A.; Bonafoni, S. Land Surface Temperature Retrieval from Landsat 5, 7, and 8 over Rural Areas: Assessment of Different Retrieval Algorithms and Emissivity Models and Toolbox Implementation. *Remote Sens.* **2020**, *12*, 294, https://doi.org/10.3390/rs12020294.
75. Wang, W.; Bruyere, C.; Michael, D.; Duhia, J.; Dave, G.; Kavulich, M.; Werner, K.; Chen, M.; Hui-Chuan, L.; Michalakes, J.; et al. *Advanced Research WRF (ARW) Version 4 Modeling System User´s Guide*; National Center for Atmospheric Research: Boulder, CO, USA, 2019; Volume 456.
76. Xie, B.; Fung, J.C.H.; Chan, A.; Lau, A. Evaluation of Nonlocal and Local Planetary Boundary Layer Schemes in the WRF Model. *J. Geophys. Res. Atmos.* **2012**, *117*, https://doi.org/10.1029/2011JD017080.
77. Stensrud, D.J. *Parameterization Schemes*; Cambridge University Press: Cambridge, UK, 2007; Volume 9780521865; ISBN 9780511812590.
78. García-Díez, M.; Fernández, J.; Fita, L.; Yagüe, C. Seasonal Dependence of WRF Model Biases and Sensitivity to PBL Schemes over Europe. *Q. J. R. Meteorol. Soc.* **2013**, *139*, 501–514, https://doi.org/10.1002/qj.1976.
79. Chen, S.-H.; Sun, W.-Y. A One-Dimensional Time Dependent Cloud Model. *J. Meteorol. Soc. Japan Ser. II* **2002**, *80*, 99–118, https://doi.org/10.2151/jmsj.80.99.
80. Hong, S.-Y.; Noh, Y.; Dudhia, J. A New Vertical Diffusion Package with an Explicit Treatment of Entrainment Processes. *Mon. Weather Rev.* **2006**, *134*, 2318–2341, https://doi.org/10.1175/MWR3199.1.
81. Janjić, Z.I. The Step-Mountain Eta Coordinate Model: Further Developments of the Convection, Viscous Sublayer, and Turbulence Closure Schemes. *Mon. Weather Rev.* **1994**, *122*, 927–945, https://doi.org/10.1175/1520-0493(1994)122<0927:TSMECM>2.0.CO;2.
82. Dudhia, J. Numerical Study of Convection Observed during the Winter Monsoon Experiment Using a Mesoscale Two-Dimensional Model. *J. Atmos. Sci.* **1989**, *46*, 3077–3107, https://doi.org/10.1175/1520-0469(1989)046<3077:NSOCOD>2.0.CO;2.
83. Mlawer, E.J.; Taubman, S.J.; Brown, P.D.; Iacono, M.J.; Clough, S.A. Radiative Transfer for Inhomogeneous Atmospheres: RRTM, a Validated Correlated-k Model for the Longwave. *J. Geophys. Res. Atmos.* **1997**, *102*, 16663–16682, https://doi.org/10.1029/97JD00237.
84. Tewari, M.; Chen, F.; Wang, W.; Dudhia, J.; LeMone, M.A.; Mitchell, K.; Ek, M.; Gayno, G.; Wegiel, J.; Cuenca, R.H. Implementation and Verification of the Unified Noah Land Surface Model in the WRF Model. *Bull. Am. Meteorol. Soc.* **2004**, 2165–2170, https://doi.org/10.1007/s11269-013-0452-7.
85. Jiménez, P.A.; Dudhia, J.; González-Rouco, J.F.; Navarro, J.; Montávez, J.P.; García-Bustamante, E. A Revised Scheme for the WRF Surface Layer Formulation. *Mon. Weather Rev.* **2012**, *140*, 898–918, https://doi.org/10.1175/MWR-D-11-00056.1.
86. Diaz, L.R.; Santos, D.C.; Käfer, P.S.; Iglesias, M.L.; da Rocha, N.S.; da Costa, S.T.L.; Kaiser, E.A.; Rolim, S.B.A. Reanalysis Profile Downscaling with WRF Model and Sensitivity to PBL Parameterization Schemes over a Subtropical Station. *J. Atmos. Sol.-Terr. Phys.* **2021**, *222*, 105724, https://doi.org/10.1016/j.jastp.2021.105724.
87. Santos, D.C.; Nascimento, E.D.L. Numerical Simulations of the South American Low Level Jet in Two Episodes of MCSs: Sensitivity to PBL and Convective Parameterization Schemes. *Adv. Meteorol.* **2016**, *2016*, https://doi.org/10.1155/2016/2812978.
88. Diaz, L.R.; Santos, D.C.; Käfer, P.S.; da Rocha, N.S.; da Costa, S.T.L.; Kaiser, E.A.; Rolim, S.B.A. Atmospheric Correction of Thermal Infrared Landsat Images Using High-Resolution Vertical Profiles Simulated by WRF Model. *Environ. Sci. Proc.* **2021**, *8*, 27, https://doi.org/10.3390/ecas2021-10351.
89. Sobrino, J.; Raissouni, N.; Li, Z.-L. A Comparative Study of Land Surface Emissivity Retrieval from NOAA Data. *Remote Sens. Environ.* **2001**, *75*, 256–266, https://doi.org/10.1016/S0034-4257(00)00171-1.
90. Li, Z.L.; Wu, H.; Wang, N.; Qiu, S.; Sobrino, J.A.; Wan, Z.; Tang, B.H.; Yan, G. Land Surface Emissivity Retrieval from Satellite Data. *Int. J. Remote Sens.* **2013**, *34*, 3084–3127, https://doi.org/10.1080/01431161.2012.716540.
91. Sobrino, J.A.; Jimenez-Munoz, J.C.; Soria, G.; Romaguera, M.; Guanter, L.; Moreno, J.; Plaza, A.; Martinez, P. Land Surface Emissivity Retrieval from Different VNIR and TIR Sensors. *IEEE Trans. Geosci. Remote Sens.* **2008**, *46*, 316–327, https://doi.org/10.1109/TGRS.2007.904834.
92. Van de Griend, A.A.; Owe, M. On the Relationship between Thermal Emissivity and the Normalized Difference Vegetation Index for Natural Surfaces. *Int. J. Remote Sens.* **1993**, *14*, 1119–1131, https://doi.org/10.1080/01431169308904400.
93. Yu, X.; Guo, X.; Wu, Z. Land Surface Temperature Retrieval from Landsat 8 TIRS—Comparison between Radiative Transfer Equation-Based Method, Split Window Algorithm and Single Channel Method. *Remote Sens.* **2014**, *6*, 9829–9852, https://doi.org/10.3390/rs6109829.
94. Li, S.; Jiang, G.-M. Land Surface Temperature Retrieval From Landsat-8 Data With the Generalized Split-Window Algorithm. *IEEE Access* **2018**, *6*, 18149–18162, https://doi.org/10.1109/ACCESS.2018.2818741.
95. Valor, E.; Caselles, V. Mapping Land Surface Emissivity from NDVI: Application to European, African, and South American Areas. *Remote Sens. Environ.* **1996**, *57*, 167–184, https://doi.org/10.1016/0034-4257(96)00039-9.
96. Käfer, P.S.P.S.; Rolim, S.B.A.; Iglesias, M.L.; da Rocha, N.S.; Diaz, L.R. Land Surface Temperature Retrieval by LANDSAT 8 Thermal Band: Applications of Laboratory and Field Measurements. *IEEE J. Sel. Top. Appl. Earth Obs. Remote Sens.* **2019**, *12*, 2332–2341, https://doi.org/10.1109/JSTARS.2019.2913822.

97. Sekertekin, A.; Bonafoni, S. Sensitivity Analysis and Validation of Daytime and Nighttime Land Surface Temperature Retrievals from Landsat 8 Using Different Algorithms and Emissivity Models. *Remote Sens.* **2020**, *12*, 2776, https://doi.org/10.3390/RS12172776.
98. Oltra-Carrió, R.; Sobrino, J.A.; Franch, B.; Nerry, F. Land Surface Emissivity Retrieval from Airborne Sensor over Urban Areas. *Remote Sens. Environ.* **2012**, *123*, 298–305, https://doi.org/10.1016/j.rse.2012.03.007.
99. Harod, R.; Eswar, R.; Bhattacharya, B.K. Effect of Surface Emissivity and Retrieval Algorithms on the Accuracy of Land Surface Temperature Retrieved from Landsat Data. *Remote Sens. Lett.* **2021**, *12*, 983–993, https://doi.org/10.1080/2150704X.2021.1957511.
100. Ihlen, V.; Zanter, K. *Landsat 8 (L8) Data Users Handbook*; Sioux Falls, SD, USA, 2019; Volume 5.
101. Jiménez-Muñoz, J.C.; Cristobal, J.; Sobrino, J.A.J.A.; Sòria, G.; Ninyerola, M.; Pons, X.; Jimenez-Munoz, J.C.; Cristobal, J.; Sobrino, J.A.J.A.; Soria, G.; et al. Revision of the Single-Channel Algorithm for Land Surface Temperature Retrieval from Landsat Thermal-Infrared Data. *IEEE Trans. Geosci. Remote Sens.* **2009**, *47*, 339–349, https://doi.org/10.1109/TGRS.2008.2007125.
102. Carlson, T.N.; Ripley, D.A. On the Relation between NDVI, Fractional Vegetation Cover, and Leaf Area Index. *Remote Sens. Environ.* **1997**, *62*, 241–252, https://doi.org/10.1016/S0034-4257(97)00104-1.
103. Sobrino, J.A.; Raissouni, N. Toward Remote Sensing Methods for Land Cover Dynamic Monitoring: Application to Morocco. *Int. J. Remote Sens.* **2000**, *21*, 353–366, https://doi.org/10.1080/014311600210876.
104. Berk, A.; Anderson, G.P.; Acharya, P.K.; Hoke, M.L.; Chetwynd, J.H.; Bernstein, L.S.; Shettle, E.P.; Matthew, M.W.; Adler-Golden, S.M. *MODTRAN4 Version 3 Revision 1 USER'S MANUAL.*; Air Force Research Laboratory: Hanscom AFB, MA, USA, 2003.
105. Atmospheric Correction Parameter Calculator. Mid-Latitude Summer Standard Profile. Available online: https://atmcorr.gsfc.nasa.gov/RSD/mid_lat_summer_stdatm_RH_units.rsd (accessed on 16 December 2020).
106. Atmospheric Correction Parameter Calculator. Mid-Latitude Winter Standard Profile. Available online: https://atmcorr.gsfc.nasa.gov/RSD/mid_lat_winter_stdatm_units.rsd (accessed on 16 December 2020).
107. Chai, T.; Draxler, R.R. Root Mean Square Error (RMSE) or Mean Absolute Error (MAE)?–Arguments against Avoiding RMSE in the Literature. *Geosci. Model Dev.* **2014**, *7*, 1247–1250, https://doi.org/10.5194/gmd-7-1247-2014.
108. Willmott, C.J.; Matsuura, K. Advantages of the Mean Absolute Error (MAE) over the Root Mean Square Error (RMSE) in Assessing Average Model Performance. *Clim. Res.* **2005**, *30*, 79–82, https://doi.org/10.3354/cr030079.
109. Taylor, K.E. Summarizing Multiple Aspects of Model Performance in a Single Diagram. *J. Geophys. Res. Atmos.* **2001**, *106*, 7183–7192, https://doi.org/10.1029/2000JD900719.
110. Pérez-Jordán, G.; Castro-Almazán, J.A.; Muñoz-Tuñón, C.; Codina, B.; Vernin, J. Forecasting the Precipitable Water Vapour Content: Validation for Astronomical Observatories Using Radiosoundings. *Mon. Not. R. Astron. Soc.* **2015**, *452*, 1992–2003, https://doi.org/10.1093/mnras/stv1394.
111. Lin, C.; Chen, D.; Yang, K.; Ou, T. Impact of Model Resolution on Simulating the Water Vapor Transport through the Central Himalayas: Implication for Models' Wet Bias over the Tibetan Plateau. *Clim. Dyn.* **2018**, *51*, 3195–3207, https://doi.org/10.1007/s00382-018-4074-x.
112. Mohan, M.; Sati, A.P. WRF Model Performance Analysis for a Suite of Simulation Design. *Atmos. Res.* **2016**, *169*, 280–291, https://doi.org/10.1016/j.atmosres.2015.10.013.
113. Tavares, M.H.; Cunha, A.H.F.; Motta-Marques, D.; Ruhoff, A.L.; Cavalcanti, J.R.; Fragoso, C.R.; Bravo, J.M.; Munar, A.M.; Fan, F.M.; Rodrigues, L.H.R. Comparison of Methods to Estimate Lake-Surface-Water Temperature Using Landsat 7 ETM+ and MODIS Imagery: Case Study of a Large Shallow Subtropical Lake in Southern Brazil. *Water* **2019**, *11*, 168, https://doi.org/10.3390/w11010168.
114. Coll, C.; Galve, J.M.; Sanchez, J.M.; Caselles, V. Validation of Landsat-7/ETM+ Thermal-Band Calibration and Atmospheric Correction with Ground-Based Measurements. *IEEE Trans. Geosci. Remote Sens.* **2010**, *48*, 547–555, https://doi.org/10.1109/TGRS.2009.2024934.
115. García-Santos, V.; Cuxart, J.; Martínez-Villagrasa, D.; Jiménez, M.A.; Simó, G. Comparison of Three Methods for Estimating Land Surface Temperature from Landsat 8-TIRS Sensor Data. *Remote Sens.* **2018**, *10*, 1450, https://doi.org/10.3390/rs10091450.
116. Windahl, E.; de Beurs, K. An Intercomparison of Landsat Land Surface Temperature Retrieval Methods under Variable Atmospheric Conditions Using in Situ Skin Temperature. *Int. J. Appl. Earth Obs. Geoinf.* **2016**, *51*, 11–27, https://doi.org/10.1016/j.jag.2016.04.003.
117. Käfer, P.S.; Rolim, S.B.A.; Diaz, L.R.; da Rocha, N.S.; Iglesias, M.L.; Rex, F.E. Comparative analysis of split-window and single-channel algorithms for land surface temperature retrieval of a pseudo-invariant target. *Bull. Geod. Sci.* **2020**, *26*, https://doi.org/10.1590/s1982-21702020000200008.
118. Wang, D.; Liu, Y.; Yu, T.; Zhang, Y.; Liu, Q.; Chen, X.; Zhan, Y. A Method of Using WRF-Simulated Surface Temperature to Estimate Daily Evapotranspiration. *J. Appl. Meteorol. Climatol.* **2020**, *59*, 901–914, https://doi.org/10.1175/JAMC-D-19-0287.1.
119. Wang, D.; Yu, T.; Liu, Y.; Gu, X.; Mi, X.; Shi, S.; Ma, M.; Chen, X.; Zhang, Y.; Liu, Q.; et al. Estimating Daily Actual Evapotranspiration at a Landsat-like Scale Utilizing Simulated and Remote Sensing Surface Temperature. *Remote Sens.* **2021**, *13*, 225, https://doi.org/10.3390/rs13020225.

.

6.2 ARTIGO 02: Evaluating Land Surface Temperature (LST) retrieval methods and the on-demand Surface Temperature (ST) product derived from Landsat 8 TIRS data

O "*Evaluating Land Surface Temperature (LST) retrieval methods and the on-demand Surface Temperature (ST) product derived from Landsat 8 TIRS data*" foi submetido ao *Journal of Applied Remote Sensing* (JARS). Neste artigo, investigou-se qual o erro produzido na LST a partir do uso dos algoritmos de canal único GSC, ISC e do produto ST. A ferramenta ACPC da NASA foi utilizada como fonte dos dados atmosféricos com base nos achados do primeiro artigo. Os resultados deste segundo artigo mostraram qual o método mais adequado para estimar a LST com o menor erro. A importância de avaliar algoritmos de canal único parte de dois fatores: (i) dada a aplicação desses algoritmos na estimativa da LST a partir de dados do infravermelho termal medidos em uma banda, possibilitando estudos com séries temporais da série Landsat (1982 a 2022); (ii) dada situações de mau funcionamento de canais espectrais, como o ocorrido no Landsat 8 que limitou o uso de apenas uma banda.

Gmail **Savannah Lemos <savannahlemos95@gmail.com>**

JARS 220340G Confirmation of Manuscript Submission

1 mensagem

jars@spie.org <jars@spie.org> 10 de junho de 2022 às 17:32
Responder a: jars@spie.org
Para: savannahlemos95@gmail.com
Cc: silvia.rolim@ufrgs.br, l.ribeiro.diaz@vu.nl, pamela.kafer@ufrgs.br, eduardo.kaiser@ufrgs.br, gabrielhallal@gmail.com, najila.rocha@ufrgs.br, savannah.lemos@ufrgs.br

Journal of
Applied Remote Sensing SPIE.

Dear Ms. Lemos da Costa,

I acknowledge receipt of your manuscript entitled "Evaluating Land Surface Temperature (LST) retrieval methods and the on-demand Surface Temperature (ST) product derived from Landsat 8 TIRS data," which you have submitted to be considered for publication in the Journal of Applied Remote Sensing (JARS).

The authors listed on this manuscript are:

Savannah Lemos da Costa
Silvia Rolim
Lucas Diaz
Pâmela Käfer
Eduardo Kaiser
Gabriel Hallal
Najila da Rocha

All authors named on a manuscript are expected to have made a significant contribution to the writing, concept, design, execution, or interpretation of the work represented. If you feel you are incorrectly included as an author on this manuscript, please respond immediately to this message indicating your concerns.

The manuscript control number for your paper is JARS 220340G. Please refer to this number in any correspondence.

You may check on the status of this manuscript at any time by selecting the "Check Manuscript Status" link after logging in at the following URL:

https://jars.msubmit.net/cgi-bin/main.plex

If you have any questions about your submission, please contact the editorial staff using the "Send Manuscript Correspondence" link, or send an e-mail to journals@spie.org.

If you receive a suspicious email purporting to be from this journal and you question its authenticity, please contact us immediately at jars@spie.org.

Note to all authors: Please be sure to update your areas of expertise and contact information in your Journal of Applied Remote Sensing profile at https://jars.msubmit.net/cgi-bin/main.plex. If you are unsure of your login name or password, use the "Unknown/Forgotten Password" link. Once logged on, you can modify your account information via the "Modify Profile/Password" link at the bottom of your homepage.

Thank you for submitting your work to the Journal of Applied Remote Sensing.

Sincerely,

Dr. Ni-Bin Chang
Editor-in-Chief
Journal of Applied Remote Sensing

Evaluating Land Surface Temperature (LST) retrieval methods and the on-demand Surface Temperature (ST) product derived from Landsat 8 TIRS data

Savannah Tâmara Lemos da Costa[a*], Silvia Beatriz Alves Rolim[a], Lucas Ribeiro Diaz[b], Pâmela Suélen Käfer[a], Eduardo André Kaiser[a], Gabriel Prattes Hallal[a], Nájila Souza da Rocha[a]

[a]Federal University of Rio Grande do Sul (UFRGS), State Research Center for Remote Sensing and Meteorology (CEPSRM), Geological Remote Sensing Laboratory (LabSRGeo), Porto Alegre (RS), Brazil.

[b]Faculty of Science, Vrije Universiteit Amsterdam, 1081 HV Amsterdam, The Netherlands

Abstract. Several methods have been developed for Land Surface Temperature (LST) retrieval based on satellite data, such as Radiative Transfer Equation (RTE), and algorithms as the Single Channel (SC), Mono Window (MW), and Split Window (SW). These efforts have been made in an attempt to minimize the errors imposed in the nonlinear solution of the Radiative Transfer in the land-atmosphere interface. Most methods are developed for the North Hemisphere and its distinct atmospheric and surface conditions. In addition, Single Channel methods allow retrieving LST of thermal data from almost 40 years of the Landsat Program, since 1984. Here we compared LSTs obtained with Generalized Single Channel (GSC) and Improved Single Channel (ISC) algorithms, and on-demand Surface Temperature (ST) products of a Landsat-8 image. The derived temperatures were validated with a local radiosonde and auxiliary data at a pseudo-invariant sand dune target (99.53% of quartz) during the Brazilian summer season. The LST products showed a high correlation (r=0.99) with LST data from the field experiment, resulting in a better performance for ISC (RMSE of 0.69 K), followed by GSC (RMSE of 2.5 K) and ST product (RMSE of 4.24 K). These results complement and reinforce the research developed in the area.

Keywords: thermal infrared, radiative transfer, single-channel, emissivity, atmospheric correction.

*****Savannah Tâmara Lemos da Costa**,** E-mail: savannahlemos95@gmail.com

1 Introduction

Several methods have been developed for Land Surface Temperature (LST) retrieval based on satellite data, such as Radiative Transfer Equation (RTE)[1–5], and algorithms as the Single Channel (SC)[6–10], Mono Window (MW)[11], and Split Window (SW)[12–14]. These efforts have been made in an attempt to minimize the errors imposed in the nonlinear solution of the Radiative Transfer in the land-atmosphere interface.

A well-established way to obtain an accurate LST is inverting and solving the RTE using atmospheric parameters (transmittance, upwelling and downwelling atmospheric radiances) derived from a radiosonde vertical profile[7,9,15]. These parameters can be estimated through a Radiative Transfer Model (RTM) such as the MODerate resolution atmospheric TRANsmission

(MODTRAN)[4,16,17]. However, radiosonde launch is not common and moreover, relies on a field campaign that spends resources and must be made at the same satellite overpass time.

Reference 18 and 19 proposed a free web tool as an alternative way to estimate the atmospheric parameters, the Atmospheric Correction Parameter Calculator (ACPC). It can automatically generate atmospheric correction parameters based on the National Centers for Environmental Prediction (NCEP) reanalysis data[20] through the MODTRAN[4,5,17,21,22]. Many studies reported acceptable accuracy in the LST retrieval using ACPC data[3,18,19,23–26].

In order to reduce atmospheric parameters dependence in the LST estimation procedure, other methods based on RTE approximations have been proposed, such as the Generalized Single Channel (GSC)[1,8–10] and the Improved Single Channel (ISC)[6,7] algorithms. The GSC uses only the water vapor content to correct the atmospheric effects. Many authors reported LST errors around 2.7 K and 4 K in Landsat 8 data experiments using the GSC[8,9,15,27]. On the other hand, the ISC retrieves the LST by using the water vapor and including the mean atmospheric temperature. It was proposed for GSC improvement and has been successful as some studies reported errors between 0.27 K to 1.6 K for ISC application in Landsat 8 data[7,28–30].

Recently, Surface Temperature (ST) products from Landsat 5, 7, and 8 became available[31–33]. They can generate a valuable long-term series of LST with moderate spatial resolution (100 to 120 m) for almost 40 years. Some studies have been conducted on the validation of the ST product over North America and showed RMSE between 0.6 and 1.1 K over water bodies, and between 2.1 and 3K over land surfaces[4,33,34].

Most of the SC methods are idealized and developed for the North Hemisphere which has its distinct atmospheric and surface characteristics. In this sense, it is important to evaluate these methods and on-demand ST products of a Landsat-8 image for LST retrieval in the tropical to temperate climate of the Southern Hemisphere.

The main objective is to compare LSTs obtained with Generalized Single Channel (GSC) and Improved Single Channel (ISC) algorithms, and on-demand Surface Temperature (ST) products of a Landsat-8 image. According to the CEOS Land Product Validation subgroup and the International Land Surface Temperature and Emissivity Working Group, estimated LST through satellite thermal data must be limited to up to 1 K of uncertainty to be useful in climate studies[35]. For Ref. 36 and 37, an adequate LST precision ranges from less than 2 K for energy fluxes to less than 0.3 K for climate change detection. In the Southern Hemisphere context, the derived temperatures were validated with a local radiosonde and auxiliary data at a pseudo-invariant sand dune target (99.53% of quartz) during the Brazilian summer season.

2 Theoretical background

Thermal Infrared (TIR) data measured by satellite sensors are directly associated with LST through RTE. However, this equation is mathematically undetermined once the number of variables to solve for (one temperature and n emissivities) is always greater than the number of observations available (n)[33]. Moreover, atmospheric effects must be corrected on at-sensor radiance[6–10,28,38]. Therefore, several methods such as Single Channel, Mono Window, and Split Window have been proposed for LST retrieval based on assumptions and constraints on RTE and emissivity [2,6–14,20,28,36,39,40].

Single Channel (SC) methods retrieve LST using the radiance measured in a single band from the sensor and assuming the previous knowledge of emissivity[36,39]. Inverting and solving the RTE is the best option for LST retrieval, since it does not involve additional approximations[3,5,10,33,41]. However, accurate atmospheric correction parameters are necessary.

They can be calculated through an RTM as the MODTRAN using a radiosonde atmospheric vertical profile as initial input[4,7,9,15–17]. Since radiosonde launch is a difficult task, atmospheric profiles from reanalysis data can be alternatively used[4,5,17,21,22].

Generalized Single Channel (GSC)[1,8–10] and the Improved Single Channel (ISC)[6,7] algorithms aimed to reduce the dependence on radiosonde data and atmospheric parameters. The GSC proposed the LST retrieval for any thermal sensor with a Full-Width Half-Maximum (FWHM) of around 1 µm using only the water vapor content to correct the atmospheric effects[1]. However, this restriction to a unique atmospheric variable for representation of the real state of the atmosphere produced LST errors for water vapor content higher than 3 $g.cm^{-2}$ [9,28]. Therefore, the ISC aimed for the GSC enhancement. It allows the LST retrieval by employing the water vapor content and the mean atmospheric temperature[6].

LST is an essential parameter for understanding the spatiotemporal distribution of the energy fluxes in the land-atmosphere process. It plays an important role in a variety of research fields[38] such as urban planning[15,42,43], agriculture[44,45], environmental monitoring[46,47], and geology[48]. In this context, Landsat series allows a unique opportunity to study long-term trends of LST from 120 to 60 m spatial resolution[33,49]. Registration of radiance data in the thermal infrared region began with the Landsat 4 (1982-1993) with one single band (10.4-12.5 µm). Subsequently, Landsat platforms 5 (1984-2013) and 7 (1999-April 6, 2022) maintained one thermal band, both with 10.4-12.5 µm range, with 100 and 60 m spatial resolution, respectively[32,33,50].

Landsat 8 satellite was launched in 2013 and so far, has been continuously mapping the Earth’s surface in moderate spatial resolution. It carries two sensors onboard, the Operational Land Imager (OLI) and the Thermal Infrared Sensor (TIRS). TIRS registers data in two bands: 10 (10.6-11.19 µm) and 11 (11.5-12.51 µm) with a 100 m resolution[33,50]. However, the United States

Geological Survey (USGS) recommended that band 11 should not be used due to large calibration errors produced by stray light[33,50,51]. Therefore, only Single Channel methods are possible to retrieve the LST for all Landsat series data with pattern.

In 2020, an on-demand Landsat ST product for the entire globe was made available for public access. It is part of the collection of Landsat Level 2 Science Product (L2SP) and retrieves the LST for Landsat 5, 7, and 8 data using the RTE combined with a brightness temperature Lookup Table (LUT) approach[31,52,53]. The importance of using the Single Channel approach is that it allows the generation of standardized LST products for the entire Landsat series.

For the generation of the ST product, atmospheric parameters, emissivity, and thermal radiance are required. Initially, reanalysis profiles from Modern-Era Retrospective Analysis for Research and Applications, Version 2 (MERRA-2) and Goddard Earth Observing System Model, Version 5 (GEOS-5) Forward Processing – Instrument Team (FP-IT) are acquired, the information provided in the profiles from the grids that overlap the Landsat scene and surrounding it are interpolated to time and date of the scene. A DEM is also used to adjust the profile layers in order to calculate the atmospheric parameters to the appropriate elevation of each pixel. After that, the profiles are introduced to the MODTRAN to calculate the three parameters, which are spatially interpolated for each pixel location[31,32,54].

The emissivity is extracted from the Advanced Spaceborne Thermal Emission and Reflection Radiometer Global Emissivity Dataset (ASTER GED) product. It is adjusted to the spectral response function of the Landsat sensor based on the broadband regression approach, which uses regression coefficients derived from spectral library emissivities[33]. Once the ASTER GED gives the mean emissivity in the period of 2000-2008, the emissivity correction is needed in areas that the surface covering changed. In this case, a new emissivity is estimated based on the linear relationship between Normalized Difference Vegetation Index (NDVI) and emissivity, using the NDVI derived from Landsat and ASTER[33,52,54]. The last requirement for LST estimation is the at-sensor radiance, which is obtained from the thermal band (band 10 for the Landsat 8 ST product) after the radiometric calibration.

Several corrections for atmospheric and emissivity effects are involved in the SC methods and on-demand ST products[40,55]. They are based on assumptions and constraints which can cause LST errors. Therefore, it is very important to assess its accuracy to be used with confidence. Many studies have been testing and validating the SC methods[1,6–9,25,28,29,41,56]. These efforts are necessary to contribute to reliable information regarding the quality of the LST product as well as to provide feedback to the developers of LST retrieval algorithms for future improvement[39].

3 Study area

The study area consists of a transgressive dune field on the north coast of Rio Grande do Sul (RS) state, Brazil, between the municipalities of Cidreira and Tramandaí (Fig. 1).

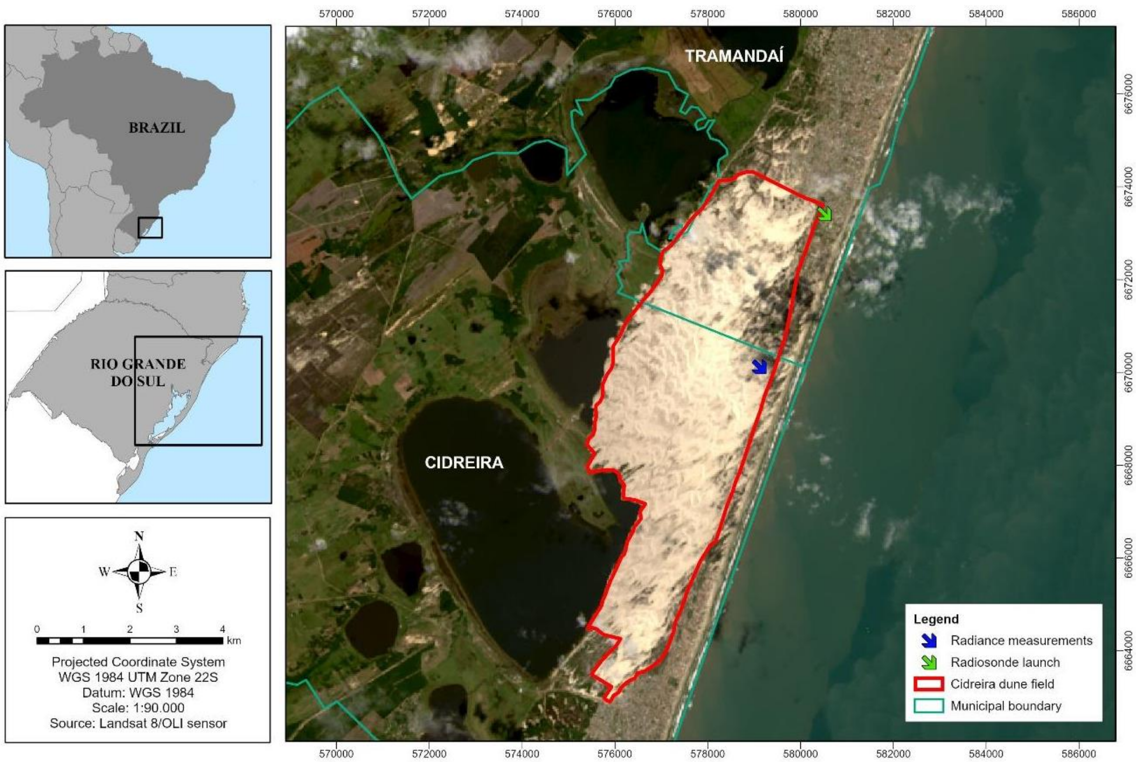

Fig. 1 Study area of Cidreira dune – Rio Grande do Sul - Brazil.

This area is an experimental site considered a pseudo-invariant target. It has about 30 km² and is known as Cidreira dune field, where the fine sands (sizes between 125-250 μm) are composed of 99.53% of quartz (SiO_2) and 0.47% of heavy minerals[28,57].

4 Data Acquisition and Methods

4.1 Landsat 8 data and on-demand ST product

One scene from Landsat 8 OLI/TIRS Collection 1 Level-1 captured in the summer season was acquired[58] and Table 1 shows its information.

Table 1 Landsat 8 scene information.

Time	Path/Row	Solar Angle
Mar. 14, 2018	220/81	47.37° (zenith)
13:12.06		55.75° (azimuth)

The band 10 (10.6-11.19 μm) was used for the LST retrieval. It was chosen since has less atmospheric influence, decreasing the uncertainties in the LST[9]. We select a subset of 31215 pixels corresponding to the Cidreira dune field delimitation.

First, the radiometric calibration was applied to obtain the spectral radiance[50], as follows:

$$L_{sens} = M_L * DN + A_L \quad (1)$$

wherein L_{sens} is the at-sensor radiance ($Wm^{-2}sr^{-1}\mu m^{-1}$), M_L is the multiplicative scaling factor for the band equal to 3.342×10^{-4}, A_L is the additive scaling factor equal 0.1 and DN is the pixel value in digital number.

The brightness temperature at Top of Atmosphere (TOA) also is required in the LST retrieval, thus Eq. (2) was used for its calculation[50].

$$BT_{TOA} = \frac{K_2}{ln\left(\frac{K_1}{L_{sens}}+1\right)} \quad (2)$$

wherein BT_{TOA} is the brightness temperature at TOA. K_1 and K_2 are band-specific thermal conversion constants, respectively 774 and 1321 in $Wm^{-2}sr^{-1}\mu m^{-1}$.

We also acquired the on-demand ST product from the selected scene that provides the LST in Kevin. Moreover, we obtained two auxiliary data from the product, which were the emissivity band (derived from ASTER GED) and the quality band. This last one contains LST errors related to the uncertainties produced by the emissivity estimation, atmospheric compensation, instrument, and presence of clouds in the scene[54].

4.2 Land Surface Temperature retrieval

We used in this paper the Radiative Transfer Equation (RTE), Generalized Single Channel (GSC), and Improved Single Channel (ISC) algorithms. These methods require previous knowledge of emissivity. The main difference between them refers to the data necessary for atmospheric correction. The effective wavelength of 10.904 μm from the band 10 was applied in all retrievals[9]. The algorithms were written and applied over the Landsat image in a Python environment.

4.2.1 Radiative Transfer Equation

Assuming a cloud-free atmosphere under local thermodynamic equilibrium, an approximation of the RTE is given by:

$$L_{\lambda\ sens} = \left[\varepsilon_\lambda B_\lambda(Ts) + (1-\varepsilon_\lambda) L_\lambda{}^{\downarrow}\right]\tau_\lambda + L_\lambda{}^{\uparrow} \quad (3)$$

where $L_{\lambda sens}$ is the at-sensor spectral radiance, ε_λ is the spectral emissivity, $L_\lambda{}^{\downarrow}$ is the downwelling atmospheric radiance, $L_\lambda{}^{\uparrow}$ is the upwelling atmospheric radiance, τ_λ is atmospheric transmittance, and $B_\lambda(Ts)$ corresponds to the Blackbody radiance emitted at a temperature of Ts.

Inverting Eq. (3), it is possible to obtain the Ts as follows:

$$LST = Ts = \frac{K_2}{ln\left(\frac{K_1}{\frac{L\ sens - L^{\uparrow} - \tau(1-\varepsilon)L^{\downarrow}}{\varepsilon\tau}} + 1\right)} \quad (4)$$

where Ts is the LST in Kelvin. K_1 and K_2 are band-specific thermal conversion constants, previously defined. The wavelength was pulled out, once the formulation was derived from the spectral response of the Landsat 8 band 10.

4.2.2 Generalized Single Channel

Reference 9 developed the Generalized Single Channel (GSC), where a linear relationship between radiance and temperature is obtained from Planck's law, and the LST can be retrieved by Eq. (5).

$$T_s = \gamma\left[\frac{1}{\varepsilon}(\psi_1 L_{sens} + \psi_2) + \psi_3\right] + \delta \quad (5)$$

wherein T_s is the LST in Kelvin, ε is the emissivity, L_{sens} is the at-sensor radiance, and ψ_1, ψ_2, ψ_3 are atmospheric functions. The γ and δ are derived from the Planck equation, as follows:

$$\gamma = \left\{\frac{C_2 L_{sens}}{(BT_{TOA})^2}\left[\frac{\lambda^4 L_{sens}}{C_1} + \frac{1}{\lambda}\right]\right\}^{-1} \tag{6}$$

$$\delta = -\gamma L_{sens} + BT_{TOA} \tag{7}$$

wherein C_1 is equal to 1.19104x10^8 Wμm^{-2}sr^{-1} and C_2 is equal to 14387.7 μm, BT_{TOA} is brightness temperature at TOA, and λ is the effective wavelength.

The GSC algorithm takes into account the amount of water vapor (ω) as the main absorber in the atmosphere[9]. Thus, the atmospheric functions (ψ_1, ψ_2, and ψ_3) can be estimated through Eqs. (8), (9), and (10), supported by an empirical relationship between the water vapor and atmospheric parameters.

$$\psi_1 = 0.04019\omega^2 + 0.02916\omega + 1.01523 \tag{8}$$

$$\psi_2 = -0.38333\omega^2 - 1.50294\omega + 0.20324 \tag{9}$$

$$\psi_3 = 0.00918\omega^2 + 1.36072\omega - 0.27514 \tag{10}$$

4.2.3 Improved Single Channel

Improved Single Channel (ISC) algorithm[6,7] retrieves the LST using the above-mentioned Eq. (5), (6), and (7). However, the atmospheric functions are obtained as a function of the water vapor content (ω) and the mean atmospheric temperature (T_a). The atmospheric functions are calculated as follows:

$$\psi_1 = -7.2122\omega^2 + 0.00005{T_a}^2 - 2.452321\omega - 0.026275T_a - 0.00005{T_a}^2\omega + 0.02317T_a\omega + 0.04663T_a\omega^2 - 0.00007{T_a}^2\omega^2 + 4.47297 \tag{11}$$

$$\psi_2 = 89.61569\omega^2 - 0.00038{T_a}^2 + 106.55093\omega + 0.21578T_a + 0.00141{T_a}^2\omega - 0.78444T_a\omega - 0.5732T_a\omega^2 + 0.00091{T_a}^2\omega^2 - 30.37028 \tag{12}$$

$$\psi_3 = -14.65955\omega^2 - 0.0001{T_a}^2 - 79.95838\omega + 0.4181T_a - 0.00091{T_a}^2\omega + 0.54535T_a\omega + 0.09114T_a\omega^2 - 0.00014{T_a}^2\omega^2 - 3.76184 \quad (13)$$

4.3 Emissivity estimation from field measurements

A field campaign in the study area was carried out by the UFRGS Geological Remote Sensing Laboratory on March 14, 2018. There, a set of radiance measurements of quartz were taken using a Fourier-transform Infrared spectrometer (μFTIR; 102F model), with a spectral range of 2 to 16 μm and spectral resolution of 4.8 or 16 cm-1, at coordinates 30°5'56.53"S and 50°10'37.72"W (Fig. 1). A homogeneous and bare area was selected and the measurements were made concurrently with Landsat 8 overpass, see Ref. 28 for a detailed description.

The spectral emissivity (ε_λ) of quartz was calculated as follows[59]:

$$\varepsilon_\lambda = \frac{L_\lambda - {L_\lambda}^{\downarrow}}{B_\lambda(T) - {L_\lambda}^{\downarrow}} \quad (14)$$

wherein L_λ is the spectral radiance of quartz, $L_\lambda^{\downarrow}$ is the atmospheric downwelling radiance which was registered by a golden reference panel with an emissivity of 0.04, and $B_\lambda(T)$ is the radiance derived by Planck's law given as[60]:

$$B_\lambda(T) = \frac{C_1\lambda^{-5}}{exp\left(\frac{C_2}{\lambda T}\right) - 1} \quad (15)$$

wherein C_1 and C_2 are constants (C_1 = 1.191x10^8 Wμm^{4}sr^{-1}m^{-2}, C_2 = 1.439x$10^4$$\mu$mK), λ is the wavelength and T is the radiometric temperature. Assuming that $\varepsilon = 1$ between 7.5 and 8 μm, the sample temperature can be obtained by the inversion of (15). This wavelength range was chosen because the emissivity and temperature retrieval are most accurate at the maximum emissivity value[40,61].

4.4 Atmospheric Data

Atmospheric profiles provide the real state of the atmosphere with information of temperature (K), pressure (hPa), and relative humidity[21–23,62]. We acquired two atmospheric profiles. The first was registered in the field by a radiosonde launched during the satellite overpass (Fig. 1), also by the UFRGS Geological Remote Sensing Laboratory campaign. The second one consisted of an interpolated profile generated by ACPC[18] using the NCEP reanalysis data. It is the initial input used in the atmospheric correction parameters estimation[20]. We obtained the interpolated profile at the coordinates and time of the field measurements, i.e., at 30°5'56.53"S and 50°10'37.72"W on March 14, 2018 at 13:12 pm.

4.4.1 Atmospheric Correction Parameters

In this study, we used the radiative transfer code MODTRAN 4, version3r1, developed by the U.S. Air Force Research Laboratory[16], to estimate the atmospheric correction parameters (τ, $L_\lambda^{\downarrow}$, $L_\lambda^{\uparrow}$). We set the spectral response curve of Landsat 8 band 10 and used the radiosonde atmospheric profile as initial input.

It is important to note that MODTRAN requires profiles reaching the space, i.e., up to 100 km, however, the radiosonde profile provides information only up to 30 km. Therefore, we applied the ACPC methodology[18,19] and completed the radiosonde profile (30-100km) with the available MODTRAN Standard Atmosphere, the standard mid-latitude summer profile[63].

4.4.2 Water vapor content and mean atmospheric temperature

We used the interpolated profile generated by ACPC to calculate ω (Eq. 16) and T_a (Eq. 18), as follows:

$$\omega = \frac{0.493\varphi_r P_S}{T_o} \tag{16}$$

wherein ω is the water vapor in g.cm^{-2} and φ_r is the relative humidity in the first layer of the atmospheric profile, and P_s is the partial pressure given by:

$$P_s = exp\left(26.23 - \frac{5416}{T_o}\right) \qquad (17)$$

wherein P_s is the partial pressure and T_o is the temperature in the first layer of the vertical profile.

The mean atmospheric temperature (T_a) was calculated using Eq. (18). This formulation gives a linear function between T_a and near-surface air temperature (T_o) from the mid-latitude summer standard atmosphere for clear sky conditions[11].

$$T_a = 16.011 + 0.9262T_o \qquad (18)$$

wherein T_o is the near-surface air temperature assumed to be the temperature in the first layer of the interpolated atmospheric profile.

4.5 Comparative analysis

We obtained LSTs through the GSC, and ISC algorithms, and on-demand ST product. To validate the results, we compared them with the estimated LST by using the RTE and the atmospheric correction parameters derived from radiosonde profile, this was assumed as our ground truth. It is important to mention that the *in situ* spectral emissivity of quartz (0.9798) was applied for all the LST retrieval methods. According to Ref. 56, a minimum LST error of 0.3 K is obtained by applying *in situ* data for atmospheric and emissivity correction.

Comparative analysis between the LSTs was made by employing the following statistical metrics[35]: Standard Deviation (STD) in Eq. (19); Systematic error (Bias) in Eq. (20); Mean Absolute Error (MAE) in Eq. (21); Root Mean Square Error (RMSE) in Eq. (22); and Pearson correlation coefficient (r) in Eq. (23).

$$STD = \sqrt{\frac{\sum_{i=1}^{n}(p_i - \bar{p})^2}{n-1}} \quad (19)$$

$$Bias = \frac{1}{n}\sum_{i=1}^{n}(o_i - p_i) \quad (20)$$

$$MAE = \frac{1}{n}\sum_{i=1}^{n}|o_i - p_i| \quad (21)$$

$$RMSE = \frac{1}{n}\sqrt{\sum_{i=1}^{n}(o_i - p_i)^2} \quad (22)$$

$$r = \frac{\sum(o_i - \bar{o})(p_i - \bar{p})}{\sqrt{\sum(o_i - \bar{o})^2}\sqrt{\sum(p_i - \bar{p})^2}} \quad (23)$$

In presented equations, n is the number of observations, o_i is the observed temperature (ground truth), p_i is the predicted temperature, and $\bar{o}$ and $\bar{p}$ are observed and predicted means, respectively.

Furthermore, evaluating the on-demand ST product performance, we compared the emissivity band from the product with the *in-situ* emissivity. Also, LST errors found in the product quality band were analyzed against the results obtained for the ST product in our comparative analysis.

5 Results and discussion

In this paper, retrieved LST through RTE combined with *in situ* data was used to validate retrieved LSTs by GSC, ISC, and on-demand ST product. Spatial distribution of LSTs is presented in Fig. 2.

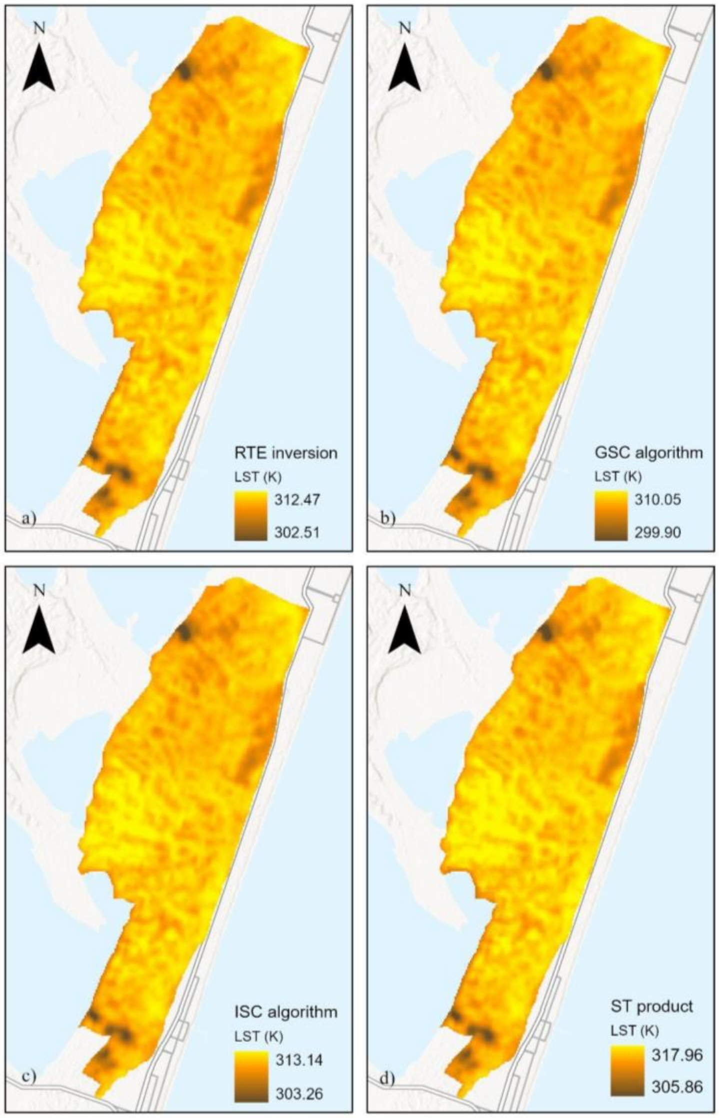

Fig. 2 Spatial distribution of retrieved LSTs over Cidreira dunes with: (a) RTE inversion (b) GSC (c) ISC (d) on-demand ST product.

5.1 GSC algorithm validation

GSC presented an STD of 1.58 K, an RMSE of 2.5 K, and a strong correlation with the ground truth (r=0.99). However, underestimating in -2.5 K (Bias), which can be seen in the displacement of the red histogram in Fig. 3a. Approximately 40 to 43% of the pixels contained an error ranging from -2.46 K to -2.53 K as shown in Fig. 3b.

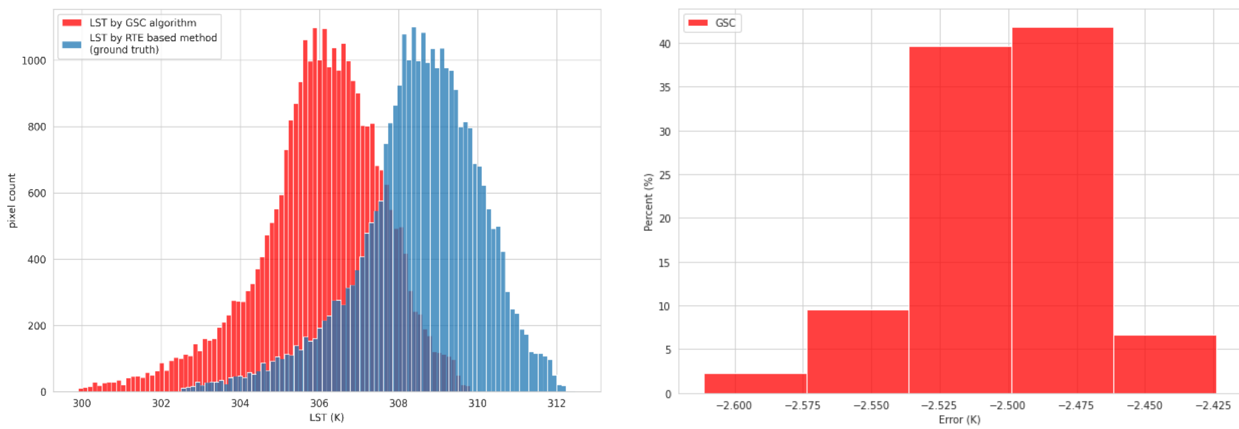

(a) (b)

Fig. 3 Retrieved LST by the GSC algorithm: (a) comparing to the ground truth (b) distribution of LST errors.

Studies that validated the GSC reported an RMSE between 1 K and 2 K for thermal data from Landsat 4, 5, and 7 [1,10,41,64]. Reference 15 found an RMSE range from 1.26 K to 1.61 K using Landsat 8 band 10. Data from other satellites/sensors such as NOAA/AVHRR, ERS-2/ATSR-2, and TERRA/ASTER were tested with GSC, and an RMSE lower than 2 K was achieved[1]. It is important to note that all these errors were obtained in low atmospheric water vapor (ω<3 g.cm^{-2}).

On the other hand, LST errors increased when GSC was used in high water vapor conditions (ω>3 g.cm^{-2}). Applying GSC for Landsat 8 band 10, Ref. 3 found an RMSE higher than 2.7 K, and Ref. 28 reported an error of -2.71 K in an experiment over Cidreira dunes. In our results, an RMSE of 2.5 K was obtained, also due to the high estimated water vapor of 3.04 g.cm^{-2}.

In agreement with Ref. 28, the proximity of the study area to the sea surface leads to high humidity, and worse results can be expected for the GSC. This has already been proved in sensitivity analysis carried out by Ref. 9. They found an RMSE of 1.5 K for ω < 3 g.cm^{-2} and an RMSE ranged from 3 to 4 K for ω > 3 g.cm^{-2}.

5.2 ISC algorithm validation

ISC presented an STD of 1.54 K with an RMSE of 0.69 K showing best performance and highly correlated with the ground truth (r=0.99). Different from GSC, the ISC overestimated at 0.69 K (Bias) the LST by RTE, the overlapping of histograms in Fig. 4a shows LSTs approximations. Almost 60% of pixels showed an error varying from 0.69-0.7 K (Fig. 4b).

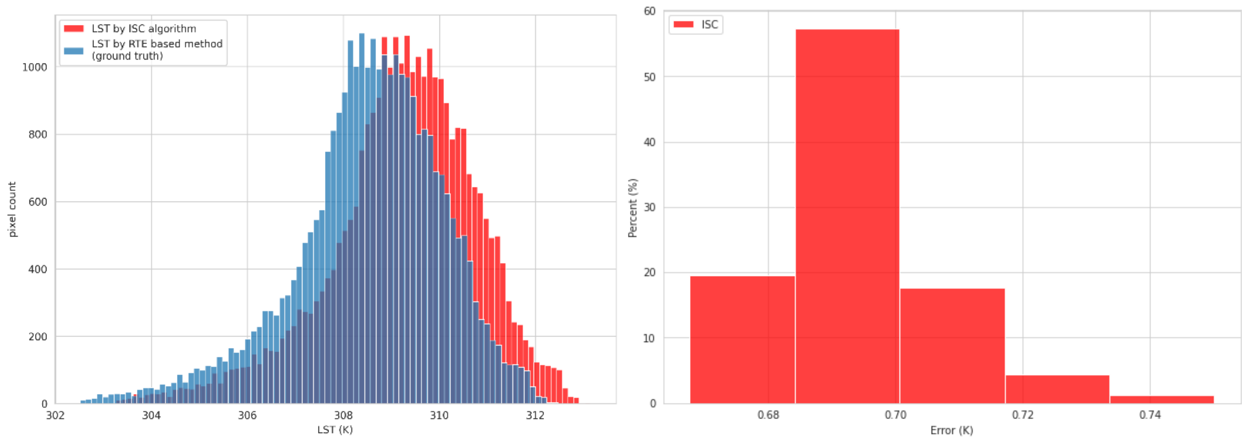

(a) (b)

Fig. 4 Retrieved LST by the ISC algorithm: (a) comparing to the ground truth (b) distribution of LST errors.

Reference 6 introduced the mean atmospheric temperature (T_a) into the GSC in order to minimize LST errors and maintain the operationality of the algorithm. Improvement was successfully obtained as shown in ISC validation studies. Ref. 6 found an RMSE of 0.5 K and 1 K for Landsat 5 and 7 data, respectively. They observed that T_a addition reduced errors in LST, especially for high water vapor conditions.

Reference 7 applied the ISC using Landsat 8 band 10 and reported an RMSE around 1 K, and a mean difference of -0.5 K with the ground truth. They noticed that the ISC has better performance over constant emissivity conditions, such as ice surface. This was proved by Ref. 29 that estimated the LST over snow and found great results for ISC with an RMSE of 0.32 K and small bias of -0.06 K.

Retrieving LST for nine bands 10 from Landsat 8 (2018-2019) in the Cidreira dunes, Ref. 30 found an RMSE of 1.6 K for ISC. Satisfactory results were reported by Ref. 28, which obtained an error of 0.6 K comparing a single pixel with *in situ* temperature. Both studies estimated the water vapor and mean atmospheric temperature using data from local meteorological station.

Our study area is characterized by high humidity and the inclusion of T_a provided better performance for ISC (RMSE lower than 0.7 K). This is in accordance with the above-mentioned studies. Moreover, the pseudo-invariant target, which is a very homogeneous area (99.53% of quartz) with almost constant emissivity, can contribute to remarkable results for ISC.

5.3 On-demand Landsat 8 ST product validation

Evaluating the on-demand ST product, we found an STD of 1.8 K and a high RMSE of 4.24 K. It was highly correlated with the ground truth (r=0.98), however, overestimating it by 4.3 K (Bias). This can be seen by the distance between the histograms in Fig. 5a. About 80% of the pixels showed an error of 4 K to 4.5 K (Fig. 5b).

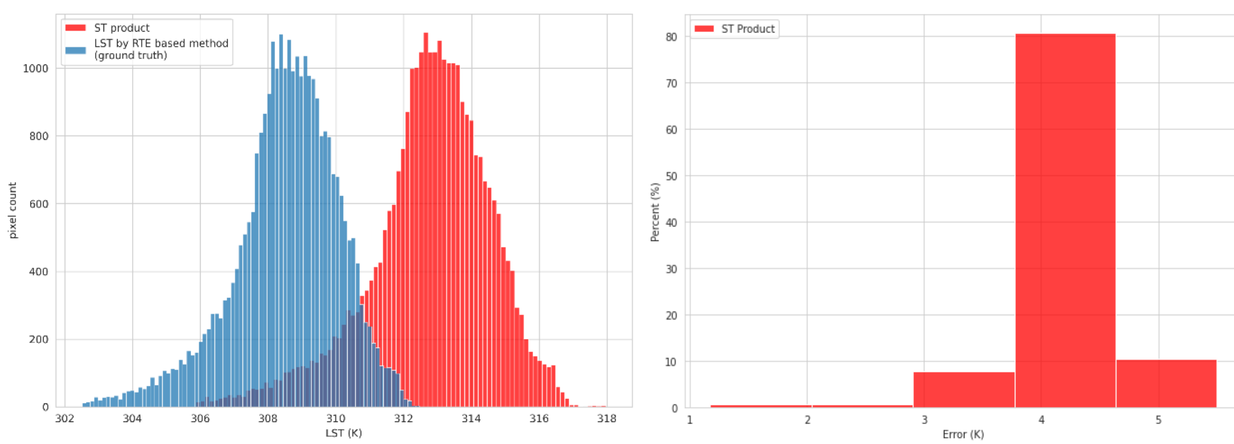

(a) (b)

Fig. 5 LST from the ST product: (a) comparing to the ground truth (b) distribution of LST errors.

Until the development of this research, validation of the ST product from Landsat 8 had only been addressed in North America. Therefore, one of our purposes was to evaluate its performance in the Southern Hemisphere conditions, contributing to the product enhancement.

Reference 33 validated the ST products derived from Landsat 5 and 7. Over vegetated surfaces, they found an RMSE of 2.2 K and bias of 0.7 K (Landsat 5), and an RMSE of 2.3 K and bias of 0.9 K (Landsat 7). On the other hand, the products presented an RMSE of 0.6 K and bias of -0.3 K (Landsat 5), and an RMSE of 0.7 K and bias of 0.4 K (Landsat 7) over water bodies. As the target has a well-known emissivity, they associated these errors to the atmospheric correction.

According to Ref. 32, the products presented worst performance in humid atmospheres. They validated Landsat 7 ST products and reported an RMSE of 2.61 K for atmospheric transmittance less than 30%. This error decreased to 0.81 K when transmittance was 85%. Ref. 31 validated the Landsat 8 ST product for cloud free conditions, an average error of -0.56 K and a STD of 0.76 K were obtained.

Reference 34 validated ST products derived from Landsat 5, 7, and 8. Best performance was presented over water bodies (RMSE of 1.1 K) and snow (RMSE of 1.6 K) due to the constant emissivity. An RMSE less than 2.1 K was obtained for vegetated sites. For barren surfaces, the products showed an RMSE of 2.8 K. The authors reported that an RMSE higher than 3 K can be expected over heterogeneous surfaces due incorrect emissivity adjustment.

Our validation showed poor performance for the ST product in a dune field (RMSE of 4.24 K). In agreement with Ref. 32, this result can be related to the high humid atmosphere of our study area once that, at this condition, higher errors can be expected for the product. In addition, an error in the emissivity estimation also can have contributed to the ST product performance.

We extract the pixel from the emissivity band of the product ($\varepsilon = 0.9491$) that matched with the coordinates of our *in situ* spectral emissivity of quartz ($\varepsilon = 0.9798$). As reported by Ref. 61, emissivity is measured by the μFTIR with high accuracy (instrument used in our field measurement). Thus, comparing our emissivity with that used for the product, a significant difference of 0.03 was obtained.

According to Ref. 1, an error on the emissivity of 0.01 induces an error of approximately 0.6 K in the LST. Thus, the emissivity difference found can provide an LST error of 1.8 K. This value can be higher than 3 K in the product due to the incorrect emissivity estimation, as reported by Ref. 34. Moreover, it must be noted that the emissivity pixels from ASTER GED originally have 100 m or 1 km of spatial resolution. They are resampled to 30 m for use in the Landsat ST products generation.

We compare the LST errors obtained in our validation for the on-demand ST product against the LST errors in the quality band of the product (Fig. 6a). In the quality band, about 50% of the pixels presented an LST error around 3 K and approximately 35% an error of 4 K, as can be seen in Fig. 6b.

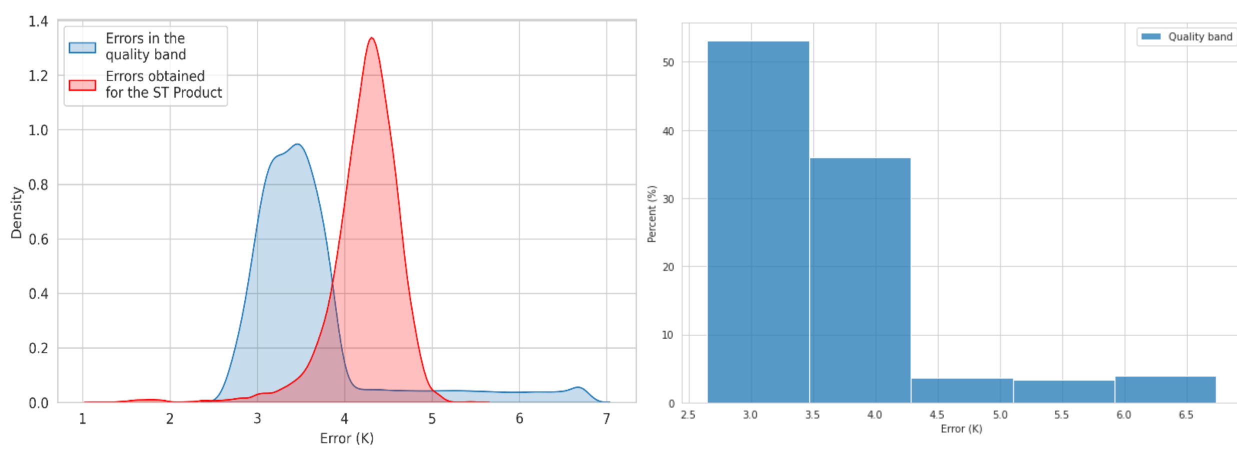

(a) (b)

Fig. 6 LST errors obtained in our validation and in the quality band: (a) comparing the density of pixels for each one (b) LST errors distribution in the quality band.

The quality band indicated a smoothed distribution of the LST errors between 3 K and 4 K for all pixels. On the other hand, our validation showed high concentration of pixels from the ST product with errors around 4.5 K (red peak in Fig. 6a). The errors estimated by the quality band are relatively smaller. Nevertheless, as mentioned before, the product showed an incorrect emissivity estimation and poor performance in a humid environment. Therefore, it can be that the atmospheric correction carried out in the product has compensated for the emissivity errors.

5.4 Overall validation results

In our validation, LST products showed a high correlation (r=0.99 and 0.98) with LST data from the field experiment, resulting in a better performance for ISC (RMSE of 0.69 K), followed by GSC (RMSE of 2.5 K) and ST (RMSE of 4.24 K), see Table 2.

Table 2 Statistical metrics for LST retrieval applying the GSC and ISC algorithms, and the on-demand ST product.

Statistical metrics	retrieved LST by GSC	retrieved LST by ISC	LST from ST product
Mean	306.03 K	309.22 K	312.76 K
STD	1.58 K	1.54 K	1.8 K
Bias	-2.5 K	0.69 K	4.23 K
MAE	2.5 K	0.69 K	4.23 K
RMSE	2.5 K	0.69 K	4.24 K
r	0.99	0.99	0.98

The box-plot graph shown in Fig. 7 displays the distributional characteristics (mean, minimum, maximum, and quartiles) for each LST retrieval method.

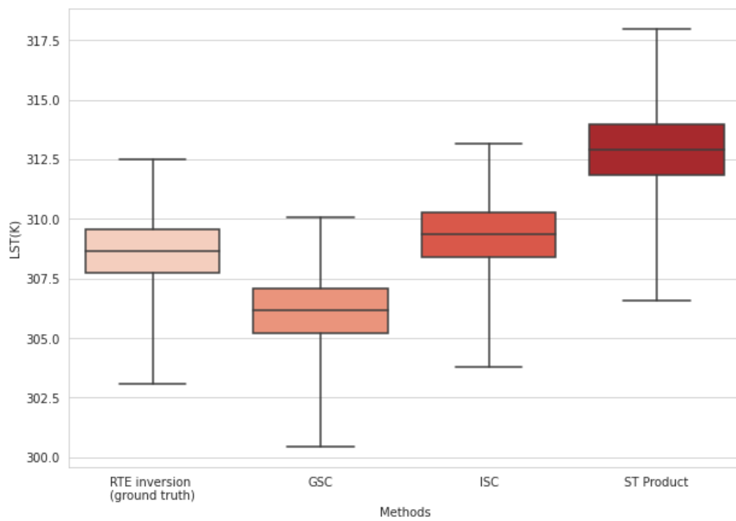

Fig. 7 Box-plot graph with the retrieved LST distribution by each method.

Analyzing the LSTs distribution, we can see that the ISC algorithm has the highest level of agreement with our ground truth (retrieved LST by RTE), then the GSC, and finally the ST product with the lowest agreement.

6 Conclusions

In this study, we compared LSTs obtained with GSC, and ISC algorithms, and on-demand ST product. Derived temperatures were validated with the estimated LST by using the RTE and the atmospheric correction parameters derived from radiosonde profile. Retrieved LSTs showed a high correlation (r=0.99 and 0.98) with LST data from the field experiment, resulting in a better performance for ISC (RMSE of 0.69 K), followed by GSC (RMSE of 2.5 K) and ST product (RMSE of 4.24 K).

The high water vapor content was the main source of errors in GSC. The inclusion of the mean atmospheric temperature in the ISC significantly reduced the LST errors. ISC was shown to be suitable for the high humidity of our study area. Conversely, for the on-demand ST product, this atmospheric condition and the incorrect emissivity estimation can have provided poor performance.

These findings complement and reinforce the research developed in the area. In addition, Single Channel methods allow retrieving LST of thermal data from almost 40 years of the Landsat Program, since 1984. Our study showed that the ISC algorithm can be used with 0.69 K of confidence to estimate long-term trends of LST in the Southern Hemisphere. It is important to mention that although the dune field is mostly composed of quartz there are a few undergrowth and moisture areas. Moreover, seasonal analysis of SC methods can be addressed in future research.

Disclosures

The authors declare no conflict of interest.

Acknowledgments

This research was supported by the Laboratory of Geological Remote Sensing of the State Center for Remote Sensing and Meteorology Research (CEPSRM) and was financed, in part, by the Coordination for Improvement of Higher Education Personnel – CAPES (*Coordenação de Aperfeiçoamento de Pessoal de Nível Superior*). The Landsat 8 data were courtesy of the US Geological Survey (USGS).

References

1. J. C. Jiménez-Munoz and J. A. Sobrino, "A generalized single-channel method for retrieving land surface temperature from remote sensing data," Journal of Geophysical Research: Atmospheres **108**(D22), 4688, John Wiley & Sons, Ltd (2003) [doi:10.1029/2003JD003480].

2. H. Tang and Z.-L. Li, “Quantitative Remote Sensing in Thermal Infrared,” Springer Berlin Heidelberg, Berlin, Heidelberg (2014) [doi:10.1007/978-3-642-42027-6].

3. A. Sekertekin and S. Bonafoni, “Land Surface Temperature Retrieval from Landsat 5, 7, and 8 over Rural Areas: Assessment of Different Retrieval Algorithms and Emissivity Models and Toolbox Implementation,” Remote Sensing 2020, Vol. 12, Page 294 **12**(2), 294, Multidisciplinary Digital Publishing Institute (2020) [doi:10.3390/RS12020294].

4. S. B. Duan et al., “Land-surface temperature retrieval from Landsat 8 single-channel thermal infrared data in combination with NCEP reanalysis data and ASTER GED product,” https://doi.org/10.1080/01431161.2018.1460513 **40**(5–6), 1763–1778, Taylor & Francis (2018) [doi:10.1080/01431161.2018.1460513].

5. B. Tardy et al., “A Software Tool for Atmospheric Correction and Surface Temperature Estimation of Landsat Infrared Thermal Data,” Remote Sensing 2016, Vol. 8, Page 696 **8**(9), 696, Multidisciplinary Digital Publishing Institute (2016) [doi:10.3390/RS8090696].

6. J. Cristóbal et al., “Improvements in land surface temperature retrieval from the Landsat series thermal band using water vapor and air temperature,” Journal of Geophysical Research: Atmospheres **114**(D8), 8103, John Wiley & Sons, Ltd (2009) [doi:10.1029/2008JD010616].

7. J. Cristóbal et al., “An Improved Single-Channel Method to Retrieve Land Surface Temperature from the Landsat-8 Thermal Band,” Remote Sensing 2018, Vol. 10, Page 431 **10**(3), 431, Multidisciplinary Digital Publishing Institute (2018) [doi:10.3390/RS10030431].

8. J. C. Jiménez-Muñoz and J. A. Sobrino, “A single-channel algorithm for land-surface temperature retrieval from ASTER data,” IEEE Geoscience and Remote Sensing Letters **7**(1), 176–179 (2010) [doi:10.1109/LGRS.2009.2029534].

9. J. C. Jimenez-Munoz et al., “Land surface temperature retrieval methods from landsat-8 thermal infrared sensor data,” IEEE Geoscience and Remote Sensing Letters **11**(10), 1840–1843, Institute of Electrical and Electronics Engineers Inc. (2014) [doi:10.1109/LGRS.2014.2312032].

10. J. A. Sobrino, J. C. Jiménez-Muñoz, and L. Paolini, “Land surface temperature retrieval from LANDSAT TM 5,” Remote Sensing of Environment **90**(4), 434–440, Elsevier (2004) [doi:10.1016/J.RSE.2004.02.003].

11. Z. Qin, A. Karnieli, and P. Berliner, “A mono-window algorithm for retrieving land surface temperature from Landsat TM data and its application to the Israel-Egypt border region,” International Journal of Remote Sensing **22**(18), 3719–3746, Taylor & Francis Group (2001) [doi:10.1080/01431160010006971].

12. J. A. Sobrino et al., “Improvements in the Split-Window Technique for Land Surface Temperature Determination,” IEEE Transactions on Geoscience and Remote Sensing **32**(2), 243–253 (1994) [doi:10.1109/36.295038].

13. F. Becker and Z. L. Li, “Towards a local split window method over land surfaces,” http://dx.doi.org/10.1080/01431169008955028 **11**(3), 369–393, Taylor & Francis Group (2007) [doi:10.1080/01431169008955028].

14. L. M. McMillin, “Estimation of sea surface temperatures from two infrared window measurements with different absorption,” Journal of Geophysical Research **80**(36), 5113–5117, John Wiley & Sons, Ltd (1975) [doi:10.1029/JC080I036P05113].

15. X. Yu, X. Guo, and Z. Wu, “Land Surface Temperature Retrieval from Landsat 8 TIRS—Comparison between Radiative Transfer Equation-Based Method, Split Window Algorithm and Single Channel Method,” Remote Sensing 2014, Vol. 6, Pages 9829-9852 **6**(10), 9829–9852, Multidisciplinary Digital Publishing Institute (2014) [doi:10.3390/RS6109829].

16. A. Berk et al., “MODTRAN Cloud and Multiple Scattering Upgrades with Application to AVIRIS,” Remote Sensing of Environment **65**(3), 367–375, Elsevier (1998) [doi:10.1016/S0034-4257(98)00045-5].

17. J. Yang et al., “Evaluation of Seven Atmospheric Profiles from Reanalysis and Satellite-Derived Products: Implication for Single-Channel Land Surface Temperature Retrieval,” Remote Sensing

2020, Vol. 12, Page 791 **12**(5), 791, Multidisciplinary Digital Publishing Institute (2020) [doi:10.3390/RS12050791].

18. J. A. Barsi, J. L. Barker, and J. R. Schott, “An Atmospheric Correction Parameter Calculator for a Single Thermal Band Earth-Sensing Instrument,” International Geoscience and Remote Sensing Symposium (IGARSS) **5**, 3014–3016 (2003) [doi:10.1109/IGARSS.2003.1294665].
19. J. A. Barsi et al., “Validation of a web-based atmospheric correction tool for single thermal band instruments,” https://doi.org/10.1117/12.619990 **5882**, 136–142, SPIE (2005) [doi:10.1117/12.619990].
20. S. Saha et al., “The NCEP Climate Forecast System Version 2,” Journal of Climate **27**(6), 2185–2208, American Meteorological Society (2014) [doi:10.1175/JCLI-D-12-00823.1].
21. X. Meng and J. Cheng, “Evaluating Eight Global Reanalysis Products for Atmospheric Correction of Thermal Infrared Sensor—Application to Landsat 8 TIRS10 Data,” Remote Sensing 2018, Vol. 10, Page 474 **10**(3), 474, Multidisciplinary Digital Publishing Institute (2018) [doi:10.3390/RS10030474].
22. L. R. Diaz et al., “Land Surface Temperature Retrieval Using High-Resolution Vertical Profiles Simulated by WRF Model,” Atmosphere 2021, Vol. 12, Page 1436 **12**(11), 1436, Multidisciplinary Digital Publishing Institute (2021) [doi:10.3390/ATMOS12111436].
23. L. R. Diaz et al., “Using the WRF Model to Refine NCEP CFSv2 Reanalysis Atmospheric Profile: A Southern Brazil Test Case,” Brazilian Journal of Geophysics **38**(2), 5–31, Sociedade Brasileira de Geofisica (2020) [doi:10.22564/RBGF.V38I2.2043].
24. Z. Zhang et al., “Towards an operational method for land surface temperature retrieval from Landsat 8 data,” https://doi.org/10.1080/2150704X.2015.1130877 **7**(3), 279–288, Taylor & Francis (2016) [doi:10.1080/2150704X.2015.1130877].
25. A. Sekertekin, “Validation of Physical Radiative Transfer Equation-Based Land Surface Temperature Using Landsat 8 Satellite Imagery and SURFRAD in-situ Measurements,” Journal of

Atmospheric and Solar-Terrestrial Physics **196**, 105161, Pergamon (2019) [doi:10.1016/J.JASTP.2019.105161].

26. J. C. Jiménez-Muñoz et al., “Atmospheric correction of optical imagery from MODIS and Reanalysis atmospheric products,” Remote Sensing of Environment **114**(10), 2195–2210, Elsevier (2010) [doi:10.1016/J.RSE.2010.04.022].
27. J. A. Sobrino et al., “Land surface emissivity retrieval from different VNIR and TIR sensors,” IEEE Transactions on Geoscience and Remote Sensing **46**(2), 316–327 (2008) [doi:10.1109/TGRS.2007.904834].
28. P. S. Kafer et al., “Land surface temperature retrieval by landsat 8 thermal band: Applications of laboratory and field measurements,” IEEE Journal of Selected Topics in Applied Earth Observations and Remote Sensing **12**(7), 2332–2341, Institute of Electrical and Electronics Engineers (2019) [doi:10.1109/JSTARS.2019.2913822].
29. Y. Li et al., “An Improved Single-Channel Polar Region Ice Surface Temperature Retrieval Algorithm Using Landsat-8 Data,” IEEE Transactions on Geoscience and Remote Sensing **57**(11), 8557–8569, Institute of Electrical and Electronics Engineers Inc. (2019) [doi:10.1109/TGRS.2019.2921606].
30. P. S. Käfer et al., “COMPARATIVE ANALYSIS OF SPLIT-WINDOW AND SINGLE-CHANNEL ALGORITHMS FOR LAND SURFACE TEMPERATURE RETRIEVAL OF A PSEUDO-INVARIANT TARGET,” Boletim de Ciências Geodésicas **26**(2), 1–17, Universidade Federal do Paraná (2020) [doi:10.1590/S1982-21702020000200008].
31. M. Cook et al., “Development of an Operational Calibration Methodology for the Landsat Thermal Data Archive and Initial Testing of the Atmospheric Compensation Component of a Land Surface Temperature (LST) Product from the Archive,” Remote Sensing 2014, Vol. 6, Pages 11244-11266 **6**(11), 11244–11266, Multidisciplinary Digital Publishing Institute (2014) [doi:10.3390/RS61111244].

32. K. G. Laraby and J. R. Schott, “Uncertainty estimation method and Landsat 7 global validation for the Landsat surface temperature product,” Remote Sensing of Environment **216**, 472–481, Elsevier (2018) [doi:10.1016/J.RSE.2018.06.026].
33. N. K. Malakar et al., “An Operational Land Surface Temperature Product for Landsat Thermal Data: Methodology and Validation,” IEEE Transactions on Geoscience and Remote Sensing **56**(10), 5717–5735, Institute of Electrical and Electronics Engineers Inc. (2018) [doi:10.1109/TGRS.2018.2824828].
34. S. B. Duan et al., “Validation of Landsat land surface temperature product in the conterminous United States using in situ measurements from SURFRAD, ARM, and NDBC sites,” https://doi.org/10.1080/17538947.2020.1862319 **14**(5), 640–660, Taylor & Francis (2020) [doi:10.1080/17538947.2020.1862319].
35. Pierre Guillevic et al., “Land Surface Temperature Product Validation Best Practice Protocol,” pp. 1–58, Land Product Validation Subgroup (WGCV/CEOS) (2018).
36. A. Benmecheta, A. Abdellaoui, and A. Hamou, “A comparative study of land surface temperature retrieval methods from remote sensing data,” http://dx.doi.org/10.5589/m13-008 **39**(1), 59–73, Taylor & Francis (2014) [doi:10.5589/M13-008].
37. I. J. Barton, “ Satellite-derived sea surface temperatures: A comparison between operational, theoretical and experimental algorithms,” Journal of Applied Meteorology **31**(5), 433–442 (1992).
38. J. A. Sobrino et al., “Review of thermal infrared applications and requirements for future high-resolution sensors,” IEEE Transactions on Geoscience and Remote Sensing **54**(5), 2963–2972, Institute of Electrical and Electronics Engineers Inc. (2016) [doi:10.1109/TGRS.2015.2509179].
39. Z. L. Li et al., “Satellite-derived land surface temperature: Current status and perspectives,” Remote Sensing of Environment **131**, 14–37, Elsevier (2013) [doi:10.1016/J.RSE.2012.12.008].
40. S. B. A. Rolim et al., “Comparison of emissivity retrieval methods from ASTER data using Fourier-Transform Infrared Spectroscopy,” Acta Geophysica 2020 68:6 **68**(6), 1867–1876, Springer (2020) [doi:10.1007/S11600-020-00498-X].

41. J. C. Jimenez-Munoz et al., “Revision of the single-channel algorithm for land surface temperature retrieval from landsat thermal-infrared data,” IEEE Transactions on Geoscience and Remote Sensing **47**(1), 339–349 (2009) [doi:10.1109/TGRS.2008.2007125].
42. W. Morrison et al., “Atmospheric and emissivity corrections for ground-based thermography using 3D radiative transfer modelling,” Remote Sensing of Environment **237**, 111524, Elsevier (2020) [doi:10.1016/J.RSE.2019.111524].
43. S. Khoshnoodmotlagh et al., “Urban morphology detection and it’s linking with land surface temperature: A case study for Tehran Metropolis, Iran,” Sustainable Cities and Society **74**, 103228, Elsevier (2021) [doi:10.1016/J.SCS.2021.103228].
44. M. Karimi Firozjaei et al., “Land Surface Ecological Status Composition Index (LSESCI): A novel remote sensing-based technique for modeling land surface ecological status,” Ecological Indicators **123**, 107375, Elsevier (2021) [doi:10.1016/J.ECOLIND.2021.107375].
45. C. Xu et al., “Surface soil temperature seasonal variation estimation in a forested area using combined satellite observations and in-situ measurements,” International Journal of Applied Earth Observation and Geoinformation **91**, 102156, Elsevier (2020) [doi:10.1016/J.JAG.2020.102156].
46. Y. Malbéteau et al., “Normalizing land surface temperature data for elevation and illumination effects in mountainous areas: A case study using ASTER data over a steep-sided valley in Morocco,” Remote Sensing of Environment **189**, 25–39, Elsevier (2017) [doi:10.1016/J.RSE.2016.11.010].
47. X. Shi, J. Sun, and Z. Xiao, “Investigation on River Thermal Regime under Dam Influence by Integrating Remote Sensing and Water Temperature Model,” Water 2021, Vol. 13, Page 133 **13**(2), 133, Multidisciplinary Digital Publishing Institute (2021) [doi:10.3390/W13020133].
48. S. Liu et al., “Detection of Geothermal Anomaly Areas with Spatio-Temporal Analysis Using Multitemporal Remote Sensing Data,” IEEE Journal of Selected Topics in Applied Earth Observations and Remote Sensing **14**, 4866–4878, Institute of Electrical and Electronics Engineers Inc. (2021) [doi:10.1109/JSTARS.2021.3076162].

49. E. A. Kaiser et al., “Spatiotemporal Influences of LULC Changes on Land Surface Temperature in Rapid Urbanization Area by Using Landsat-TM and TIRS Images,” Atmosphere 2022, Vol. 13, Page 460 **13**(3), 460, Multidisciplinary Digital Publishing Institute (2022) [doi:10.3390/ATMOS13030460].

50. V. Ihlen, “Landsat 8 (L8) Data Users Handbook,” U. S. Geological Survey, Virginia (2019).

51. M. Montanaro et al., “Stray Light Artifacts in Imagery from the Landsat 8 Thermal Infrared Sensor,” Remote Sensing 2014, Vol. 6, Pages 10435-10456 **6**(11), 10435–10456, Multidisciplinary Digital Publishing Institute (2014) [doi:10.3390/RS61110435].

52. G. C. Hulley, C. G. Hughes, and S. J. Hook, “Quantifying uncertainties in land surface temperature and emissivity retrievals from ASTER and MODIS thermal infrared data,” Journal of Geophysical Research: Atmospheres **117**(D23), 23113, John Wiley & Sons, Ltd (2012) [doi:10.1029/2012JD018506].

53. Karen Zanter, “LANDSAT SURFACE TEMPERATURE (ST) PRODUCT GUIDE,” in Department of the Interior U.S. Geological Survey **2** (2018).

54. Cody Anderson and Brian Sauer, “Landsat 8-9 Calibration and Validation (Cal/Val) Algorithm Description Document (ADD),” in Department of the Interior U.S. Geological Survey **4** (2021).

55. S. B. A. Rolim et al., “A Review of Temperature and Emissivity Retrieval Methods: Applications and Restrictions,” American Journal of Environmental Engineering **6**(4A), 119–128 (2016).

56. J. C. Jiménez-Muñoz and J. A. Sobrino, “Error sources on the land surface temperature retrieved from thermal infrared single channel remote sensing data,” http://dx.doi.org/10.1080/01431160500075907 **27**(5), 999–1014, Taylor & Francis (2007) [doi:10.1080/01431160500075907].

57. G. H. Pittigliani and S. B. A. Rolim, “Biblioteca Espectral do Laboratório de Sensoriamento Remoto Geológico (LabSRGeo): criando uma base de dados para os Sistemas Laguna Barreira do Rio Grande do Sul,” in Anais do XXVIII Salão de Iniciação Científica da UFRGS, UFRGS, Porto Alegre (2017).

58. USGS, “Earth Explorer” (2020).

59. D&P INSTRUMENTS, “Model 102 Portable FTIR Instruction Manual - Versão 1.2,” Simsbury, CT (2006).

60. P. S. Käfer et al., “Land surface temperature retrieval by landsat 8 thermal band: Applications of laboratory and field measurements,” IEEE Journal of Selected Topics in Applied Earth Observations and Remote Sensing **12**(7), 2332–2341, Institute of Electrical and Electronics Engineers (2019) [doi:10.1109/JSTARS.2019.2913822].

61. A. R. Korb et al., “Portable Fourier transform infrared spectroradiometer for field measurements of radiance and emissivity,” Applied Optics, Vol. 35, Issue 10, pp. 1679-1692 **35**(10), 1679–1692, Optical Society of America (1996) [doi:10.1364/AO.35.001679].

62. J. Rosas, R. Houborg, and M. F. McCabe, “Sensitivity of Landsat 8 Surface Temperature Estimates to Atmospheric Profile Data: A Study Using MODTRAN in Dryland Irrigated Systems,” Remote Sensing 2017, Vol. 9, Page 988 **9**(10), 988, Multidisciplinary Digital Publishing Institute (2017) [doi:10.3390/RS9100988].

63. NASA, “Atmospheric Correction Parameter Calculator,” (Atmospheric Correction Parameter Calculator), 2021, <https://atmcorr.gsfc.nasa.gov/> (accessed 30 November 2021).

64. J. Zhou et al., “Intercomparison of methods for estimating land surface temperature from a Landsat-5 TM image in an arid region with low water vapour in the atmosphere,” http://dx.doi.org/10.1080/01431161.2011.617396 **33**(8), 2582–2602, Taylor & Francis (2011) [doi:10.1080/01431161.2011.617396].

Savannah Tâmara Lemos da Costa received the BS degree in environmental engineering in 2018 from the State University of Pará (UEPA), Marabá, Brazil. Currently she is working toward the MS degree in remote sensing from Federal University of Rio Grande do Sul (UFRGS). Her research interests include radiative transfer simulations in the land-atmosphere system and land surface temperature retrieval.

7 CONSIDERAÇÕES FINAIS

Estimar a LST a partir de dados do infravermelho termal obtidos por satélites ainda é um desafio, pois a radiância registrada pelo sensor depende dos parâmetros da superfície (emissividade e temperatura) e da correção dos efeitos atmosféricos. Diversos métodos possuem restrições e suposições na RTE como forma de minimizar os erros impostos no cálculo da LST.

Nesses métodos, corrigir os efeitos atmosféricos é um dos fatores fundamentais para se obter LST acurada. Nesse contexto, perfis atmosféricos de produtos de reanálise tem se mostrado uma alternativa adequada para caracterizar a estrutura vertical da atmosfera e, por fim, realizar uma correção satisfatória.

Nesse estudo, os algoritmos GSC e ISC e o produto ST foram avaliados na estimativa da LST. Inicialmente, para fundamentar essa avaliação, os parâmetros atmosféricos derivados da ACPC e de perfis de dados de reanálise NCEP CFSv2 com resoluções originais e refinadas por um modelo numérico foram comparados. Em seguida, estes parâmetros foram utilizados na estimativa da LST, para verificar a aplicabilidade da ACPC e dos perfis como fonte de dados de correção atmosférica. Para calcular o erro, perfis de radiossondagens *in situ* foram utilizados para gerar os parâmetros atmosféricos e a LST, assumidos como valores de referência.

Os resultados obtidos mostraram que, para os três parâmetros atmosféricos (transmitância, radiância ascendente e descendente), a ACPC forneceu os menores erros quando comparada com os parâmetros derivados dos perfis das radiossondas. Os perfis NCEP CFSv2 de resoluções originais apresentaram o segundo menor erro na estimativa dos parâmetros. Os perfis NCEP CFSv2 de resoluções refinadas com o modelo WRF não mostraram diferenças estatísticas significativas, apresentaram os maiores erros na estimativa dos três parâmetros.

Em relação a estimativa da LST a partir das diferentes fontes de dados atmosféricos, os parâmetros calculados com os perfis NCEP CFSv2 de resoluções originais resultaram em LST com os menores erros (RMSE de 0,55 K). Em seguida, os parâmetros da ACPC permitiram estimar a LST com RMSE de 0,56 K. Já os parâmetros calculados com os perfis NCEP CFSv2 de resoluções refinadas através do WRF, em grades de 12 Km e 3 Km, resultaram em LST com RMSE de 0,79 e 0,82 K, respectivamente. Ambas as grades WRF e perfil NCEP CFSv2 geraram um viés

LST positivo, enquanto que a ACPC gerou um viés negativo. No geral, todas os perfis apresentaram resultados relativamente bons na estimativa da LST.

Nesta primeira etapa concluiu-se que, dentre os dados atmosféricos analisados, os parâmetros calculados a partir dos perfis NCEP CFSv2 de resoluções originais e da ACPC se mostraram os mais adequados para a correção atmosférica e estimativa da LST. Do ponto de vista prático, a ACPC pode se mostrar mais vantajosa, pois é uma ferramenta que automaticamente extrai e complementa os perfis NCEP, os introduz no MODTRAN e gera os três parâmetros atmosféricos para o local e horário da passagem do satélite.

A segunda etapa da pesquisa foi dedicada à avaliação dos algoritmos GSC, ISC e do produto ST na estimativa da LST. Um campo de dunas em uma região litorânea do Hemisfério Sul foi selecionado e os dados TIR do Landsat 8 foram utilizados para derivar a LST. Com base nos resultados do primeiro estudo, notou-se que a ACPC é apropriada na correção atmosférica e estimativa da LST. Sendo assim, os dados atmosféricos utilizados nos algoritmos GSC e ISC foram extraídos e interpolados pela ACPC.

Para avaliar o desempenho dos algoritmos e do produto ST, a inversão e solução da RTE foi utilizada no cálculo da LST, considerada verdade de campo. Nesta estimativa, a emissividade do quartzo obtida em campo e parâmetros atmosféricos derivados de radiossondagem lançada *in situ* foram empregados.

Os resultados mostraram melhor desempenho para o ISC com um RMSE de 0,69 K, seguido pelo GSC (RMSE de 2,5 K) e pelo produto ST (RMSE de 4,24 K). Todos as LSTs estimadas apresentaram alta correlação (≥ 0,98) com a LST verdade de campo. O RMSE obtido para o GSC pode ter sido ocasionado pelo alto conteúdo de vapor d’água de 3,04 $g.cm^{-2}$, mostrando concordância com outros estudos em que os erros encontrados foram de aproximadamente 2.7 K e 4 K. Em contrapartida, esse erro foi substancialmente reduzido com a adição da temperatura média atmosférica no ISC. O produto ST apresentou o pior desempenho. Estudos anteriores reportaram que este produto pode apresentar erros de 2,6 K em condições de alta umidade e de 3 K devido a emissividade estimada incorretamente. Dessa forma, o alto RMSE encontrado pode estar atribuído a estes dois fatores.

Alguns estudos tem mostrado que, a LST deve possuir erros entre 0,3 K a 1 K para ser útil em detecção de mudanças climáticas. Já em estudos de balanço de energia, um erro de até 2 K é aceitável. Dessa forma, concluiu-se com essa pesquisa que o ISC se mostrou o mais adequado, podendo ser aplicado em estudos de balanço de energia.

Confirmou-se, portanto, a importância da análise dos métodos SC no presente trabalho, justificada pela sua aplicação em dados de radiância de sensores termais com uma banda, principalmente para estudos com séries temporais de LST derivadas da série Landsat (1982 a 2022), além de situações de mau funcionamento de canais espectrais, como o ocorrido no Landsat 8. Esta pesquisa permitiu conhecer os erros na LST produzidos pelos algoritmos GSC, ISC e pelo produto ST nas condições do Hemisfério Sul, complementando e reforçando os estudos realizados neste tema, bem como fornecendo um *feedback* para os desenvolvedores dos algoritmos.

Apesar das contribuições obtidas com esta pesquisa, algumas limitações devem ser destacadas e consideradas em trabalhos futuros. Devido à pandemia COVID-19, a utilização de dados de LST *in situ* na avaliação, tanto no aeroporto SBPA quanto no campo de dunas Cidreira, foi inviabilizada. Dessa forma, assumimos como cenário ideal a LST estimada com a RTE utilizando dados atmosféricos de radiossondagem. Além do mais, a avaliação do desempenho dos algoritmos e do produto ST foi feita em um alvo composto por 99,53% de quartzo. Portanto, sugere-se que em pesquisas futuras a avaliação englobe outros tipos de cobertura do solo e que LST *in situ* seja adicionada. Além disso, é importante abordar uma análise sensitiva dos algoritmos e do produto ST quanto aos dados utilizados na correção atmosférica.

FINANCIAMENTO

Esta pesquisa foi realizada com apoio da Coordenação de Aperfeiçoamento de Pessoal de Nível Superior – Brasil (CAPES) – Código de Financiamento 001, através de bolsa de mestrado.

REFERÊNCIAS

ANDREWS, David G. Some Comparisons between the Middle Atmosphere Dynamics of the Southern and Northern Hemispheres. **Middle Atmosphere**, v. 130, n. 2/3, p. 213–232, 1989. DOI: 10.1007/978-3-0348-5825-0_6.

BARSI, Julia A. *et al.* Validation of a web-based atmospheric correction tool for single thermal band instruments. *In:* Optics and Photonics, 2005, San Diego, California. **Proceedings Earth Observing Systems X**. San Diego: SPIE, v. 5882, 2005. p. 136–142. DOI: https://doi.org/10.1117/12.619990.

BARSI, Julia A.; BARKER, John L.; SCHOTT, John R. An Atmospheric Correction Parameter Calculator for a Single Thermal Band Earth-Sensing Instrument. **International Geoscience and Remote Sensing Symposium (IGARSS)**, v. 5, p. 3014–3016, 2003. DOI: https://doi.org/10.1109/IGARSS.2003.1294665.

BECKER, François; LI, Zhao Liang. Towards a local split window method over land surfaces. **International Journal of Remote Sensing**, v. 11, n. 3, p. 369–393, 2007. DOI: http://dx.doi.org/10.1080/01431169008955028.

BENMECHETA, A.; ABDELLAOUI, A.; HAMOU, A. A comparative study of land surface temperature retrieval methods from remote sensing data. **Journal canadien de télédétection**, v. 39, n. 1, p. 59–73, 2014. DOI: http://dx.doi.org/10.5589/m13-008.

BERK, Alexander *et al.* MODTRAN Cloud and Multiple Scattering Upgrades with Application to AVIRIS. **Remote Sensing of Environment**, v. 65, n. 3, p. 367–375, 1998. DOI: https://doi.org/10.1016/S0034-4257(98)00045-5.

ANDERSON, Cody; SAUER, Brian. **Landsat 8-9 Calibration and Validation (Cal/Val) Algorithm Description Document (ADD)**. 2021. Disponível em: https://www.usgs.gov/media/files/landsat-8-9-calibration-validation-algorithm-description-document. Acesso em: 14 out. 2021.

COOK, Monica *et al.* Development of an Operational Calibration Methodology for the Landsat Thermal Data Archive and Initial Testing of the Atmospheric Compensation Component of a Land Surface Temperature (LST) Product from the Archive. **Remote Sensing 2014**, v. 6, n. 11, p. 11244–11266, 2014. Disponível em: https://www.mdpi.com/2072-4292/6/11/11244/htm. Acesso em: 30 nov. 2021.

CRISTÓBAL, Jordi *et al.* An Improved Single-Channel Method to Retrieve Land Surface Temperature from the Landsat-8 Thermal Band. **Remote Sensing**, v. 10, n. 3, p. 431, 2018. Disponível em: https://www.mdpi.com/2072-4292/10/3/431/htm. Acesso em: 30 nov. 2021.

CRISTÓBAL, Jordi *et al.* Improvements in land surface temperature retrieval from the Landsat series thermal band using water vapor and air temperature. **Journal of Geophysical Research: Atmospheres**, v. 114, n. D8, p. 8103, 2009. Disponível em:

https://onlinelibrary.wiley.com/doi/full/10.1029/2008JD010616. Acesso em: 30 nov. 2021.

DASH, Prasanjit *et al.* Land surface temperature and emissivity estimation from passive sensor data: Theory and practice-current trends. **International Journal of Remote Sensing**, v. 23, n. 13, p. 2563–2594, 2002. Disponível em: https://doi.org/10.1080/01431160110115041. Acesso em: 15 maio 2020.

DASH, Prasanjit *et al.* Retrieval of land surface temperature and emissivity from satellite data: Physics, theoretical limitations and current methods. **Journal of the Indian Society of Remote Sensing**, v. 29, n. 1, p. 23–30, 2001. Disponível em: https://link.springer.com/article/10.1007/BF02989910. Acesso em: 23 fev. 2022.

DEE, D. P. *et al.* The ERA-Interim reanalysis: configuration and performance of the data assimilation system. **Quarterly Journal of the Royal Meteorological Society**, v. 137, n. 656, p. 553–597, 2011. Disponível em: https://onlinelibrary.wiley.com/doi/full/10.1002/qj.828. Acesso em: 12 set. 2022.

DIAZ, Lucas Ribeiro *et al.* Land Surface Temperature Retrieval Using High-Resolution Vertical Profiles Simulated by WRF Model. **Atmosphere**, v. 12, n. 11, p. 1436, 2021. Disponível em: https://www.mdpi.com/2073-4433/12/11/1436/htm. Acesso em: 30 nov. 2021.

DIAZ, Lucas Ribeiro *et al.* Using the WRF Model to Refine NCEP CFSv2 Reanalysis Atmospheric Profile: A Southern Brazil Test Case. **Brazilian Journal of Geophysics**, v. 38, n. 2, p. 5–31, 2020. Disponível em: https://sbgf.org.br/revista/index.php/rbgf/article/view/2043. Acesso em: 1 dez. 2021.

D&P INSTRUMENTS. **Model 102 Portable FTIR Instruction Manual - Versão 1.2**. Simsbury, CT, 2006.

DUAN, Si Bo *et al.* Land-surface temperature retrieval from Landsat 8 single-channel thermal infrared data in combination with NCEP reanalysis data and ASTER GED product. **International Journal of Remote Sensing**, v. 40, n. 5–6, p. 1763–1778, 2018. Disponível em: https://doi.org/10.1080/01431161.2018.1460513. Acesso em: 1 dez. 2021.

DUAN, Si Bo *et al.* Validation of Landsat land surface temperature product in the conterminous United States using in situ measurements from SURFRAD, ARM, and NDBC sites. **International Journal of Digital Earth**, v. 14, n. 5, p. 640–660, 2020. Disponível em: https://doi.org/10.1080/17538947.2020.1862319. Acesso em: 30 nov. 2021.

ECMWF. **Fact sheet: Reanalysis**. 2020. Disponível em: https://www.ecmwf.int/en/about/media-centre/focus/2020/fact-sheet-reanalysis. Acesso em: 1 dez. 2021.

GERACE, Aaron; MONTANARO, Matthew. Derivation and validation of the stray light correction algorithm for the thermal infrared sensor onboard Landsat 8. **Remote Sensing of Environment**, v. 191, p. 246–257, 2017. Disponível em: Acesso em: 6 ago. 2022.

GERACE, Aaron; MONTANARO, Matthew; ROHRBACH, Scott. Toward an operational stray light correction for the Landsat 8 Thermal Infrared Sensor. **Applied Optics,** v. 54, n. 13, p. 3963–3978, 2015. Disponível em: https://opg.optica.org/viewmedia.cfm?uri=ao-54-13-3963&seq=0&html=true. Acesso em: 6 ago. 2022.

GILLESPIE, Alan *et al.* A temperature and emissivity separation algorithm for advanced spaceborne thermal emission and reflection radiometer (ASTER) images. **IEEE Transactions on Geoscience and Remote Sensing**, v. 36, n. 4, p. 1113–1126, 1998. DOI: https://doi.org/10.1109/36.700995.

GUANGMENG, Guo; MEI, Zhou. Using MODIS land surface temperature to evaluate forest fire risk of Northeast China. **IEEE Geoscience and Remote Sensing Letters**, [*s. l.*], v. 1, n. 2, p. 98–100, 2004. DOI: 10.1109/LGRS.2004.826550.

GUILLEVIC, Pierre *et al.* **Land Surface Temperature Product Validation Best Practice Protocol**. Land Product Validation Subgroup (WGCV/CEOS), 2018. Disponível em: https://lpvs.gsfc.nasa.gov/PDF/CEOS_LST_PROTOCOL_Feb2018_v1.1.0_light.pdf. Acesso em: 1 dez. 2021.

HASSANLI, H.; RAHIMZADEGAN, M. Investigating extracted total precipitable water vapor from Weather Research and Forecasting (WRF) model and MODIS measurements. **J. Atmos. Solar-Terrestrial Phys.**, v. 193, n. 105060, 2019. DOI: 10.1016/j.jastp.2019.105060

HERSBACH, Hans *et al.* The ERA5 global reanalysis. **Quarterly Journal of the Royal Meteorological Society**, v. 146, n. 730, p. 1999–2049, 2020. Disponível em: https://onlinelibrary.wiley.com/doi/full/10.1002/qj.3803. Acesso em: 12 set. 2022.

HOOK, Simon J. *et al.* A comparison of techniques for extracting emissivity information from thermal infrared data for geologic studies. **Remote Sensing of Environment**, v. 42, n. 2, p. 123–135, 1992. Disponível em: https://doi.org/10.1016/0034-4257(92)90096-3. Acesso em: 30 nov. 2021.

HULLEY, Glynn C.; HUGHES, Christopher G.; HOOK, Simon J. Quantifying uncertainties in land surface temperature and emissivity retrievals from ASTER and MODIS thermal infrared data. **Journal of Geophysical Research: Atmospheres**, v. 117, n. D23, p. 23113, 2012. Disponível em: https://onlinelibrary.wiley.com/doi/full/10.1029/2012JD018506. Acesso em: 1 dez. 2021.

IHLEN, V. **Landsat 8 (L8) Data Users Handbook**. Virginia: U. S. Geological Survey, 2019. Disponível em: https://www.usgs.gov/landsat-missions/landsat-8-data-users-handbook. Acesso em: 30 nov. 2021.

JENSEN, John R**. Remote Sensing of the Environment: An Earth Resource Perspective**, 2. ed. Prentice Hall, Upper Saddle River, NJ, p. 1–592, 2009.

JIMÉNEZ-MUÑOZ, Juan C. *et al.* Land surface temperature retrieval methods from landsat-8 thermal infrared sensor data. **IEEE Geoscience and Remote Sensing Letters**, v. 11, n. 10, p. 1840–1843, 2014. Disponível em: https://doi.org/10.1109/LGRS.2014.2312032. Acesso em: 30 nov. 2021.

JIMÉNEZ-MUÑOZ, Juan C. *et al.* Revision of the single-channel algorithm for land surface temperature retrieval from landsat thermal-infrared data. **IEEE Transactions on Geoscience and Remote Sensing**, v. 47, n. 1, p. 339–349, 2009. Disponível em: https://doi.org/10.1109/TGRS.2008.2007125. Acesso em: 29 abr. 2022.

JIMÉNEZ-MUNOZ, Juan C.; SOBRINO, José A. A generalized single-channel method for retrieving land surface temperature from remote sensing data. **Journal of Geophysical Research: Atmospheres**, v. 108, n. D22, p. 4688, 2003. Disponível em: https://onlinelibrary.wiley.com/doi/full/10.1029/2003JD003480. Acesso em: 1 dez. 2021.

JIMÉNEZ-MUNOZ, Juan C.; SOBRINO, José A. A single-channel algorithm for land-surface temperature retrieval from ASTER data. **IEEE Geoscience and Remote Sensing Letters**, v. 7, n. 1, p. 176–179, 2010. Disponível em: https://doi.org/10.1109/LGRS.2009.2029534. Acesso em: 30 nov. 2021.

KÄFER, Pâmela S. *et al.* Assessing uncertainties in estimating surface energy fluxes from remote sensing over natural grasslands in Brazil. **Theoretical and Applied Climatology**, v. 148, n. 1, p. 751–765, 2022. Disponível em: https://link.springer.com/article/10.1007/s00704-021-03869-6. Acesso em: 5 jul. 2022.

KÄFER, Pâmela S. *et al.* Land surface temperature retrieval by Landsat 8 thermal band: Applications of laboratory and field measurements. **IEEE Journal of Selected Topics in Applied Earth Observations and Remote Sensing**, v. 12, n. 7, p. 2332–2341, 2019. Disponível em: https://doi.org/10.1109/JSTARS.2019.2913822. Acesso em: 30 nov. 2021.

KAISER, Eduardo A. *et al.* Spatiotemporal Influences of LULC Changes on Land Surface Temperature in Rapid Urbanization Area by Using Landsat-TM and TIRS Images. **Atmosphere,** v. 13, n. 3, p. 460, 2022. Disponível em: https://www.mdpi.com/2073-4433/13/3/460/htm. Acesso em: 29 abr. 2022.

KALNAY, E. *et al.* The NCEP/NCAR 40-Year Reanalysis Project. **Bulletin of the American Meteorological Society**, v. 77, n. 3, p. 437–472, 1996. Disponível em:

https://journals.ametsoc.org/view/journals/bams/77/3/1520-0477_1996_077_0437_tnyrp_2_0_co_2.xml. Acesso em: 11 set. 2022.

KANAMITSU, Masao *et al.* NCEP–DOE AMIP-II Reanalysis (R-2). **Bulletin of the American Meteorological Society**, v. 83, n. 11, p. 1631–1644, 2002. Disponível em: https://journals.ametsoc.org/view/journals/bams/83/11/bams-83-11-1631.xml. Acesso em: 12 set. 2022.

KHOSHNOODMOTLAGH, Sajad *et al.* Urban morphology detection and it's linking with land surface temperature: A case study for Tehran Metropolis, Iran. **Sustainable Cities and Society**, v. 74, p. 103228, 2021. Disponível em: https://doi.org/10.1016/j.scs.2021.103228. Acesso em: 30 nov. 2021.

KOBAYASHI, Shinya *et al.* The JRA-55 Reanalysis: General Specifications and Basic Characteristics. **Journal of the Meteorological Society of Japan. Ser. II**, v. 93, n. 1, p. 5–48, 2015. Disponível em: https://doi.org/10.2151/jmsj.2015-001. Acesso em: 12 set. 2022.

KÖPPEN, Wladimir. **Klassifikation Der Klimate Nach Temperatur, Niederschlag Und Jahreslauf**. Petermanns Geographische Mitteilungen, p. 193–203, 1918.

KUENZER, Claudia; DECH, Stefan. **Thermal remote sensing Sensors, Methods, Applications**. Dordrecht: Springer Netherlands, 2013.

KUZNETSOV, Anatoly *et al.* **Remote sensing of the environment and radiation transfer: An introductory survey**. Springer-Verlag Berlin Heidelberg, 2012.

LARABY, Kelly. **Landsat Surface Temperature Product: Global Validation and Uncertainty Estimation**. 2017. Tese (Doutorado em Imaging Science), Rochester Institute of Technology, Rochester, NY, 2017. Disponível em: https://scholarworks.rit.edu/theses/9439. Acesso em: 24 fev. 2022.

LARABY, Kelly G.; SCHOTT, John R. Uncertainty estimation method and Landsat 7 global validation for the Landsat surface temperature product. **Remote Sensing of Environment**, v. 216, p. 472–481, 2018. Disponível em: https://doi.org/10.1016/j.rse.2018.06.026. Acesso em: 30 nov. 2021.

LECKNER, Bo. The spectral distribution of solar radiation at the earth's surface-elements of a model. **Solar Energy**, [*s. l.*], v. 20, n. 2, p. 143–150, 1978. Disponível em: Acesso em: 15 maio 2020.

LI, Yachao *et al.* An Improved Single-Channel Polar Region Ice Surface Temperature Retrieval Algorithm Using Landsat-8 Data. **IEEE Transactions on Geoscience and Remote Sensing**, v. 57, n. 11, p. 8557–8569, 2019. Disponível em: https://doi.org/10.1109/TGRS.2019.2921606. Acesso em: 30 nov. 2021.

LI, Zhao Liang *et al.* Land surface emissivity retrieval from satellite data. **International Journal of Remote Sensing**, v. 34, n. 9–10, p. 3084–3127, 2013a. Disponível em: https://doi.org/10.1080/01431161.2012.716540. Acesso em: 6 ago. 2022.

LI, Zhao Liang *et al.* Satellite-derived land surface temperature: Current status and perspectives. **Remote Sensing of Environment**, v. 131, p. 14–37, 2013b. Disponível em: https://doi.org/10.1016/j.rse.2012.12.008. Acesso em: 15 maio 2020.

LI, Zhao Liang; BECKER, François. Feasibility of land surface temperature and emissivity determination from AVHRR data. **Remote Sensing of Environment**, v. 43, n. 1, p. 67–85, 1993. Disponível em: https://doi.org/10.1016/0034-4257(93)90065-6. Acesso em: 23 fev. 2022.

LI, Shanshan; JIANG, Geng Ming. Land Surface Temperature Retrieval from Landsat-8 Data with the Generalized Split-Window Algorithm. **IEEE Access**, [*s. l.*], v. 6, p. 18149–18162, 2018. Disponível em: https://doi.org/10.1109/ACCESS.2018.2818741. Acesso em: 30 nov. 2021.

LIOU, Kuo-Nan. **An introduction to atmospheric radiation**. Academic Press, 2002.

LIU, Shanwei *et al.* Detection of Geothermal Anomaly Areas with Spatio-Temporal Analysis Using Multitemporal Remote Sensing Data. **IEEE Journal of Selected Topics in Applied Earth Observations and Remote Sensing**, v. 14, p. 4866–4878, 2021. Disponível em: https://doi.org/10.1109/JSTARS.2021.3076162. Acesso em: 30 nov. 2021.

MALAKAR, Nabin K. *et al.* An Operational Land Surface Temperature Product for Landsat Thermal Data: Methodology and Validation. **IEEE Transactions on Geoscience and Remote Sensing**, [*s. l.*], v. 56, n. 10, p. 5717–5735, 2018. Disponível em: https://doi.org/10.1109/TGRS.2018.2824828. Acesso em: 30 nov. 2021.

MCMILLIN, Larry M. Estimation of sea surface temperatures from two infrared window measurements with different absorption. **Journal of Geophysical Research**, v. 80, n. 36, p. 5113–5117, 1975. Disponível em: https://onlinelibrary.wiley.com/doi/full/10.1029/JC080i036p05113. Acesso em: 29 abr. 2022.

MENG, Xiangchen; CHENG, Jie. Evaluating Eight Global Reanalysis Products for Atmospheric Correction of Thermal Infrared Sensor—Application to Landsat 8 TIRS10 Data. **Remote Sensing**, v. 10, n. 3, p. 474, 2018. Disponível em: https://www.mdpi.com/2072-4292/10/3/474/htm. Acesso em: 30 nov. 2021.

MONTANARO, Matthew *et al.* Stray Light Artifacts in Imagery from the Landsat 8 Thermal Infrared Sensor. **Remote Sensing,** v. 6, n. 11, p. 10435–10456, 2014. Disponível em: https://www.mdpi.com/2072-4292/6/11/10435/htm. Acesso em: 29 abr. 2022.

NASA. **Atmospheric Correction Parameter Calculator**. 2021. Disponível em: https://atmcorr.gsfc.nasa.gov/. Acesso em: 30 nov. 2021.

NCEP *et al.* **NCEP FNL Operational Model Global Tropospheric Analyses, continuing from July 1999. Research Data Archive at the National Center for Atmospheric Research, Computational and Information Systems Laboratory**. 2000. DOI: https://doi.org/10.5065/D6M043C6.

NCEP *et al.* **NCEP Global Forecast System (GFS) Analyses and Forecasts. Research Data Archive at the National Center for Atmospheric Research, Computational and Information Systems Laboratory.** 2007. DOI: 10.5065/D65D8PWK.

NORMAN, John M.; BECKER, François. Terminology in thermal infrared remote sensing of natural surfaces. **Agricultural and Forest Meteorology**, v. 77, n. 3–4, p. 153–166, 1995. Disponível em: https://doi.org/10.1016/0168-1923(95)02259-Z. Acesso em: 15 maio 2020.

OLSEN, R.C. **Remote Sensing from Air and Space**. SPIE, 2007. Disponível em: https://spiedigitallibrary.org/ebooks/PM/Remote-Sensing-from-Air-and-Space/eISBN-9780819481078/10.1117/3.673407. Acesso em: 15 maio 2020.

PAZ, Louize. **Avaliação da influência antrópica na erosão praial no Litoral Norte do Rio Grande do Sul, Brasil**. Trabalho de conclusão de curso, Universidade Federal do Rio Grande do Sul. Instituto de Biociências, Imbé, 2015. Disponível em: https://lume.ufrgs.br/handle/10183/140158. Acesso em: 9 jun. 2022.

PITTIGLIANI, Gabriel Horn; ROLIM, Silvia Beatriz Alves. Biblioteca Espectral do Laboratório de Sensoriamento Remoto Geológico (LabSRGeo): criando uma base de dados para os Sistemas Laguna Barreira do Rio Grande do Sul. *In:* XXVIII Salão de Iniciação Científica da UFRGS, 2017, Porto Alegre. **Anais do XXVIII Salão de Iniciação Científica da UFRGS.** Porto Alegre: UFRGS, 2017.

PLANCK, Max. Entropie und Temperatur strahlender Wärme. **Annalen der Physik**, v. 306, n. 4, p. 719–737, 1900. Disponível em: http://doi.wiley.com/10.1002/andp.19003060410. Acesso em: 15 maio 2020.

PÖRTNER, Hans-Otto *et al.* **IPCC, 2022: Climate Change 2022: Impacts, Adaptation, and Vulnerability. Contribution of Working Group II to the Sixth Assessment Report of the Intergovernmental Panel on Climate Change**. 2022. Disponível em: https://www.ipcc.ch/report/ar6/wg2/.

POWERS, Jordan G. *et al.* The Weather Research and Forecasting Model: Overview, System Efforts, and Future Directions. **Bulletin of the American Meteorological Society**, v. 98, n. 8, p. 1717–1737, 2017. Disponível em: https://journals.ametsoc.org/view/journals/bams/98/8/bams-d-15-00308.1.xml. Acesso em: 12 set. 2022.

PRASAD, Narasimha; BANDI, Rajkumar Gatadi; PADMAJA, Buddi. Monitoring and extracting abnormalities in land surface temperature images for automatic identification of forest fires. *In:* 7th European Modelling Symposium on Computer Modelling and Simulation, 2013, Manchester, UK. **Proceedings.** Manchester: IEEE, 2013, p. 215–219. Disponível em: https://doi.org/10.1109/EMS.2013.37. Acesso em: 20 ago. 2022.

QIN, Z.; KARNIELI, A.; BERLINER, P. A mono-window algorithm for retrieving land surface temperature from Landsat TM data and its application to the Israel-Egypt border region. **International Journal of Remote Sensing**, v. 22, n. 18, p. 3719–3746, 2001. Disponível em: https://doi.org/10.1080/01431160010006971. Acesso em: 15 maio 2020.

RAHIMZADEGAN, M.; MOBASHERI, MR. An attempt for improving MODIS atmospheric temperature profiles products in clear sky. **Met. Apps.**, v. 18, n. 2, p. 181–187, 2011. DOI: 10.1002/met.221

RIENECKER, Michele M. *et al.* MERRA: NASA's Modern-Era Retrospective Analysis for Research and Applications. **Journal of Climate**, v. 24, n. 14, p. 3624–3648, 2011. Disponível em: https://journals.ametsoc.org/view/journals/clim/24/14/jcli-d-11-00015.1.xml. Acesso em: 12 set. 2022.

ROCHA, Nájila Souza da *et al.* The Influence of Land Surface Temperature in Evapotranspiration Estimated by the S-SEBI Model. **Atmosphere**, v. 11, n. 10, p. 1059, 2020. Disponível em: https://www.mdpi.com/2073-4433/11/10/1059/htm. Acesso em: 22 ago. 2022.

ROLIM, Silvia B. A. *et al.* A Review of Temperature and Emissivity Retrieval Methods: Applications and Restrictions. **American Journal of Environmental Engineering**, v. 6, n. 4A, p. 119–128, 2016. DOI: http://dx.doi.org/10.5923/s.ajee.201601.18

ROLIM, Silvia B. A. *et al.* Comparison of emissivity retrieval methods from ASTER data using Fourier-Transform Infrared Spectroscopy. **Acta Geophysica,** v. 68, n. 6, p. 1867–1876, 2020. Disponível em: https://link.springer.com/article/10.1007/s11600-020-00498-x. Acesso em: 1 dez. 2021.

ROSAS, Jorge; HOUBORG, Rasmus; MCCABE, Matthew F. Sensitivity of Landsat 8 Surface Temperature Estimates to Atmospheric Profile Data: A Study Using MODTRAN in Dryland Irrigated Systems. **Remote Sensing**, v. 9, n. 10, p. 988, 2017. Disponível em: https://www.mdpi.com/2072-4292/9/10/988/htm. Acesso em: 30 nov. 2021.

SABINS, Floyd F. **Remote sensing principles and interpretation**. 3. ed. W.H. Freeman & Co Ltd, 1996.

SAHA, Suranjana *et al.* The NCEP Climate Forecast System Reanalysis. **Bulletin of the American Meteorological Society**, v. 91, n. 8, p. 1015–1058, 2010. Disponível em: https://journals.ametsoc.org/view/journals/bams/91/8/2010bams3001_1.xml. Acesso em: 12 set. 2022.

SAHA, Suranjana *et al.* The NCEP Climate Forecast System Version 2. **Journal of Climate**, v. 27, n. 6, p. 2185–2208, 2014. Disponível em: https://journals.ametsoc.org/view/journals/clim/27/6/jcli-d-12-00823.1.xml. Acesso em: 30 nov. 2021.

SCHOTT, John R. **Remote sensing: the image chain approach**. Oxford University Press, 2007.

SEKERTEKIN, Aliihsan. Validation of Physical Radiative Transfer Equation-Based Land Surface Temperature Using Landsat 8 Satellite Imagery and SURFRAD in-situ Measurements. **Journal of Atmospheric and Solar-Terrestrial Physics**, v. 196, p. 105161, 2019. Disponível em: https://doi.org/10.1016/j.jastp.2019.105161. Acesso em: 29 abr. 2022.

SEKERTEKIN, Aliihsan; BONAFONI, Stefania. Land Surface Temperature Retrieval from Landsat 5, 7, and 8 over Rural Areas: Assessment of Different Retrieval Algorithms and Emissivity Models and Toolbox Implementation. **Remote Sensing,** v. 12, n. 2, p. 294, 2020. Disponível em: https://www.mdpi.com/2072-4292/12/2/294/htm. Acesso em: 30 nov. 2021.

SHI, Xi; SUN, Jian; XIAO, Zijun. Investigation on River Thermal Regime under Dam Influence by Integrating Remote Sensing and Water Temperature Model. **Water,** v. 13, n. 2, p. 133, 2021. Disponível em: https://www.mdpi.com/2073-4441/13/2/133/htm. Acesso em: 30 nov. 2021.

SKAMAROCK, William *et al.* A Description of the Advanced Research WRF Model Version 4.3. 2021. Disponível em: https://opensky.ucar.edu/islandora/object/technotes%3A588/. Acesso em: 12 set. 2022.

SOBRINO, José A. *et al.* Evapotranspiration estimation with the S-SEBI method from Landsat 8 data against lysimeter measurements at the barrax site, Spain. **Remote Sensing**, v. 13, n. 18, 2021. Disponível em: https://doi.org/10.3390/rs13183686. Acesso em: 5 jul. 2022.

____________________. Improvements in the Split-Window Technique for Land Surface Temperature Determination. **IEEE Transactions on Geoscience and Remote Sensing**, v. 32, n. 2, p. 243–253, 1994. Disponível em: https://doi.org/10.1109/36.295038. Acesso em: 29 abr. 2022.

____________________. Land surface emissivity retrieval from different VNIR and TIR sensors. **IEEE Transactions on Geoscience and Remote Sensing**, v. 46, n. 2, p. 316–327, 2008. Disponível em: https://doi.org/10.1109/TGRS.2007.904834. Acesso em: 15 maio 2020.

____________________. Review of thermal infrared applications and requirements for future high-resolution sensors. **IEEE Transactions on Geoscience and Remote Sensing**, v. 54, n. 5, p. 2963–2972, 2016. Disponível em: http://dx.doi.org/10.1109/TGRS.2015.2509179. Acesso em: 30 nov. 2021.

SOBRINO, José A.; JIMÉNEZ-MUÑOZ, Juan C.; PAOLINI, Leonardo. Land surface temperature retrieval from LANDSAT TM 5. **Remote Sensing of Environment**, v. 90, n. 4, p. 434–440, 2004. Disponível em: https://doi.org/10.1016/j.rse.2004.02.003. Acesso em: 30 nov. 2021.

SOBRINO, José A.; RAISSOUNI, Naoufal. Toward remote sensing methods for land cover dynamic monitoring: Application to Morocco. **International Journal of Remote Sensing**, v. 21, n. 2, p. 353–366, 2010. Disponível em: **https://doi.org/10.1080/014311600210876**. Acesso em: 14 fev. 2022.

TANG, Huajun; LI, Zhao-Liang. **Quantitative Remote Sensing in Thermal Infrared**. Berlin, Heidelberg: Springer Berlin Heidelberg, 2014. Disponível em: http://link.springer.com/10.1007/978-3-642-42027-6. Acesso em: 22 out. 2020.

TARDY, Benjamin *et al.* A Software Tool for Atmospheric Correction and Surface Temperature Estimation of Landsat Infrared Thermal Data. **Remote Sensing,** v. 8, n. 9, p. 696, 2016. Disponível em: https://www.mdpi.com/2072-4292/8/9/696/htm. Acesso em: 30 nov. 2021.

USGS. **Earth Explorer**. 2020. Disponível em: https://earthexplorer.usgs.gov/

VAN DE GRIEND, A. A.; OWE, M. On the relationship between thermal emissivity and the normalized difference vegetation index for natural surfaces. **International Journal of Remote Sensing**, v. 14, n. 6, p. 1119–1131, 2007. Disponível em: http://dx.doi.org/10.1080/01431169308904400. Acesso em: 14 fev. 2022.

VAN LOON, Harry. A review of the surface climate of the Southern Hemisphere and some comparisons with the Northern Hemisphere. **Journal of Marine Systems**, v. 2, n. 1–2, p. 171–194, 1991. Disponível em: https://doi.org/10.1016/0924-7963(91)90023-N. Acesso em: 21 ago. 2022.

WAN, Jikang; ZHU, Min; DING, Wei. Accuracy Evaluation and Parameter Analysis of Land Surface Temperature Inversion Algorithm for Landsat-8 Data. **Advances in Meteorology**, v. 2021, 2021. Disponível em: https://doi.org/10.1155/2021/9917145. Acesso em: 14 fev. 2022.

XU, Chenyang *et al.* Surface soil temperature seasonal variation estimation in a forested area using combined satellite observations and in-situ measurements. **International Journal of Applied Earth Observation and Geoinformation**, v. 91, p. 102156, 2020. Disponível em: https://doi.org/10.1016/j.jag.2020.102156. Acesso em: 30 nov. 2021.

YANG, Jingjing *et al.* Evaluation of Seven Atmospheric Profiles from Reanalysis and Satellite-Derived Products: Implication for Single-Channel Land Surface Temperature Retrieval. **Remote Sensing,** v. 12, n. 5, p. 791, 2020. Disponível em: https://www.mdpi.com/2072-4292/12/5/791/htm. Acesso em: 30 nov. 2021.

YU, Xiaolei; GUO, Xulin; WU, Zhaocong. Land Surface Temperature Retrieval from Landsat 8 TIRS—Comparison between Radiative Transfer Equation-Based Method, Split Window Algorithm and Single Channel Method. **Remote Sensing**, v. 6, n. 10, p. 9829–9852, 2014. Disponível em: https://www.mdpi.com/2072-4292/6/10/9829/htm. Acesso em: 30 nov. 2021.

ZANTER, Karen. **Landsat Surface Temperature (ST) product guide**. 2018. Disponível em: https://www.usgs.gov/core-science-systems/nli/landsat/landsat-collection-2-surface-temperature. Acesso em: 1 dez. 2021.

ZHOU, Ji *et al.* Intercomparison of methods for estimating land surface temperature from a Landsat-5 TM image in an arid region with low water vapour in the atmosphere. **International Journal of Remote Sensing**, v. 33, n. 8, p. 2582–2602, 2011. Disponível em: http://dx.doi.org/10.1080/01431161.2011.617396. Acesso em: 20 fev. 2022.